Molecules and the Dynamics of SN 1987A

by

Holly May Davies

A Thesis submitted to Cardiff University
for the degree of Master of Philosophy

September 2024

Abstract

Molecular emission has helped diagnose physical properties and conditions of many astronomical objects in the ISM. Recently, molecular emission has been observed in the ejecta of supernova remnant SN 1987A. On-going observations of SN 1987A since its explosion have been key to understanding how a young core collapse supernova remnant evolves across time. For this master's thesis, I analyse high angular resolution observations of the emission from two HCO^+ transitions at $J = 3 - 2$ and $J = 4 - 3$ using the Atacama Large Millimetre Array (ALMA). From these observations, I highlight any potential chemical reactions which could form HCO^+ in the ejecta. I compare the spatial distribution of the $J = 3 - 2$ HCO^+ emission with that of the $J = 2 - 1$ CO emission and find that their brightest peaks are co-located and show a strong correlation suggesting that HCO^+ may form from CO. In order to form HCO^+, a moderate amount of hydrogen needs to be mixed into the carbon/oxygen rich regions of the ejecta. This may occur through hydrodynamical mixing of elements within the remnant before and during the supernova explosion. I speculate that, alongside large-scale, macroscopic mixing of clumps of elements known to occur in the remnant, forms of smaller-scale mixing from smaller elemental clumps down to atomic-level mixing at clump interfaces or boundary layers of different elements could also occur. To confirm the findings of this thesis, an extensive chemical network of HCO^+ formation in the remnant environment of SN 1987A is required. My HCO^+ analysis however, provides insight into the mixing and chemistry that can occur within the remnant which can open up new routes of hydrogen chemistry previously not considered for SN 1987A and potentially be applicable to other young supernova remnants.

Publications

FIRST AUTHOR PUBLICATIONS

H.M. Davies, et al. 2024/2025; *HCO^+ and the Effect of Mixing in SN 1987A*, In Prep

Contents

Acknowledgements

> *“Sometimes life is like a dark tunnel. You can’t always see the light at the end of the tunnel, but if you just keep moving... you will come to a better place"*
>
> Uncle Iroh *Avatar: Legend of Aang, 2006, season 2, episode 18.*

Acknowledgements

This work is supported by the STFC PhD studentship grant (grant number 2422911). I make use of the following python packages `NumPy`[*] (van der Walt et al., 2011), `SciPy`[†] (Virtanen et al., 2020), `MatPlotLib`[‡] (Hunter, 2007) and `Astropy`[§] (Astropy Collaboration et al., 2013; Price-Whelan et al., 2018; Astropy Collaboration et al., 2022). I also make use of CASA (CASA Team et al., 2022) and CARTA (Comrie et al., 2021) to clean and analyse the ALMA observations for this thesis. I also make use of NASA funded Astrophysics Data System[¶] under Cooperative Agreement 80NSSC21M00561.

Personal Thanks

The biggest thing I have learned from my PhD journey is that research is hard and that few people finish it without having some sort of struggle/stress/crisis. Due to this, it is incredibly important to have support and care from those closest to you to help you through it. I dedicate my acknowledgments to three people in particular. Firstly, my parents who’ve cheered me on throughout the years. My parents who kept me well fed and looked after during my first year of my PhD studies which was during the Covid-19 pandemic and have been understanding when I made the difficult decision to switch to an Mphil. Thank you Mam and Dad for giving me all your support and love over the years. Secondly I’d like to thank my partner Hidde, who has an endless supply of love and support. Thank you for everything! Thank you for being the voice of reason, introducing me to board games, kibbeling, Marble League and taking me on lovely hikes too. Thank you for all the lovingly-made cups of tea you’ve made me to keep me fuelled through the thesis writing purgatory. *De schildpad draagt klompen.*

I know I said I’d like to thank three people, but there are so many more I’d also like to thank! I’d like to thank my sister whom I’d always look up to and am very proud of. Thank you for

---

[*] `https://numpy.org/`

[†] `https://scipy.org/`

[‡] `https://matplotlib.org/`

[§] `https://www.astropy.org/index.html`

[¶] `https://ui.adsabs.harvard.edu/`

your multiple taxi rides to and from our parents' house. Yes, I will learn to drive soon, promise! I'd like to thank the folks at the Astro Department, they are unlike any other group of people I have met, they are friendly, helpful and all support each other, something invaluable that Cardiff University should be proud of. Cheers to the mighty Ralph, Sigurd, Varhis, Jerec, Muna, Y'ri, Fyros, Remy and of course, Pebbles! Or in other words, I'd like to thank my D&D group; The Stormbreakers, for providing me with a weekly sanctuary from the stresses of day-to-day life, it's been my absolute pleasure partaking in many an adventure with you! Thank you to my office mates who have been incredibly fun to work with! The communal biscuits and bits of interesting trivia here and there were greatly appreciated! I will miss the Office Olympics, but I guess it's only fair to let someone else win the left-over chocolates from the department advent calendars this year! I'd also like to thank the Cosmology group at Cardiff, you have made me feel very welcome participating with my partner in game nights and other personal achievements the group has celebrated together (albeit H_0 estimations using supernovae are not in agreement with Planck's H_0- yet!) I'd also like to thank Anita Richards, thank you for all the help you have given me in wrapping my head around ALMA data in the first year of my PhD, I greatly appreciate your kindness and patience. I'd also like to give special thanks to Phil Cigan, Anita Richards and Hidde Jense for the snippets of code used for this project.

CHAPTER 1

Introduction

> *"From this day forward, Flight Control will be known by two words: 'Tough' and 'Competent'. Tough means we are forever accountable for what we do or what we fail to do. We will never again compromise our responsibilities. [...] Competent means we will never take anything for granted. We will never be found short in our knowledge and in our skills.[...] When you leave this meeting today you will go to your office and the first thing you will do there is to write 'Tough and Competent' on your blackboards. It will never be erased."*

Gene F. Kranz: NASA 'White Team' Flight Director. *1967*

1.1 Supernovae

1.1.1 What is a Supernova?

Ancient civilisations in China and Japan described supernovae as 'guest stars' (e.g. Schaefer 2023) which were bright objects that looked like stars, that suddenly appeared in the sky. Some were so bright that they could been seen with the naked eye even during the day. Eventually, the brightness of these 'guest stars' diminished until they could be no-longer seen by our ancestor's eyes thus earning them their name. At present day, we know these 'guest stars' by another name: supernova explosions. These explosions are generally categorised into two types, Type I and Type II which arise predominantly from whether hydrogen emission lines are present in their early spectra. Type I supernova have no or very little hydrogen whereas Type II have hydrogen in their spectra. Broadly speaking, supernovae can occur in two ways, one being from thermonuclear explosions of white dwarf stars and the other being the core collapse of massive ($M \geq 8\,M_\odot$) stars. SN 1987A is the focus of this thesis which is a Type II, core collapse supernova (SN) remnant (e.g. Arnett et al. 1989 and references therein).

The cause of a core collapse SN is as follows: the star runs out of nuclear-burning fuel and inwardly collapses due to it being unable to support themselves against gravity. The collapse begins in the iron-rich core of the progenitor star, the collapse increases the core temperature to about 10^{10} K (e.g. Janka 2012) which creates a runaway reaction that disintegrates atoms of iron into atoms of helium and then into proton and electron constituents (e.g. Tayler 1994; Prialnik 2010; Janka 2012). The protons combine with the free electrons to create a gas heavy in neutrons. This gas becomes degenerate when a density of $\sim 10^{15}\,\mathrm{g\,cm^{-3}}$ (e.g. Prialnik 2010) is reached and the core suddenly stops collapsing. This results in the in-falling outer layers rebounding as a shock wave which blasts out the progenitor star's outer layers that surround the iron core. It is this emerging shock wave from the outer layers of the supernova remnant we see as the supernova explosion, and has a typical peak energy of 10^{51} erg (e.g. Janka 2012 and refs therein). It is this initial blast that forms the peak of a supernova light curve, it then exponentially decays. Then, the luminosity of the light curve is powered by the decay of radioisotopes present in the exploded material which displays a gradual decline from months to years (e.g. McCray & Fransson 2016 and references therein). What's left behind after the explosion is a supernova remnant; a nebulous collection of gas which is heated by subsequent shocks such as the reverse shock, radioactive emission from radioisotopes, and energetic winds of the compact object (e.g. Fransson & Kozma 2002; Hester et al. 2002; Fransson et al. 2024). This gas cools further to form molecules and dust in later years, whose emission can be analysed by astronomers. Supernovae hold importance to astronomers as they are suspected to be major contributors of dust to the interstellar medium since they can produce amounts of dust of the order of $10^{-1}\,M_\odot$ (e.g. Hoyle & Wickramasinghe 1970; Gomez et al. 2012; Matsuura et al. 2015) - the building blocks for star formation but also enriching the ISM with elements heavier than hydrogen and helium. The leftover neutrons in the core becomes a compact object, where it either becomes a neutron star, or if it has a mass greater than $\sim 2\,M_\odot$ will become a black hole (Tayler, 1994; Prialnik, 2010).

1.1.2 A Brief History of SN 1987A

In February 1987, light from a supernova explosion in the Large Magellanic Cloud (hereafter LMC) reached Earth (Kunkel et al., 1987). Due to this explosion being the first supernova (SN) of the year, it was named SN 1987A. Its fairly close proximity (at around 51 kpc; Panagia 1999), meant it was the brightest supernova event recorded in almost 400 years (Arnett et al., 1989). Even today, some thirty years after its initial explosion, it is still arguably the most studied object

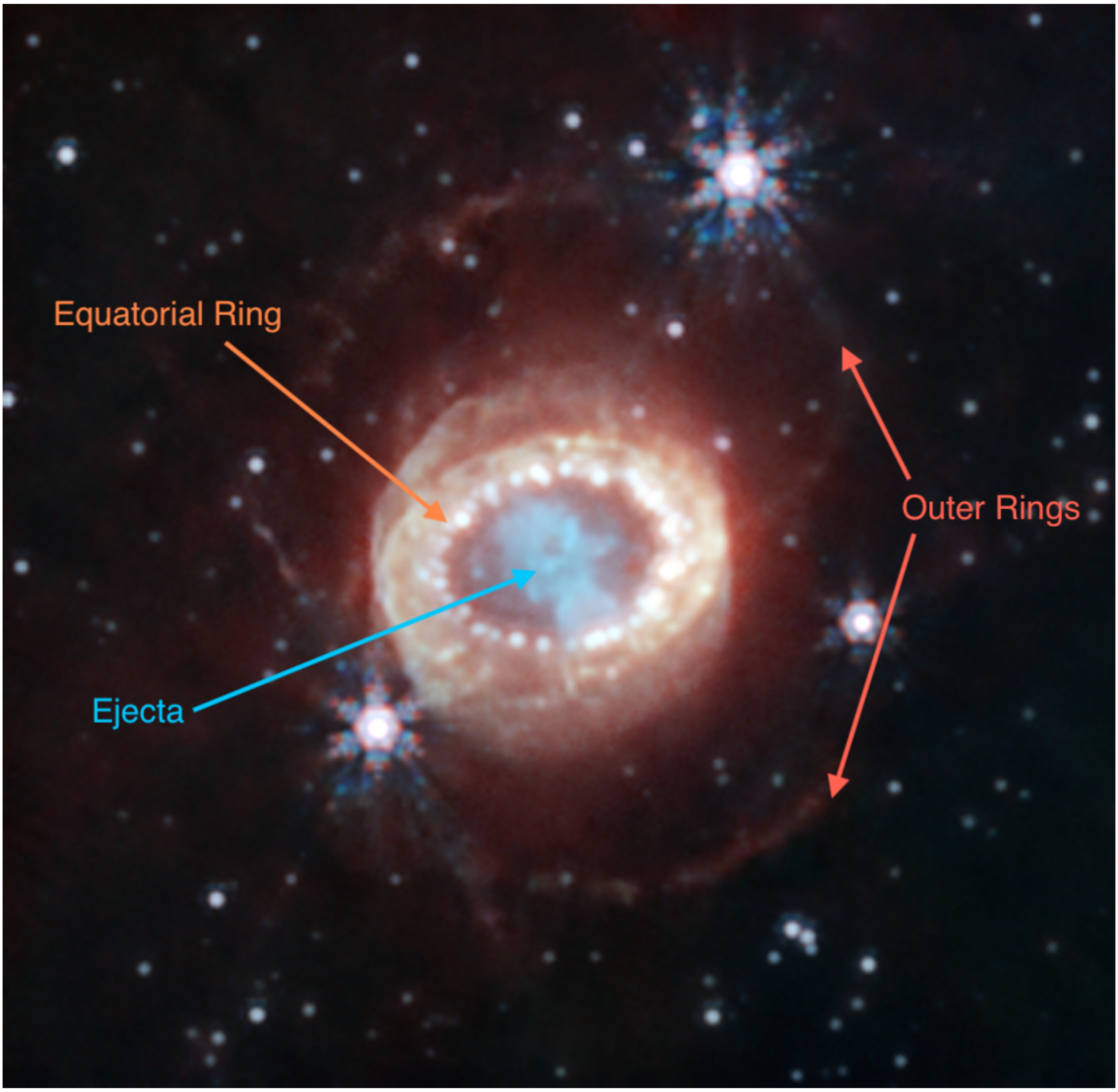

Figure 1.1. An image of the remnant of SN 1987A taken with the *JWST* NIRCam at wavelengths ranging from 1.5 to 4.4 μm. This image highlights the different structures found within the remnant. The blue central region indicates the ejecta, encircling this is the equatorial ring which consists of bright 'hot-spots' and more diffuse regions. There are also two faint outer rings most visible to the north and south of the image. This image also features three stars which are un-related to the supernova remnant. Courtesy of NASA, ESA, CSA, Mikako Matsuura (Cardiff University), Richard Arendt (NASA-GSFC, UMBC), Claes Fransson (Stockholm University), Josefin Larsson (KTH). Image processing done by Alyssa Pagan (STScI).

outside of our Solar System. An initial burst of neutrinos and the strong presence of hydrogen lines in its spectra indicated (Arnett et al., 1989) that this event was a Type II, core-collapse supernova (CCSN) explosion. Through lucky timing, astronomers were able to observe the explosion of SN 1987A (Kunkel et al., 1987) and observations of it have continued since, thus developing our understanding of young core collapse supernova remnants and how they evolve across time. This means that any on-going observations of young supernovae such as SN 1987A would greatly benefit our understanding of them. Additionally, CCSN rates in our galaxy are roughly 1-2 per century (Rozwadowska et al., 2021) therefore SN 1987A provides astronomers with a rare opportunity to study such a remnant in detail. Since its explosion, the remnant has been subject to shocks and radioactive heating which can power the emission from atoms, ions and molecules in the ejecta. Therefore an understanding of these energy sources can help uncover the chemical composition of the remnant.

The explosion type for SN 1987A was narrowed down even further to be a Type II-P supernova which is recognised by its distinctive plateau phase in the light curve which occurred a few days after the explosion. The gradual decay of the early light curve was caused by the radioactive decay of radioisotopes such as ^{56}Ni, ^{56}Co, ^{57}Co and ^{57}Ni (e.g. McCray 1993; Fransson & Kozma 2002). By 2,000 days after the SN explosion (hereafter $\mathrm{d_{SN}}$) the light curve is predominantly powered by ^{44}Ti (e.g. Fransson & Kozma 2002) which has a long half-life of 58.9 years (Ahmad et al., 2006). Its long half-life means its decay can provide heating for the dust, molecules, atoms and ions for a long time in the ejecta (e.g. Larsson et al. 2013; Matsuura et al. 2015; Jones et al. 2023).

The remnant of SN 1987A is comprised of two outer rings, an inner equatorial ring (ER) and the remnant's ejecta at its center as seen in Fig. 1.1. The material creating the rings was expelled from the progenitor star roughly 20,000 years before the supernova explosion (Crotts & Heathcote, 2000), what caused this to occur however is still up for debate with two possibilities being either a result of a rapidly-rotating single progenitor star (e.g. Chita et al. 2008), or the result of a binary merger (Morris & Podsiadlowski, 2007). Although, 3D hydrodynamical modelling favours a binary merger due to it very accurately replicating the triple-ring system of the remnant (Utrobin et al., 2021). A new and exciting phase of the remnant began in 1995 ($\mathrm{d_{SN}}$ $\sim$3,700), dense blobs of gas in the ER, began to brighten as a result of a blast wave interacting with them, causing emission in radio, optical, ultraviolet, mid-infrared and X-rays (e.g. Sonneborn et al. 1998; France et al. 2010; Frank et al. 2016; Larsson et al. 2019b). The origin of this blast wave comes from the dense, homologously expanding envelope of hydrogen, that was originally surrounding the progenitor star, reaching the reverse shock from the initial explosion of the supernova (McCray & Fransson, 2016). The blast wave encountering the ER caused a change in the dominant power source of the remnant from the decay of ^{44}Ti to X-ray heating thus affecting the emission, chemistry and composition of the ejecta. It was found that around d$_{\rm SN}$ ~6,000, these X-rays power some atomic and ionic line emission in the ejecta (Larsson et al., 2011). Roughly 5$\%$ of this energy goes into ionising hydrogen which creates Hα emission when it recombines (Fransson et al., 2013). Thus the Hα emission is powered by the energy deposition of X-rays in the ring (Larsson et al., 2013; Fransson et al., 2013; Larsson et al., 2016). The Hα emission forms a distinctive 'keyhole' morphology, where its distribution in the ejecta is edge-brightened due to the X-rays only being able to penetrate so far into the dense ejecta before getting absorbed or degraded by ejecta material (Fransson et al., 2013). Owing thanks to the advantage of Hα as a tracer of the X-ray energy deposition of the ejecta, and the fact that its morphology has not changed much since d$_{\rm SN}$=10,000 (Larsson et al., 2019b), its spatial distribution can be used as a marker for levels of strong ionisation in the ejecta. I explore this concept more in Section 2.2.7.

The flux of the low energy (0.2−2 keV) X-ray emission from the ring began to decline by d$_{\rm SN}$ ~10,000 (Ravi et al., 2024) indicating that the blast wave has started to travel past the ER to the circumstellar environment outside of the ring. Despite the initial decline of lower energy X-ray emission, in more recent times (d$_{\rm SN}$ ~12,000) it has began to plateau which can be tentatively explained if the outermost ejecta is now colliding with the reverse shock (Ravi et al. 2024 and references therein) and thus producing low energy X-ray emission just inside of the ER. The higher-energy X-rays however, still continue to increase even up to the latest X-ray observations at d$_{\rm SN}$ ~13,000. Thus, X-rays will continue to influence and alter the molecular chemistry in the ejecta as its expansion makes it more transparent to incoming X-rays (Fransson et al., 2013). Despite three decades' worth of observations and modelling, there is still much we don't know about the remnant, one of which is that the compact object left behind from the explosion has yet to be directly observed. Recent developments with state-of-the-art observatories such as ALMA and the *JWST* have shown that observations such as a bright blob of dust and transition molecules (such as CO $J = 2 - 1$ and SiO $J = 5 - 4$, $J = 6 - 5$ and $J = 7 - 6$) in the central region of the ejecta Cigan et al. (2019) and the presence of argon emission lines (Fransson et al., 2024) at the central regions of the ejecta are likely heated by the compact object, suspected to be a neutron star.

1.2 Molecules in SN 1987A.

The prime subject of this thesis is the analysis of the molecular emission of HCO$^+$ in the ejecta of SN 1987A. Molecules such as HCO$^+$ exist in the cooler ($\leq$10^3 K) and denser ($\geq$1 cm^{-3}) regions of the inter-stellar medium (ISM) (e.g. Williams & Viti 2013). Astronomers have analysed molecular emission from such regions and objects of the ISM to probe physical properties regarding these structures, such as the example of the line emission of rotational transitions of CO being a tracer of mass in giant molecular clouds (e.g. Tielens 2005; Williams & Viti 2013). SN 1987A has now entered a cool, molecular phase of its evolution (Kamenetzky et al., 2013), in which astronomers can analyse the emission of molecules to uncover properties of the remnant that previously were hidden. In CCSNe in general, it is suspected that some molecules such as SiO, are precursors to dust through molecular clustering and nucleation (e.g. Roche et al. 1991; Sarangi & Cherchneff 2013) which is important to understanding how remnants enrich the surrounding ISM with dust and heavier elements.

In SN 1987A emission from atomic lines exist too, in regions where ionising radiation is present such as UV and X-rays which break up any molecules that begin to form. This gives astronomers the chance to compare morphologies of molecular emission to morphologies of atomic lines to infer additional things about remnant, such as the dominant heating sources which power the emission (e.g. Larsson et al. 2011, 2013, 2016; Cigan et al. 2019; Larsson et al. 2019b). Comparisons of emission morphologies can be made between different molecules too, and have been used to support the evidence of the hydrodynamical mixing which occurred in the supernova remnant during the explosion (e.g. Abellán et al. 2017; Matsuura et al. 2017; Cigan et al. 2019) which will be discussed in more detail in Sect. 1.2.4. This thesis primarily attempts to answer how HCO^+ is formed in SN remnants through comparison with the morphology of the CO and SiO emission. Therefore it is necessary to give background lore on the past detections of molecular emission in the ejecta of SN 1987A before more specifically describing the 'key' molecule to this study; HCO^+.

1.2.1 Past Detections of Molecules

A detection of carbon monoxide in SN 1987A came at $d_{\rm SN}$=112 and was observed in the infrared spectra at 2.3 μm (e.g. Spyromilio et al. 1988 and references therein). This detection was subsequently confirmed with a second emission line of CO at 4.6 μm at $d_{\rm SN}$=192, making it the first molecule to be detected in SN 1987A and the first of its kind in all supernovae (Spyromilio et al., 1988). The CO line emission was of vibrationally-excited to the $\nu = 1$ and $\nu = 2$ transitions due to the high temperatures of the remnant at this early time at around $\sim 10^3$ K (e.g. McCray 1993). Modelling of the follow-up observations of the CO line emission at 2.3 μm found that the CO mass was estimated to be $\sim 10^{-3}$ $M_\odot$ (Liu et al., 1992). After CO, the next molecule to be detected was SiO. The mid-infrared spectra at $d_{\rm SN}$=164 began showing an excess around 8−9 μm (Aitken et al., 1988) which was attributed to emission from the vibrationally-excited ($\nu = 1$) SiO at 7.9 μm. By modelling the SiO line emission, its mass was calculated to be $\sim 10^{-6}$ $M_\odot$(Roche et al., 1991). The vibrationally-excited emission of CO and SiO continued until day ~600, when their emissions diminished from the spectra. This could be partly due to the temperature of the

CO gas (cooling to $\leq$10^3 K beyond d$_{\rm SN}$ $\sim$500 (Liu & Dalgarno, 1995)) no longer being able to excite the CO molecules to their vibrational transitions anymore (e.g. Kamenetzky et al. 2013 and references therein) and also partly due to the emergence of dust emission around this time which absorbs the light in the near-infrared (e.g. Roche et al. 1991). H$_2$ was predicted to begin forming as early as $d_{\rm SN}$ $\sim$100 (Culhane & McCray, 1995) and with the bulk of it forming around $d_{\rm SN}$ $\sim$400−1000. It was first detected however, at d$_{\rm SN}$=6,489 by Fransson et al. (2016) in the near-infrared (hereafter NIR) at 2.12 μm and 2.41 μm. Recent advancements with *JWST* resolved the spatial distribution of H$_2$ further to capture some of its extended emission (Matsuura et al., 2024). The spatial distribution of the H$_2$ emission shows a 'keyhole' shaped morphology similar to that of Hα. However, the locations of the brightest emission of Hα and H$_2$ differ greatly, with Hα being brightest in the west and H$_2$ emission being brightest in the south. It was found that H$_2$ emission is most likely powered by ultraviolet radiation from the ring or the decay of ^{44}Ti (Fransson et al., 2016; Larsson et al., 2023) which explains the difference between H$_2$ and Hα emissions where the latter is powered by X-ray energy deposition from the ring as mentioned in earlier in Sect. 1.1.2. This 'keyhole' shaped morphology consists of outer edges which are illuminated and there is a region of low emission at the central region of the ejecta (Larsson et al., 2011, 2013, 2016) which is called the 'hole'. This could be due to dust in the central regions obscuring the emission of H$_2$ and Hα (Cigan et al., 2019; Matsuura et al., 2024) or the fact that the X-rays which ionises the hydrogen for the Hα emission or the UV which generates the H$_2$ fluorescence resulting in its emission does not penetrate into the inner layers of the ejecta where the hole resides (e.g. Fransson et al. 2013; Larsson et al. 2013).

During the cool molecular phase of the remnant at later epochs, purely rotational transitions of CO and SiO were observed starting at d$_{\rm SN}$=9,174 (Kamenetzky et al., 2013). This includes the $J = 1-0$, $J = 2-1$, $J = 6-5$ and $J = 7-6$ transitions of CO at 115, 230, 691 and 706 GHz respectively. In addition, the line emission of $J = 5-4$ SiO was observed at 217 GHz. These observations of CO and SiO were continued across a larger frequency range (210−300 and 340−360 GHz), where a subsequent transition of $J = 6-5$ SiO was observed which occurs at 260 GHz (Matsuura et al., 2017). The line emissions were modelled to return masses of 0.02−1 M$_\odot$ and 0.04−2×10^{-3} M$_\odot$ for CO and SiO respectively (Matsuura et al., 2017). These masses are much larger than previous mass estimations of CO and SiO in the infra-red at early epochs. More recent developments of imaging CO, SiO and H$_2$ in the ejecta have enabled the emission morphology of the molecules to be viewed as a 3D spatial distribution (Abellán et al., 2017; Cigan et al., 2019; Larsson et al., 2019b). This was achievable due to the homologous expansion of the ejecta with time creates Doppler broadening of these molecular lines. This comes with an advantage that the molecules' velocity information can be used to determine their position within the remnant and hence these molecular distributions can therefore be viewed in 3D (e.g. Abellán et al. 2017; Larsson et al. 2019a). It was found that the CO $J = 2 - 1$ emission had a toroidal shape in the ejecta whereas SiO appeared to be more compact in distribution compared to CO (Abellán et al., 2017), the H_2 morphology consisted of a 'blobby' structure sitting south of the ejecta's centre (Larsson et al., 2019b).

1.2.2 HCO^+

HCO^+ is a molecular ion commonly found in the interstellar medium (ISM) (e.g. Williams & Viti 2013). It has been detected in proto-planetary disks (e.g. Dutrey et al. 2007; ALMA Partnership et al. 2015; Henning et al. 2024) and molecular clouds (Williams & Viti, 2013) where, in the latter environment it traces dense gas (Williams & Viti, 2013), the cosmic ray ionisation rate (Zhou et al., 2022; Tu et al., 2024) and the gravitational in-fall in molecular clouds (Yang et al., 2021). Therefore, this molecule is very versatile in probing the different conditions in different astronomical objects to further our understanding of them. Models of HCO^+ formation in molecular clouds indicate that it primarily forms via the formation route (Herbst & Klemperer, 1973; Oka, 2006; Panessa et al., 2023),:

$$\mathrm{H_3^+ + CO \rightarrow HCO^+ + H_2} \tag{1.1}$$

where H_3^+ is ultimately formed from cosmic rays ionising hydrogen gas via:

$$\mathrm{H_2} + \gamma \rightarrow \mathrm{H_2^+ + e^-} \tag{1.2}$$

and H_2^+ immediately interacts with H_2 to form H_3^+ giving the H_3^+ formation reaction below.

$$\mathrm{H_2^+ + H_2 \rightarrow H_3^+ + H} \tag{1.3}$$

The chemistry of molecular clouds is governed by the ionisation levels resulting from an external UV field (e.g. Tielens 2005). It is often the case that models of the chemical formation rates of molecules within molecular clouds are often investigated as a function of extinction (e.g. Panessa et al. 2023). This extinction of light through the cloud makes the light appear more red than expected which can then be measured by astronomers (e.g. Draine 2011). Panessa et al. (2023) found that 90% of HCO^+ forms at A_V=5 where Eq. 1.1 is the primary formation route. At lower extinctions (A_V=0.4–5) other HCO^+ formation pathways such as CO^++H_2 →HCO^++H and CH_2+O→HCO^++H are dominant but less HCO^+ forms from them overall. The time it takes for HCO^+ abundances in molecular clouds to reach stability is of the order of Myr (Herbst & Klemperer, 1973; Panessa et al., 2023), however, HCO^+ can also be found in molecular clouds undergoing shock interactions from nearby supernovae (Snell et al., 2005; Wootten et al., 2022; Zhou et al., 2022; Mazumdar et al., 2022; Tu et al., 2024).

There has only been one instance of HCO^+ forming in a supernova remnant environment which is in SN 1987A. The majority of the inner ejecta of SN 1987A has not yet interacted with its surrounding interstellar environment at the time of the HCO^+ observations which was detected on d_{SN} ~10,000 (Matsuura et al., 2017). This came as a surprise as chemical models of CCSNe such as SN 1987A either did not consider HCO^+ formation (e.g. Cherchneff & Dwek 2009; Sarangi & Cherchneff 2013) or have predicted very small abundances of it ($X_{\mathrm{HCO}^+} \sim 10^{-18}$) (Rawlings & Williams, 1990). This theoretical abundance equates to a mass of $1.6 \times 10^{-17}\,M_\odot$ if we assume the total mass of the ejecta is $\sim 16\,M_\odot$ where the 'core' has a mass of $\sim 6\,M_\odot$ and the envelope has a mass of $\sim 10\,M_\odot$ (e.g. Woosley et al. 1988b; Woosley 1988) The terms 'core' and 'envelope' are explained in Sect. 1.2.4 later. In reality, a far greater mass of $\sim 5 \times 10^{-6}\,M_\odot$ was calculated from observed HCO^+ line emission (Matsuura et al., 2017). This brings us to the primary aim of this Master's thesis; to investigate why and how has HCO^+ formed in such quantities in SN 1987A.

1.2.3 An Aside on Dust

The first observations of dust in SN 1987A came at d_{SN} ~615 (Wooden et al., 1993) which was roughly 500 days after the first CO detection. The dust formation in the ejecta at d_{SN} ~600 extinguished the optical and near infra-red (NIR) radiation in the ejecta and caused line emission in the optical and NIR to become truncated in the red-shifted velocities (McCray, 1993; McCray & Fransson, 2016, and references therein). Substantial quantities of cold dust in the ejecta of SN 1987A was detected at d_{SN} ~8,500 where observations were made in the far-infrared (Matsuura et al., 2011, 2015). Its total mass was calculated to be $\sim 0.6\,M_\odot$ which included a mixture of silicate and amorphous carbon dust. Understanding how dust forms in supernova is important as they may be vital contributors of dust in the interstellar medium. Additionally, more relevant to this thesis, dust is key to estimating the underlying continuum levels at the millimeter wavelengths in line emission data as it is reasonable to assume the continuum levels are due to dust, which can be modelled well using a modified blackbody fit. This is how I estimated the continuum levels in my HCO^+ observations in Section 2.2.3.

1.2.4 Mixing in SN 1987A

Before exploding as a supernova, the interior structure of the progenitor star of SN 1987A (which was around 16-22 $M_\odot$ (Arnett et al., 1989; Woosley, 1988)) is comprised of radially-stratified elemental burning zones. Elemental burning in stars, also known as stellar nucleosynthesis,

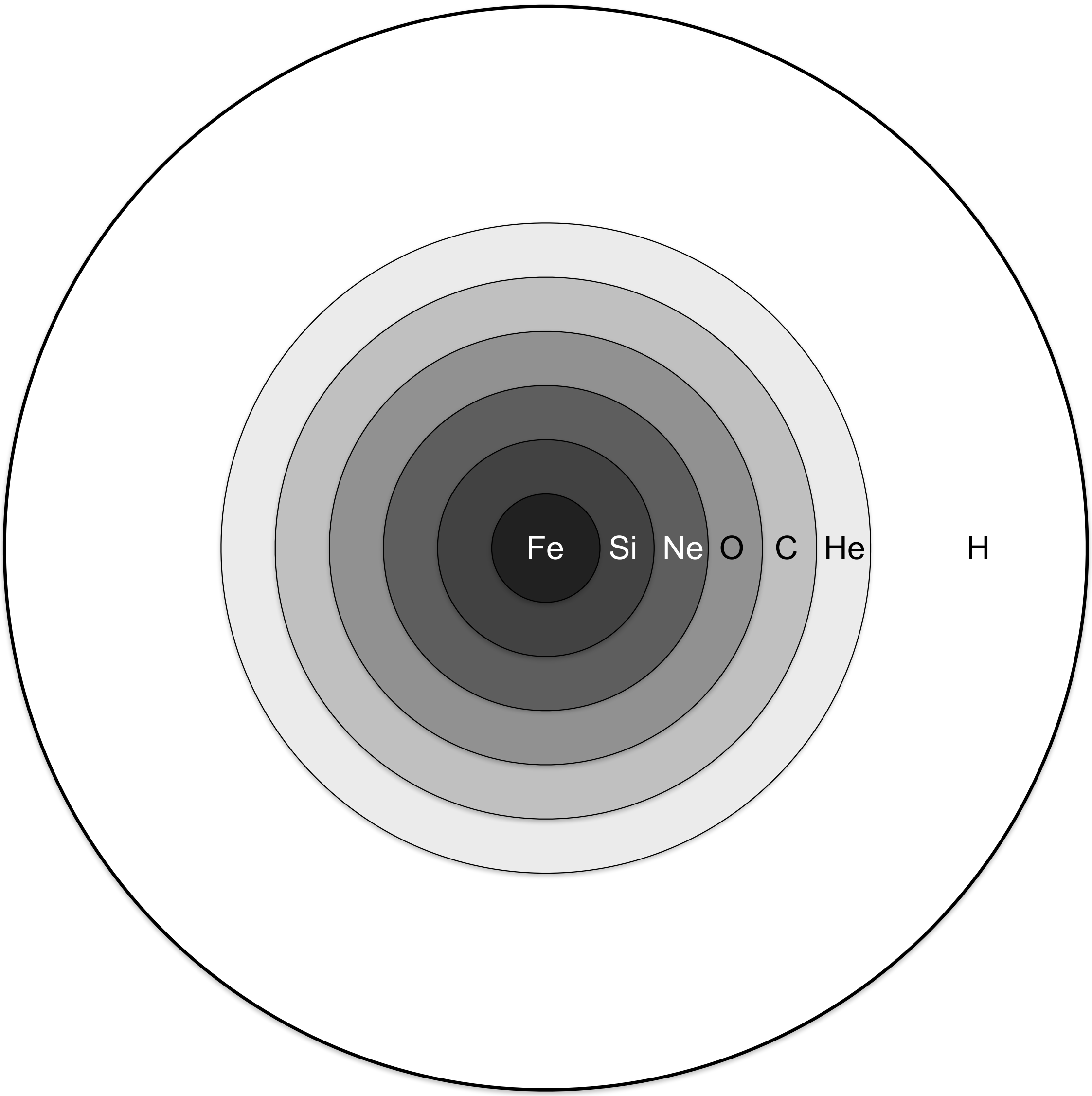

Figure 1.2. Schematic showing the elemental composition of a typical high-mass progenitor star before explosion. The radially-stratified zones are labelled with the most abundant element in that zone. Despite zones not being to scale, the hydrogen envelope was drawn larger to emphasise that the majority of the progenitor star's composition and mass is taken up by the envelope. This figure was created using the progenitor star structures modelled in (Woosley et al., 1988a).

is what powers a star, and involves the fusing of two particles (be it atoms or sub-atomic particles like protons) to create a single, heavier element. The burning of hydrogen is the predominant burning process for stars, which, through the proton proton chain and the CNO cycle, is ultimately fused into helium (e.g. Burbidge et al. 1957). The fusion of lighter elements into heavier ones occurs for all elements up to iron where it no longer becomes energetically viable for stellar nucleosynthesis to continue. Figure 1.2 shows the structure of a high-mass progenitor star where each burning zone is named after the most abundant element in that zone. Although it is not an elemental burning zone, there is an layer of iron at the central region of the star, is included in the figure. The next regions further out, consists of silicon, neon, oxygen and carbon. All these zones are collectively known as the core. Surrounding the outermost carbon zone is an inner envelope of helium and an outer envelope of hydrogen (e.g. Woosley et al., 1988a; Shigeyama & Nomoto, 1990). This onion-like, layered progenitor structure is often adopted as an unmixed ejecta scenario for core-collapse supernova (CCSNe) remnants in chemical network models (e.g. Nozawa et al. 2003; Sarangi & Cherchneff 2013) however, it is not truly representative of the structure of the ejecta of SN 1987A post-explosion. The first evidence that the progenitor structure may not be fully retained after the explosion came from the earlier-than-expected emergence of low energy X-rays ($\sim$ 16−24 eV) from d_{SN} $\sim$140−200 (Leising & Share, 1990; McCray, 1993). The X-rays originate from radioactive ^{56}Ni in the core and would get absorbed and degraded by the material surrounding the core before it has chance to escape the ejecta. It was expected that the low energy X-rays would emerge from the ejecta at later times when the expanding ejecta makes its central zones less opaque and thus enabling more X-rays to escape from it. Light curve models by Shigeyama & Nomoto (1990) found that this early emergence of X-rays can be explained if some of the ^{56}Ni has been mixed to the outer layers of the ejecta at expansion velocities of 3,000 km s^{-1} and additionally, they found that some mixing of the hydrogen from the envelope to the inner layers needs to occur to explain the broadness of the light curve peak around $\sim$80 days. This raised a question of what causes this mixing within the remnant, so early after the supernova explosion.

Macroscopic Mixing

It was theorised that large-scale mixing, known as macroscopic mixing, could disrupt the internal structure of the progenitor star after its supernova explosion and has been extensively researched in 3-D hydrodynamical models of CCSNe (Hammer et al., 2010; Wongwathanarat et al., 2015; Utrobin et al., 2015, 2019, 2021; Gabler et al., 2021). This mixing involves large mushroom and finger-like structures of heavy elements in the core such as nickel, iron, silicon and oxygen being launched outwards at velocities greater than the average expansion velocity of the ejecta at 1,000 km s^{-1} (Wongwathanarat et al., 2015). This mixing also creates ‘clumps’ which are defined as blob-like structures which have been separated from the expanding nickel sphere at the centre of the remnant*, whereas the mushroom and finger-like structures are still connected to it (Gabler et al. 2021 and see Figures 2, 7 and 11 in Wongwathanarat et al. 2015). Additionally, some of the hydrogen, present in the outermost envelope of the progenitor, is inwardly mixed due to some of it having lower velocities ($\sim$500 $\mathrm{km\,s^{-1}}$) compared to the average expansion velocity. This type of mixing is widely accepted to occur in SN 1987A due to the many observations which support it. Such observations include: the clumpy distributions of CO and SiO in the ejecta what have sizes of $\lesssim 10^{17}$ cm (e.g. Abellán et al. 2017; Cigan et al. 2019), the inward mixing of hydrogen (Kozma & Fransson, 1998; Jerkstrand et al., 2011; Fransson et al., 2016; Larsson et al., 2019a) and the presence of SN-origin dust grains on pre-solar system meteorites show that the dust mainly formed in a carbon-rich environment but have elements such as ^{44}Ti and ^{28}Si present within them too (Travaglio et al., 1999). The hydrodynamical models have also shown that macroscopic mixing is ultimately caused by Rayleigh-Taylor instabilities (hereafer RTi) which causes the giant clumpy structures of metals from the core to be launched outwards at high speeds. The RTis themselves are created when the SN forward shock encounters a change in the density gradient at boundaries between the nuclear burning zones left behind by the progenitor star (e.g. Herant & Benz 1992). In particular, it is the interfaces of the He/C+O and the He/H nuclear burning zones which cause the RTis and the greater the change in this density gradient, the larger the RTi (e.g. Wongwathanarat et al. 2015). The result of this macroscopic mixing leaves clumps containing the composition of the elemental zones they originated from, in elemental zones of a different composition; i.e. a clump of nickel transported via RTis to the hydrogen zone will still have a composition of predominantly nickel. Additional mixing on smaller scales is needed to mix the clump's elements with the elements of the surrounding zone the clump is in. A way that this could happen is discussed next.

Microscopic Mixing

Another form of mixing which could occur alongside macroscopic mixing is called microscopic mixing which mixes compositions of gasses of different elemental burning zones at the atomic/molecular scale. The possibility of microscopic mixing occurring in the remnant of SN 1987A however, is slightly problematic with early studies not supporting it. This is due the studies of modelling the early CO mass in the ejecta at days 112 to 574, showed that a microscopically mixed ejecta would lead to lower CO masses than what was observed (Liu et al., 1992; Liu & Dalgarno, 1995). Microscopic mixing would incorporate more of the destructive ion He^{+} into the inner C+O layers of the ejecta which is the dominant reaction that to dissociates CO at these early epochs ($\mathrm{d_{SN}}$<1000)

---

*called the 'nickel bubble'

(e.g. Lepp et al. 1990; Sarangi & Cherchneff 2013). Due to this, there is little literature that does consider scenarios of microscopic mixing in the remnant of SN 1987A. One study, Nozawa et al. (2003), investigates a uniformly-mixed ejecta on dust synthesis in Population III supernova remnants[†]. This uniformly-mixed ejecta is a combination of extensive macroscopic and microscopic mixing where the chemical composition of elements and molecules is the same throughout the ejecta of the remnant. They found that the diversity of dust species in a uniformly mixed ejecta is less than that of an unmixed ejecta. Despite this, microscopic mixing may aid in the small-scale mixing of elements at the interfaces of the large-scale clumps from other zones of different composition to improve the chances of creating hybrid molecules using elements from different nuclear burning zones.

Pre-SN Mixing

There is the possibility that some convective mixing at the boundaries of elemental burning zones could take place before the progenitor star goes supernova. A study by Arnett et al. (2007) modelled the effect of turbulent convective mixing on a non-rotating, $20\,M_\odot$ stellar model of solar metallicity. It was found that convective mixing can distort the boundaries of nuclear burning zones, causing some elemental material of outer elemental burning zones to get mixed further into the star. Furthermore, it was found that this mixing at the boundaries becomes more pronounced with stars of higher progenitor mass (Frey et al., 2013). The star's rotation can also induce some mixing at the interfaces of nuclear burning zones, in particular, the He/H interface (e.g. Farrell et al. 2021). These other smaller-scale mixing scenarios can also lead on to create hybrid molecules made up of elements from different burning zones such as HCO^+ some time after the supernova explosion.

1.3 Observing Molecules

This following section describes how molecular emission is observed in the radio and sub-mm regime, and how physical properties of the molecules are found using a concept known as radiative transfer and through the use of statistical modelling. This makes observing and analysing the HCO^+ emission possible for this Master's thesis. Firstly, I describe the ALMA observatory and the concepts of radio interferometry which was used in order to observe and create high-resolution images of the HCO^+ emission in SN 1987A. Secondly, I cover the main concepts in radiative transfer, which enables physical properties such as temperature and column density of molecules

---

[†] A Population III supernova remnant is the supernova explosion of a Population III star, which have very low metallicities.

to be determined from observations of molecular emission in SN 1987A. Finally, I describe the the chi-squared goodness of fit test and confidence intervals which aid in the analysis of my HCO^+ data to uncover best-fitting temperature and column density from my observations of HCO^+ line emission.

1.3.1 ALMA and Inferferometry

In the following section, I introduce the ALMA observatory and the imaging techniques used to make high-angular resolution observations of HCO^+ in SN 1987A possible. I briefly discuss the problem of achieving a high angular resolution in radio and sub-millimetre (sub-mm) frequency observations and how observatories such as ALMA, use a concept known as aperture synthesis to resolve this issue. I also discuss how science-grade observational images are created using radio interferometry.

The ALMA Observatory

Sub-mm emission of the ejecta was imaged using the Atacama Large Millimetre/sub-millimetre array (hereafter ALMA) in Chile. ALMA is a ground-based observatory which collects radio and sub-mm signals in 9 observing bands which sit in the atmosphere transparency windows in Earth's atmosphere (Cortes et al., 2024). Its current frequency observing range spans from 35−950 GHz (or 8.5−0.3 mm in wavelength) with another observing band (Band 2) with frequency range of 67−116 GHz is planned to be operational in the near future (ESO & The ALMA Partnership, 2023). This observatory uses the concept of radio interferometry to image astronomical objects with high sensitivity and resolution. This involves an array of multiple antennas[‡], spread over a large collecting area spanning several kilometers, that observe the same astronomical object at the same time (e.g. Asaki et al. 2023). This set-up improves the resolving power of the telescope array which is otherwise limited by aperture diameter, D_A, and the wavelength λ of light it observes. This is given by the Rayleigh criterion given below.

$$\Theta_{\mathrm{res}} = \frac{1.22\lambda}{D_A} \tag{1.4}$$

This means a structure or object which has an angular scale less than the telescope's angular resolution, Θ_{res} will not be resolved. A set-up of multiple antennas working as one is called aperture synthesis and further improves the imaging capabilities in radio/sub-mm astronomy. In line with this study, ALMA is known for being able to spatially resolve sub-millimetre emission lines from

---

[‡] ALMA has 66 at the time of writing (Cortes et al., 2024)

excited atoms, ions, molecules, and isotopologues (e.g. for SN 1987A, Kamenetzky et al. 2013; Abellán et al. 2017; Matsuura et al. 2017; Cigan et al. 2019). Furthermore, a unique advantage of radio interferometers is that the arrays of antennas can move into various configurations to suit the imaging needs of the object, i.e. a configuration across a large area can be used to spatially resolve small-scale structures in astronomical objects with angular resolutions down to a few milli-arcseconds whereas a more compact configuration is more sensitive to emission from extended objects spanning a few arcseconds across the sky (Cortes et al., 2024). For SN 1987A, five different array configurations are used to give the best results of the data which are described more in Chapter 2.

Radio Interferometry and Aperture Synthesis

As mentioned in the previous section, the ALMA observatory uses aperture synthesis across multiple antennas to improve the observatory's angular resolution and sensitivity. The basic principles of radio interferometry and aperture synthesis are discussed here with the help of a simple set-up of two antennas to describe how observations are made with the ALMA observatory. To understand the advantage of using radio interferometry to improve the angular resolution of an image, consider an idealised antenna, A_1, with an aperture size of D_A pointed to an astronomical object emitting coherent light of wavelength λ. This light reaches Earth as plane waves which are intercepted by the aperture of the antenna. It is often the case that these wavefronts arrive at the antenna at some angle respective to the antenna's pointing axis and therefore reach different parts of the antenna's aperture at slightly different times. This wavefront is therefore described as off-axis (Cortes et al., 2024). This has an affect on the sensitivity of the instrument. The parabolic shaped aperture focuses the wavefront to the antenna's receiver at the centre of the aperture. If the wavefront is off-axis however, then this wavefront arrives at the receiver at different times due to some path-lengths of the focused signal being longer than others. The emitted light from the astronomical object behaves like a sinusoidal wave, therefore, this difference in arrival times of the wavefront at the receiver, results in a difference in phase of the wavefronts which causes an interference pattern to be generated at the receiver. The amplitude of the light-signal received at the antenna decreases with increasing off-axis angle which makes the receiver output have a point-spread function (PSF) with sidelobes (e.g. Rieke 2012; Cortes et al. 2024). Nodes and peaks are generated in the sidelobes of the PSF due to destructive and constructive interferences of the off-axis light respectively. The primary peak of the PSF, is centred at an off-axis angle of 0°, is known as the primary beam of an antenna. Its full-width at half maximum (FWHM) in radians is given by $\Theta_{\mathrm{FWHM}} = 1.02\lambda/D_A$ (Wilson et al., 2013; Cortes et al., 2024). As mentioned in the previous sub-section, the Rayleigh criterion given by Eq. 1.4 also depends on the PSF as it is the half of the width of the primary beam up until its first nodes which were created by destructive interference. Adding a second, identical antenna, A_2, that collects light in unison with A_1 improves the angular resolution of imaging the object through a concept known as aperture synthesis (Rieke, 2012; Wilson et al., 2013; Asaki et al., 2023; Cortes et al., 2024). A setup of the two antennas is shown in Fig. 1.3, the two antennas separated by a distance, called a baseline, b, and are pointed to the astronomical object of wavelength, λ, now act as if they are one antenna where its aperture is diameter b. Hence, the resolution of the observation is now: $\Theta_{\rm res} = 1.22\lambda/b$, and if $b >> D_A$, the angular resolution of the observations greatly improve. Improving the angular resolution means observatories, such as ALMA, can probe to even smaller scales in astronomical objects which can reveal more small-scale structures of astronomical objects to astronomers. The observed signal from each antenna is converted as a voltage output which is later fed to a correlator (e.g. Rieke 2012; Wilson et al. 2013; Cortes et al. 2024).

Having multiple antennas acting as one can lead to further losses in the collected light from the astronomical object. This is due to the geometric positioning of the antennas and due to the wavefront nature of light from the astronomical object. If the astronomical object isn't observed at a time when it is not directly on the zenith, the wavefronts will arrive at the antenna array at an angle θ from the zenith line. This causes a delay to some signals being processed at the observatory's correllator which multiplies and time-averages each antenna's voltage outputs. This set-up is highlighted in Fig. 1.3 which shows the wavefront will encounter antenna A_1 before A_2 hence there is a time-delay of the incoming wavefront to the antennas. Due to the light being incoherent when they reach the correlator it also leads to them destructively interfering with each other which ultimately results in a loss of signal. To remedy this, an artificial time delay in the electronics of each antenna is induced ensuring all signals arrive at the correlator at the same time (Cortes et al., 2024). Thanks to simple geometry, shown in Fig. 1.3, and factoring in that light travels at c, this artificial time delay, t_g, is given below (Cortes et al., 2024).

$$t_g = \frac{b\sin(\theta)}{c} \tag{1.5}$$

Which can simplify to $t_g = \dfrac{b \cdot s}{c}$, where s is the direction vector to the astronomical object (e.g. Wilson et al. 2013).

Eventually, these output voltages between pairs of antennas are fed into the correlator and are Fourier transformed into a distribution of 'visibilities' which are positional points plotted on the uv plane; the more antenna pairs, the more visibility points are plotted on this plane (Cortes et al., 2024). The uv plane is a cartesian plane of coordinates in frequency units projected on the sky, where v is the north-south direction and u is the east-west direction (e.g. Rieke 2012). The positional information of points in the uv plane arise from small deviations in phase of the voltage outputs. The visibility data points themselves hold information of the amplitude and phase of

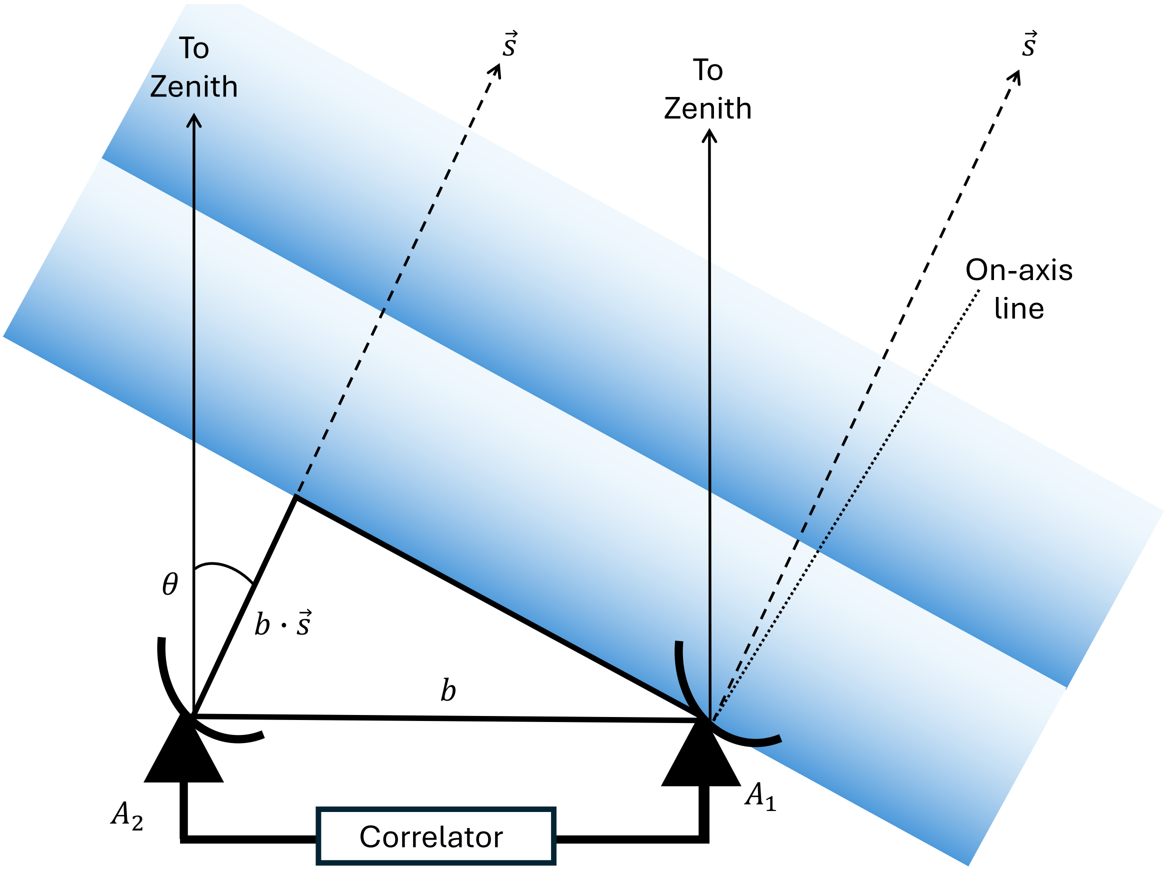

Figure 1.3. A diagram of an interferometer consisting of two antennas A_1 and A_2. Both are oriented close to the direction of an astronomical object whose vector is given by s. The two antenna are separated by a distance b, called the baseline. The blue-shaded regions show incoming wavefronts from the astronomical object. This figure also shows the geometrical delay in the wavefront reaching A_2 compared to A_1. Each antenna output will get transferred to a correlator which multiplies and time-averages the data (e.g. Cortes et al. 2024).

light at that particular point in the sky. More visibility data points can be placed on the uv plane if the antennas image the source multiple times during the day thanks to the Earth's rotation, this can be done provided the light from the astronomical object does not vary considerably across the times when it is observed by the array. These visibilities can then be converted to images which reflect the true sky observations through a process called 'cleaning' which I will discuss in the subsequent sub-section.

Interferometry Image Cleaning

The intensity of light as it appears on the sky, also called the sky brightnesses, can be calculated from the visibilities through use of the van Crittert-Zernike theorem (e.g. Högbom 1974; Cortes et al. 2024) which states: the Fourier transform of the visibilities is directly proportional to the intensities in the sky. This is also shown by the equation below.

$$\mathcal{V}(u,v) \propto \iint I(l,m) \exp 2\pi i(ul+vm) dl dm \tag{1.6}$$

$\mathcal{V}$ is the set of visibilities on the uv plane, and $I(l,m)$ is the sky brightness at a location on the sky described by the directional cosines l and m. The van Crittert-Zernike theorem in Eq. 1.6 is what enables the creation of high-angular resolution images from radio interferometry observations. The inverse Fourier transform of a completely covered uv plane with visibilities will result in an image of the sky brightnesses of an astronomical object where its resolution is set by the primary beam P_b (Högbom, 1974) as discussed in the previous section. It is often the case however, that these visibilities do not cover the uv plane completely and that there are 'gaps' between visibilities. The resulting image is therefore convolved with an additional synthesised PSF, denoted S_b called the 'dirty beam'. This generates an image of the observations that has artefacts within it arising from the sidelobes from the dirty beam (Högbom, 1974), this image is called a 'dirty image'. These artefacts are seen as artificial structures in the images and therefore it is difficult to use these images for science and so, they need to be removed from the image. In radio and sub-mm astronomy, a process called 'cleaning' helps observers to separate out the artefacts from the image and get a better representation of the object one is imaging. Cleaning involves finding the maximum brightness on the dirty image and mapping it on a blank model image as a point source. This maximum brightness corresponds to the maximum point on the primary peak of the dirty beam (Högbom, 1974). This model image is then convolved with the dirty beam and Fourier-transformed back to represent this point on the uv plane. This point on the model's uv plane is subtracted from the dirty image's set of points on the uv plane. The dirty image is then inverse Fourier transformed back to being an image. This time, the brightest intensity on the image is missing and it is now called a 'residual image'. This process is repeated again and again with the sequential largest brightnesses in the residual images, until a certain noise threshold is reached, which is commonly user defined. This process fills out the model image with the locations of the brightest point sources of the dirty image without the artefacts of the dirty beam. Lastly, this model image is convolved with a new beam modelled from the dirty beam but without the sidelobes, called a 'clean beam', which then gives the happy astronomer their science-ready, astronomical images. I use the CLEAN method to de-convolve the 'dirty beam' from my HCO^+ observations in Sect. 2.1.1.

1.3.2 Radiative Transfer

Light interacts with matter, whether it be the Yarkovsky effect slightly changing the trajectory of asteroids (e.g. Bottke et al. 2006) to sunlight heating one's greenhouse at the end of the garden. Astronomers have used such interactions to their advantage through the use of radiative transfer: a set of equations describing how light travels through astronomical objects such as clouds, atmospheres and SN remnants. So powerful are these equations, that astronomers can infer physical properties of the light-emitting material, such as the emitting material's column density, temperature and optical depth. I describe the principles of radiative transfer, from its general equation, to the limiting cases astronomers apply to simplify in solving the radiative transfer equation. I then describe how astronomers use these equations of radiative transfer to calculate the physical properties of gasses such as temperature and column density in an astronomical object.

General Equation of Radiative Transfer and Definitions

The intensity of light can change as it travels through a cloud due to its photons interacting with the cloud's material which I'll generally call a medium. This change in the light's intensity, I_ν, at a certain frequency, ν, from a source, as it travels through a medium, of optical depth, τ_ν, can be described by the general form of the radiative transfer equation below (e.g. Rybicki. & Lightmann 1979).

$$I_\nu = I_{\nu,0} e^{-\tau_\nu} + \int_0^{\tau'_\nu} S_\nu e^{-(\tau_\nu - \tau'_\nu)}. \tag{1.7}$$

$I_{\nu,0}$ is the intensity of a source of light before travelling a τ_ν through the medium and $S_\nu = \frac{j_\nu}{\alpha_\nu}$, the ratio of emissive and absorbing properties of the medium and is named the source function. The emission coefficient, j_ν, and the absorption coefficient, α_ν, account for the increase or decrease of the light's intensity through the cloud respectively. The source function relates the macroscopic properties of the medium to the microscopic properties, as j_ν and α_ν depend on the number densities of molecules occupying each energy level, as well as the energy of each level (e.g. Rybicki. & Lightmann 1979; Spitzer Jr. 1998). The optical depth defines the absorbing power of a medium the light is travelling through, it is a frequency-dependent quantity which describes the average path of a photon through a medium before getting absorbed or scattered (e.g. Rybicki. & Lightmann 1979). The absorption coefficient, is better defined by the optical depth, τ_ν where the change in optical depth is given by: $d\tau_\nu = -\alpha_\nu ds$ (e.g. Rybicki. & Lightmann 1979). A medium is usually defined as optically thick or thin, if $\tau_\nu \geq$1 then a photon travelling through a medium has a high chance of being absorbed by the medium and therefore medium is optically thick. If $\tau_\nu \leq$1 then a photon can travel through the medium and suffer little to no absorptions by the medium, and therefore the medium is optically thin.

If S_ν is constant across the medium, then the radiative transfer equation simplifies to (Rybicki. & Lightmann, 1979):

$$I_\nu = I_{\nu,0}e^{-\tau_\nu} + S_\nu(1 - e^{-\tau_\nu}). \tag{1.8}$$

.

Specifically for this Master's project, I assume the region of gas in which HCO$^+$ exists, in the remnant of SN 1987A, is mostly molecular. Molecules exist at multiple levels (N_E) of energy (the same can be said for a medium consisting of atoms or ions but they are not the focus of this Master's thesis). They can de-excite to a lower (denoted level i) or excite to a higher (denoted level j) energy states within each level N_E. The cause of these excitations and de-excitations comes from collisions, relaxations of molecules and absorption of light emitted from other relaxing molecules. This understanding of the molecular energy levels and how they are populated have enabled astronomers to use molecular emission (i.e. the 'light') and solve the RT equation. To calculate S_ν in the general radiative transfer equation, the help of Einstein is needed, where he formulated three cases on how a molecule can go from one state to another (Einstein, 1916). These are via spontaneous emission (A_{ji}), the act of a molecule emitting a photon and relaxing down to a lower energy state, stimulated absorption and emission (B_{ij} and B_{ji}), where an effect causes a molecule to excite/de-excite to a different energy state and collisional absorption and emission (C_{ij} and C_{ji}) where a molecule's excitation or de-excitation is caused by a collision with another molecule. These coefficients are related to the absorption and emissivity coefficients of the medium in Equations 1.9 and 1.10.

$$\alpha_\nu = \frac{h\nu}{4\pi}\phi_\nu(n_iB_{ij} - n_jB_{ji}) \tag{1.9}$$

$$j_\nu = \frac{h\nu_0}{4\pi}n_jA_{ji}\phi_\nu \tag{1.10}$$

Where ϕ_ν describes the shape of the line profile of an emitting molecule, commonly modelled as a gaussian function and assumed to be the same shape for both absorption and emission cases (Rybicki. & Lightmann, 1979). The quantities n_i and n_j refer to the level populations of molecules in energy states i and j of level N_E respectively. Using these Einstein coefficients, the RT equation in Eq. 1.8 can therefore be re-written as:

$$\frac{I_\nu}{ds} = \frac{h\nu}{4\pi}\bigg((n_i B_{ij} - n_j B_{ji})\phi_\nu I_\nu + n_j A_{ji}\phi_\nu\bigg) \tag{1.11}$$

If the level populations of each molecule are known, then the radiative transfer equation can be solved. The level populations, n_i and n_j, are described via the Boltzmann energy distribution below which relates them to the excitation temperature, T_{ex}, energy levels, E, and upper and lower statistical weights, g_i and g_j, of each level, as shown below.

$$\frac{n_j}{n_i} = \frac{g_j}{g_i}\exp\frac{-(E_j - E_i)}{k_{\rm B}T_{\rm ex}} \tag{1.12}$$

Local Thermodynamical Equilibrium

Local Thermodynamical Equilibrium (hereafter LTE) is where one assumes that the energy levels of the emitting material inside a particular region can be described with a single temperature; hence, a molecule at one region of the medium would be in thermodynamical equilibrium with every other molecule within the same region. The local homogeneity of temperature comes with its advantages, where the temperature required to excite molecules $T_{\rm ex}$ is equal to the kinetic temperature of the molecular gas $T_{\rm k}$, therefore Eq. 1.12 holds when $T_{\rm ex}$ is changed to $T_{\rm k}$. This can enable astronomers to easily infer $T_{\rm k}$ of the gas and thus inferring the physical conditions of the medium via the use of a population diagram, which is described later on in this section. It is assumed that molecular emission in LTE is dominated by collisional excitations (e.g. Spitzer Jr. 1998; Williams & Viti 2013). The source function can be described by a blackbody through Kirchhoff's law shown in Eq. 1.13, but only if temperature is constant across the region of the medium (e.g. Rybicki. & Lightmann 1979; Spitzer Jr. 1998; Draine 2011).

$$S_\nu = \frac{j_\nu}{\alpha_\nu} = B_\nu(T) \tag{1.13}$$

Therefore, the general solution to radiative transfer equation from Eq. 1.7 in LTE conditions can be written as:

$$I_\nu = I_{\nu,0}e^{-\tau_\nu} + B_\nu(T_{kin})[1 - e^{-\tau_\nu}] \tag{1.14}$$

However, I_ν itself can be described with a blackbody function at a certain brightness which in which $B_\nu(T_b) \equiv I_\nu$. This temperature T_b is called the brightness temperature (e.g. Draine

2011). Following the homogeneity of temperature in LTE, $T_b \equiv T_k$. In the radio and sub-mm regime however, the Planck function is approximated as the Rayleigh-Jeans blackbody function (i.e. $B_\nu = \frac{2k_B\nu^2}{c^2}T$) as intensity of light in this regime follows a linear relationship with ν. To distinguish this specific case from the more general T_b, the temperature in the Rayleigh-Jeans regime is called the antenna temperature, T_a. It has the relation to specific intensity below:

$$T_a = \frac{c^2}{2k_B\nu^2}I_\nu \tag{1.15}$$

This relation above is advantageous to millimetre and sub-mm astronomers is due to T_a, is directly observed by observatories operating in the sub-mm (this is also true for ALMA (Cortes et al., 2024)). This antenna temperature is key to estimating the physical parameters of the molecular emission which will be discussed later on in this section.

Non-Local Thermodynamic Equilibrium

We cannot apply LTE to all astronomical objects in the ISM, as the energy distribution of regions in astronomical objects may not have a single temperature to describe them. This may be also true for SN 1987A as the expansion across time decreases the density of its gas, meaning the gas is less dominated by collisions and therefore more likely to be non-LTE. Additionally, the simplification of the blackbody function in place of S_ν cannot be applied. It is often that instead conditions of Non-Local Thermodynamic Equilibrium (non-LTE) which are applied, which assume that multiple different temperatures across a region in a medium can describe the emission.

The level populations n_i and n_j st each energy level N_E are characterised in Eq. 1.12 may have different values of $T_{\rm ex}$ (e.g. Williams & Viti 2013). Therefore the radiative transfer equations in non-LTE circumstances are often solved by models of radiative transfer that calculate the individual level populations of molecular transitions through use of statistical equilibrium (e.g. van der Tak et al. 2007). Statistical equilibrium assumes that n_i and n_j remain constant across time and can be defined using Einstein coefficients (e.g. van der Tak et al. 2007; Williams & Viti 2013) For an atom of only two excitation levels, this is defined as the equation below (Tielens, 2005).

$$0 = -n_i\bigg(C_{ji} + B_{ij}J_\nu\bigg) + n_j\bigg(A_{ji} + B_{ji}J_\nu + C_{ij}\bigg) \tag{1.16}$$

J_ν is the average intensity of the medium and is characterised by the relation: $J_\nu = \frac{1}{4\pi}\int I_\nu\, d\Omega$ (e.g. Rybicki. & Lightmann 1979; van der Tak et al. 2007). How physical properties of the gas are derived from non-LTE conditions are described in the following sub-section.

Determining Physical Properties of Molecules from RT Equations.

The physical properties such as the column density and temperature of the emitting medium can be derived through a LTE and Non-LTE case. I shall firstly describe the LTE case. As mentioned before, observatories that operate in the radio and sub-mm regime often record emission from an astronomical object as a temperature called the antenna temperature, T_a. which is defined in Eq. 1.15. Note, in Sect. 1.3.1 and 2.1.1 these get converted into an intensity by comparing the antenna temperature of another astronomical object whose flux is well-known (e.g. Cortes et al. 2024). The antenna temperature is related to the physical properties of the emitting molecular gas via the equation below (e.g. Goldsmith & Langer 1999; Williams & Viti 2013):

$$T_a = \frac{hc^3 N_u A_{ul}}{8\pi k \nu^2 \Delta\nu} \left(\frac{\Delta\Omega_S}{\Delta\Omega_A}\right) \left(\frac{1-e^{-\tau}}{\tau}\right) \tag{1.17}$$

Where N_u is the column density of the upper level of a molecule, ν is the frequency of the molecular transition and $\Delta\nu$ is the frequency width of the molecular line of a specific transition and $\Delta\Omega_S$ and $\Delta\Omega_A$ are the solid angles of the emission of the source and the projection of the antenna on the sky respectively. This solid angle ratio can be equated to 1 if the emission from the source fills the beam of the antenna (Goldsmith & Langer, 1999). This relates to the molecular line intensity via $W{=}\int T_a \Delta\nu$ so therefore the column density of the upper level of a molecule is related to its line emission via the equation below.

$$N_u = \frac{8\pi k \nu^2 W}{hc^3 N_u A_{ul}} \left(\frac{\Delta\Omega_S}{\Delta\Omega_A}\right) \left(\frac{1-e^{-\tau}}{\tau}\right) \tag{1.18}$$

From this, we can derive the column density of the upper level of a molecule. In an optically thin case (τ<1), then the right-hand term containing the optical depth can be approximated to one. In an LTE environment, the column density of the upper level is related to the total column density N_{tot} via the equation below (Williams & Viti, 2013).

$$N_u = \frac{N_{\mathrm{tot}}}{Z} g_u \exp\left(\frac{-E_u}{kT_k}\right) \left(\frac{\tau}{1-e^{-\tau}}\right) \tag{1.19}$$

The right-hand bracket is a correction factor for the optical depth, this is required as the upper level and total column density for an optically thick medium would be underestimated without this correction term (Goldsmith & Langer, 1999), this optical depth correction term is denoted C_τ hereafter. Z is the partition function, which is the sum of all the lower level column densities of the emitting molecule (e.g. Rybicki. & Lightmann 1979; Goldsmith & Langer 1999) and has the form: $Z = \sum g_i \exp \frac{-E_i}{kT}$. E_u is the energy required to excite the medium from a lower to the upper energy level. Therefore, in LTE, observations of emission from only one transition of an emitting medium can lead to the column density of the emitting medium.

The kinetic temperature T_k can also be found if one has observed multiple transitions of an emitting molecule or atom in the medium, but it is usually done through means of a population diagram (e.g. Goldsmith & Langer 1999). This involves taking the natural logarithm of Eq. 1.19. Due to the relationship between the upper level column density and the integrated line intensity of the emitting medium in Eq. 1.18 leads to the resulting equation below.

$$ln\left(\frac{aW}{g_u}\right) = \frac{-E_u}{kT_k} - ln(N_{\mathrm{tot}}) - ln(Z) - ln(C_\tau) \tag{1.20}$$

Where $a = \dfrac{8\pi k\nu^2}{hc^3 A_{ul}}$. Therefore a diagram can be plotted of the left-hand term versus the upper energy levels, E_u. The gradient of the fitted line through the plotted points is equal to $-T_k^{-1}$ and therefore the kinetic temperature can be found.

If the gas is assumed to be in Non-LTE, then we cannot apply the LTE methodology to a Non-LTE medium. Instead, each level population must be calculated using Eq. 1.16 (van der Tak et al., 2007; Williams & Viti, 2013). For radiative transfer equations to be solved using the Non-LTE condition, the kinetic temperature, T_{kin}, column density, N_{col}, and information regarding the collisional data of the molecules must be known. Due to this, it is often the case that radiative transfer models are used (e.g. RADEX van der Tak et al. 2007), which take T_{kin}, N_{col} and the collisional information and iteratively solve the radiative transfer models to calculate the line intensities of molecular transitions which are then compared to observational line intensities. Thankfully, online databases such as LAMDA (Schöier et al., 2005) exist which provide the statistical weights, Einstein coefficients and collisional rates of commonly observed molecules in the ISM. This is met with a complication however, the level populations n_i and n_j must be calculated for each N_E-level of the molecule at each location in the medium while simultaneously calculate the mean intensity field J_ν at each of these locations (Tielens, 2005; Williams & Viti, 2013). Hence, it is simplified by introducing the photon escape probability β (e.g. van der Tak et al. 2007 and references therein), which generalises J_ν to $J_\nu = S_\nu(1-\beta)$. For a photon emitted at a certain region in the cloud, β is the probability the photon will escape the cloud from that region (Tielens, 2005; Williams & Viti, 2013). The escape probability can be modified for basic geometrical shapes of the medium (e.g. see van der Tak et al. 2007 and references therein), that's why it is often the case that a geometry of a medium also needs to be defined as an input to a model solving the radiative transfer equations in non-LTE. The escape probability of a spherical cloud is defined below.

$$\beta = \frac{1.5}{\tau_\nu}\left[1 - \frac{2}{\tau_\nu^2} + \left(\frac{2}{\tau_\nu} + \frac{2}{\tau_\nu^2}\right)\exp(-\tau_\nu)\right] \tag{1.21}$$

From this, the level populations can finally be estimated. With inputs of T_{k} and N_{col} the optical depth can be estimated below (van der Tak et al., 2007).

$$\tau_\nu = \frac{c^3}{8\pi\nu^3}\frac{A_{ji}N_{\rm col}}{1.64\Delta V}\left[x_i\frac{g_j}{g_i} - x_j\right] \tag{1.22}$$

Where x are the fractional population levels of i and j. Using τ_ν, the Eq. 1.7 can be solved, and the model's output is line intensities of the emitting molecule given a medium of a certain geometry, $T_{\rm k}$ and $N_{\rm col}$ and collisional rate set by the user. If a range of $T_{\rm k}$ and $N_{\rm col}$ and collisional rates are used, then the line intensities generated by the model can be compared to the observed line intensities to find the most appropriate physical parameters which can explain the observed line intensities. This is done through a goodness of fit statistical analysis test which will be described in the following Section.

1.3.3 Introduction to χ^2 Analysis

It is often the case in astronomy, that one wishes to describe the trend of some observations through use of a mathematical function - i.e. a model. But how would one robustly determine if the model and observations are in good agreement with each other? Astronomers turn to the goodness of fit chi-square (χ^2) test which is a statistical formula that computes the agreement between a model and observations. The value of the resulting output, known as the statistic, gives an indication of how well or how badly the model describes the trend of the observations. The lower the statistic of χ^2 is, the better the model fits the observations (e.g. Taylor 1996; Press et al. 1999). The formula for the χ^2 goodness-of-fit test in this instance is given below.

$$\chi^2 = \sum_{i=1}^{N}\left(\frac{O_i - M_i}{\sigma_i}\right)^2 \tag{1.23}$$

Where M_i represents the i^{th} data point of the model and O_i represents the corresponding observed data point. σ_i is the uncertainty of the observed data at the i^{th} data point.

Often, models contain a few physical parameters where their values are unknown. Therefore, multiple models, of quantity N_m, are generated with all varying parameters in order to obtain a good agreement between the model and observations. The χ^2 goodness of fit test can be applied to each of the models, provided the distribution of models and parameters follow a normal distribution. The formula changes to Eq. 1.24 (e.g. Taylor 1996; Press et al. 1999) below where y_i are our observable values at a given i^{th} value, and $f(x_i)$ is the corresponding i^{th} value of the model that is generated to fit or describe the trend of y_i by varying parameters. The χ^2 test evaluates the goodness of fit across number of observations N_o where there are corresponding points in the model, and then sums these values.

$$\chi^2 = \sum_{i=1}^{N_o} \left(\frac{y_i - f(x_i)}{\sigma_{yi}} \right)^2 \tag{1.24}$$

This creates a range of χ^2 values of quantity M_p. The parameters, and therefore model that has the closest agreement to the observations has the lowest (or minimum) χ^2 statistic ($\chi^2_{\rm min}$). A benchmark as to what a reasonable minimum chi-squared value should be, which gives good agreement between the model and the observables is given by $\chi^2_{\rm min} \sim N_o - \nu_p$. Where N_o is the number of observations and ν_p is the number of varying parameters of the model. This $N_o - \nu_p$ is given its own term, the degrees of freedom (Taylor, 1996; Press et al., 1999). The degrees of freedom, d_f, are particularly useful in determining the uncertainties of the χ^2 fit.

A χ^2 value of zero indicates a perfect fit to the observed data (e.g. Press et al. 1999). This rarely happens in nature as the observations have some random or systematic uncertainties associated with them. Therefore, there is always going to be an uncertainty associated with the best agreement between the model and the observations and so there are also uncertainties on the parameters used for the model. The way in which the uncertainties in the model and parameters can be quantified is through use of confidence regions. A confidence region is a region placed on the distribution of parameter values what have corresponding goodness of fit χ^2 values below a certain cut-off. This interval changes respectively to an area or a volume if two or three parameters are considered simultaneously. This can also be applied to finding the confidence intervals of the varying models too, which is shown in Fig. 2.3 in Sect. 2.2.3. The confidence interval is defined as $CI_{\rm lim} = \chi^2_{\rm min} + \Delta\chi^2$ (e.g. Avni 1976; Press et al. 1999).

This $\Delta\chi^2$ term sets the width of the interval in χ^2 space, and it depends on the probability density function (PDF) of the χ^2 distribution, the number of free parameters and the percentage interval to capture within the confidence interval. A typical PDF of a χ^2 distribution is shown in Fig. 1.4. Each value of χ^2 has an associated probability, and so a PDF is a representation of its distribution of probabilities across a range of χ^2 values. A χ^2 PDF is given by the formula below (e.g. Wasserman 2003).

$$f(x) = \frac{1}{\Gamma(d_f/2)2^{d_f/2}} x^{(d_f/2)-1} \exp\left(\frac{-x}{2}\right) \tag{1.25}$$

As mentioned before, the selection of $\Delta\chi^2$ depends on the number of varying parameters (e.g. Avni 1976; Press et al. 1999). These are called 'interesting' or 'free' parameters which I will denote ν_q. Table 1.1 shows the values of $\Delta\chi^2$ where one, two or three 'interesting parameters' are considered in calculating the distribution of goodness of fit χ^2 statistics.

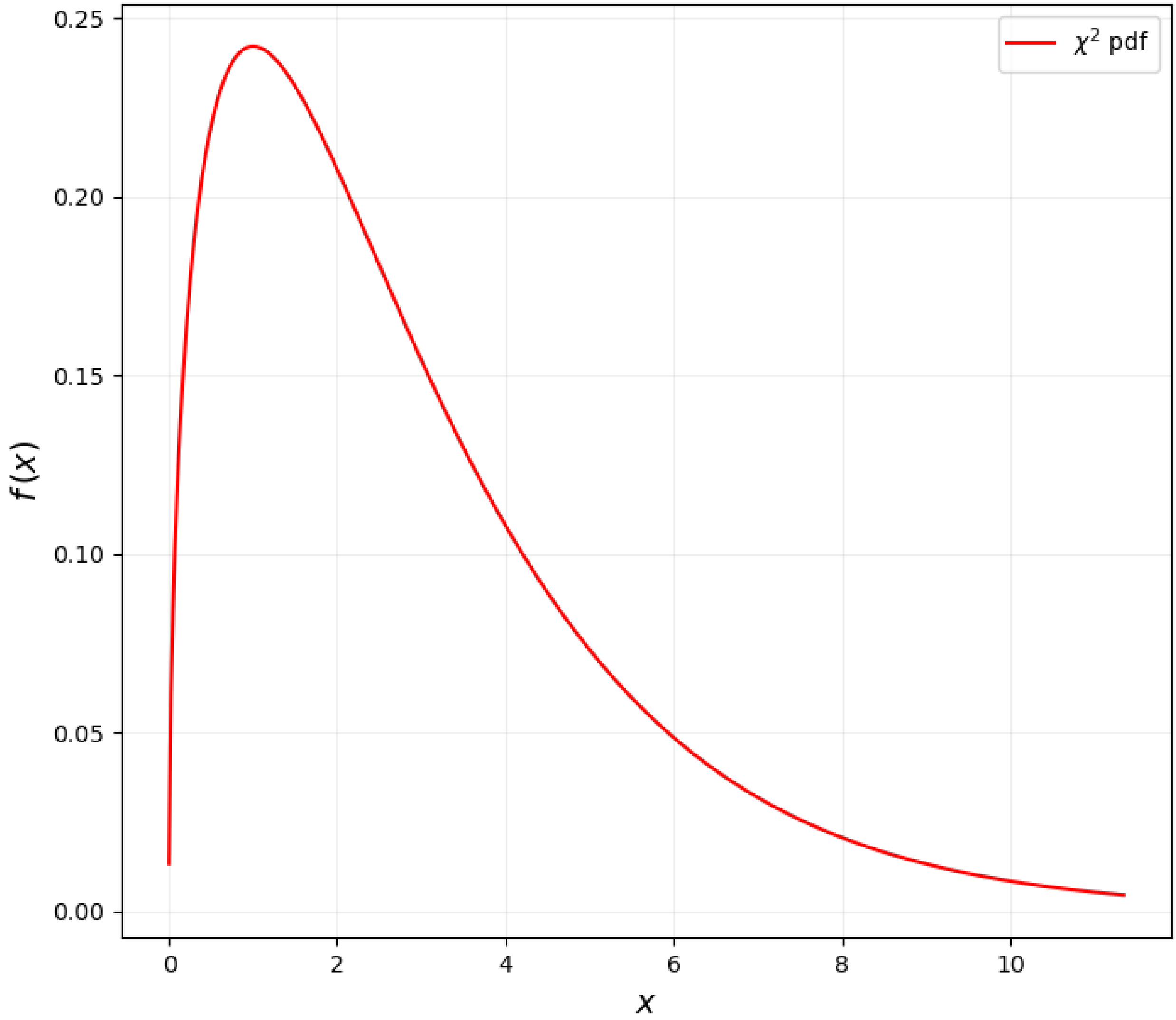

Figure 1.4. An example probability density function (PDF) of the χ^2 distribution with three degrees of freedom.

ν_q	68.3%	95.4%	99.7%
1	1.00	4.00	9.00
2	2.30	6.17	11.8
3	3.53	8.02	14.2

Table 1.1. Table displaying the $\Delta\chi^2$ values to create confidence intervals that encapsulates 68.4, 95.4 and 99.7% of the distribution of χ^2 statistics where one, two or three interesting parameters, ν_q are varied in the distributions (Avni, 1976; Press et al., 1999).

It is conventional to choose confidence intervals which contain 68.3, 95.4 and 99.7 % of the set of χ^2 values within the interval. These interval percentages correspond to 1, 2 and 3 times the standard deviation, σ, of normally-distributed data (e.g. Taylor 1996; Press et al. 1999). These conventions are also acceptable to use for the χ^2 distribution since, the underlying assumption for the χ^2 test is that the observations, models and parameters are normally-distributed. This is advantageous to astronomers as the confidence intervals can therefore lead to find the uncertainties in the best-fitting model and parameter fits by imposing the confidence interval on the distribution of models and parameters. This is can be realised because the confidence interval in χ^2 space can project onto the model and parameter distributions (e.g. Press et al. 1999). Therefore, if one imposes a confidence interval which encapsulates a certain percentage of the model and parameter distributions which corresponds to a certain σ-level of these distributions, one can find the minimum and maximum model and parameter values which have χ^2 values less than or equal to $\leq CI_{\mathrm{lim}}$ which can then be used to find the limits of the uncertainties of the best-fitting model to the observations. The χ^2 goodness of fit test is applied in Sect. 2.2.3 to find the best-fitting modified blackbody model to a set of thermal dust observations. I also use the concept of confidence intervals to find the uncertainties associated with the best-fitting model and best-fitting parameters.

1.4 Thesis Outline

The aims of this master's thesis are to provide a detailed description on how I analysed ALMA observations of the emission of HCO$^+$ in the ejecta of SN 1987A. I describe how I can compare spatial distributions of HCO$^+$ emission and to other molecular and atomic emissions such as CO and Hα. I also show how I can derive the mass of HCO$^+$ from the observations. I aim to answer the question of how HCO$^+$ was able to form in such quantities in the ejecta by looking at its chemical formation routes, and processes which occur within the ejecta to enhance the HCO$^+$ formation. The observations and analysis are beneficial to further our understanding of the molecular chemistry of supernova remnants.

The remainder of this master's thesis is structured in two chapters as follows. In chapter 2, I describe details the analysis of the HCO$^+$ data, how the HCO$^+$ emission was observed and the methodology into converting these observations into science-ready images. I compare the spatial distribution of HCO$^+$ to previously existing CO and SiO distributions and extract the line emission of HCO$^+$ to calculate the temperature and mass of HCO$^+$.

In chapter 3, I discuss the meaning of my results and investigate how HCO$^+$ may form in the ejecta of SN 1987A. This was done by estimating how much HCO$^+$ can react with CO as the key reactant to its formation and also using my results to predict what types of hydrodynamic mixing may occur in the ejecta. I also discuss how this research can be continued in future work. I finish this thesis with a summary of conclusions.

Chapter 2

HCO$^+$ in SN 1987A

"I know my value, anyone else's opinion doesn't really matter."

Peggy Carter *Agent Carter, 2015, season 1, episode 8.*

2.1 Observations and Analysis

2.1.1 HCO$^+$ Observations

HCO$^+$ Line	C	Baseline [m]	ν [GHz]	PWV [mm]	Angular Resolution [$''$]	N$_{\mathrm{ant}}$	Obs Start	Obs End	SN Days, d$_{SN}$
$J = 3 - 2$	C40–8	21.0–3696.9	267.56	0.3	0.08	38	2017-09-05	2017-09-05	11,153
$J = 3 - 2$	C43–8	92.1–8547.6	267.56	0.3–0.7	0.03	47–49	2017-11-21	2017-11-23	11,229–11,231
$J = 3 - 2$	C43–4	15.1–1261.4	267.56	0.9–1.5	0.22	43–44	2018-09-10	2018-09-14	11,522–11,526
$J = 3 - 2$	C43–8	92.1–8547.6	267.56	0.5	0.03	44	2019-07-21	2019-07-21	11,837
$J = 3 - 2$	C43–8	92.1–8547.6	267.56	0.4	0.03	45	2019-07-28	2019-07-28	11,844
$J = 4 - 3$	C43–5	15.1–1713.8	356.73	0.6	0.12	48	20-10-2018	20-10-2018	11,562
$J = 4 - 3$	C43–3	15.1–783.5	356.73	0.9	0.27	49	31-08-2018	31-08-2018	11,512

Table 2.1.1. The HCO$^+$ observations analysed in this work. C is the configuration name of the ALMA antennas, the configuration of antennas affects the maximum and minimum baseline length between antennas and therefore the angular resolution and minimum recoverable scale of the observations. ν shows the transition frequencies of HCO$^+$ in the rest frame, PWV quotes the range of precipitable water vapour at the time of observation, N$_{\mathrm{ant}}$ is the minimum and maximum number of antennae used. The final three columns state the start and end dates of the observations, and time in days since the initial supernovae explosion.

$J = 3-2$ HCO$^+$ Observations

ALMA observations of the spatially resolved line emission from the $J = 3-2$ HCO$^+$ transition at 267.56 GHz is used in this work (available under project number 2016.1.00077.S in the ALMA archive), which was collected using ALMA's band 6 recievers. Observations spanned from the 5th of September 2017 to the 28th of July 2019 (SN days 11,153 and 11,843) in ALMA observation Cycles 4 to 6. Observations are also summarised in Table 2.1.1. The observations used the ALMA antenna array configurations C40−8, C43−8 and C43−4. The former two configurations have a more extended array configuration where the maximum baselines between antennas range between 21.0−3,700 m and 92.1−8,500 m and had a total integration time of ∼5 hours. The C43−4 configuration is more compact with its antenna baselines ranging between 15.1−1,200 m, this configuration had an integration time of ∼2.5 hours. The extents of the two configurations comes with the advantage that the more extended array can probe emission from smaller scales whereas the more compact array can image larger areas of the ejecta (Cortes et al., 2024). Precipitate water vapour levels during the observation days for all configurations were found to be in an acceptable range to proceed with analysis of the data; with maximum values being 0.7 and 1.5 mm for the extended and more compact configurations respectively. The observations spanned across two 'spectral windows' which, when combined, has a frequency range of 265.6 to 269.2 GHz, corresponding to a velocity range of -1840 to 2190 km s^{-1}. The HCO$^+$ line emission is Doppler-broadened to a full-width at half maximum (FWHM) of 2,000 km s^{-1} (Matsuura et al., 2017) due to the expanding ejecta, hence, two spectral windows are needed to capture the majority of the HCO$^+$ line emission. The $J = 3-2$ HCO$^+$ data also has a non-zero continuum level present in the emission, the impact the continuum has on the spatial distribution of the $J = 3-2$ HCO$^+$ emission is investigated in Sect. 2.2.2 and the continuum level is estimated and subtracted from the HCO$^+$ line emission in Sect. 2.3.

The antennas at the ALMA observatory measure the HCO$^+$ emission as a visibility amplitude (or called the antenna temperature as in Sect. 1.3.1) which has units of Kelvin. This is converted to a flux density (in W m^{-2} Hz^{-1}) by calibrating it to a quasi-stellar object of known flux and brightness temperature (e.g. Cortes et al. 2024) which was done using the ALMA pipeline. The bandpass and phase of each antenna also need to be calibrated using quasars. Hence, J0519−4546 was used to calibrate the flux scale, J0635−7516 and J0522−3627 were used for the bandpass calibration and J0601−7036 and J0529−7245 were used to calibrate the phase. It is standard that this calibration introduces an uncertainty in the flux of about 7% for band 6 observations (ALMA Partnership et al., 2017). After calibration, the observations were de-convolved using the Common Astronomy Software Application's (hereafter CASA (CASA Team et al., 2022)) TCLEAN function*. This allows images of the observations to be reconstructed from a set of visibilities by performing an inverse Fourier transform on them (Cortes et al., 2024). All of the $J = 3 - 2$ HCO$^+$ observations in Table 2.1.1 were combined during this stage to form 1 image. TCLEAN was executed with the 'Briggs' weighting option which acts as a variable slider between having de-convolved images having a uniform or a natural weighting applied to the synthesised or 'dirty' beam. The natural weighting function reduces the noise in the images but also decreases the resolution. A uniform weighting increases the resolution of the image but also increases the noise. The Briggs function is set between variables 2.0 and -2.0 which correspond to almost natural and almost uniform weightings respectively. I set the robust value of the weighting to be 0.5, which favours a slightly more natural weighting, which keeps some small scale structures present in the $J = 3 - 2$ HCO$^+$ images whilst also ensuring a reasonable signal-to-noise ratio is achieved. This set-up in TCLEAN results in a full-width at half maximum (FWHM) beam size of 0.085$''$×0.072$''$ with a beam position angle of 44.312°. RMS noise in the resulting images was calculated through the placement of an off-source aperture in ALMA's own image analysis software CARTA (Comrie et al., 2021).

The $J = 3 - 2$ HCO$^+$ observations spanned across ~2 years, during which the ejecta may have undergone significant changes. Therefore checks must be done to ensure that they have little effect on the HCO$^+$ intensities. The expansion of the remnant can change the angular scale of the HCO$^+$ emission, our first check is to calculate by how much this angular scale changes. If molecules are doppler-broadened to velocities of $\pm$2,000 km s^{-1} (Matsuura et al., 2017) is assumed, then the angular expansion of HCO$^+$ increases by $\leq$0.02$''$ between the start and end dates of the observations. Therefore the expansion of the ejecta has a negligible impact on the HCO$^+$ observations since the change in angular expansion is smaller than the FWHM beam size (0.085$''$×0.072$''$) of the HCO$^+$ images. Changes in the heating source which powers the HCO$^+$ emission would also affect its intensity and therefore needs to be checked. Assuming HCO$^+$ is powered by the decay of ^{44}Ti which powers other molecular, ionic and dust emission in the central regions of the ejecta (e.g. Matsuura et al. 2011, 2015; Jones et al. 2023) results in a heating decrease of 2.2 % between the start and end observation dates. This is assuming that the decay rate of ^{44}Ti, which has a half-life of 58.9 years (Ahmad et al., 2006), is proportional to the decrease in the heating which powers the HCO$^+$ emission. Another source of heating which could power the HCO$^+$ emission is from the energy deposition of X-rays from shock interactions in the ring. The ring's X-ray flux has decreased by ~3.8 % during the HCO$^+$ observation period (Ravi et al., 2024). Hence, from these checks, only very minimal changes to the HCO$^+$ intensity have occurred across the time period of observations.

---

*`https://casadocs.readthedocs.io/en/stable/api/tt/casatasks.imaging.tclean.html`

$J = 4 - 3$ HCO$^+$ Observations

To determine physical properties of the HCO$^+$ emission such as its mass and temperature, an additional HCO$^+$ transition is also needed. Therefore we also observe the $J = 4 - 3$ HCO$^+$ transition at 356.73 GHz (project code 2017.1.0221.S in the ALMA archive). Emission from the $J = 4 - 3$ HCO$^+$ transition was collected using ALMA's band 7 receivers. ALMA antennas were arranged in the C43−3 and C43−5 configurations which had antenna baselines ranging from 15 to 1700 m. The data was collected on the 31st of August 2018 and the 20th of October 2018 (SN days 11,513 and 11,562 respectively) with an integration time of ∼1.2 hours. The calibration of the flux, bandpass and phase was done using the quasar J0529−7245. Precipitable water vapour levels on the days of observation measured at the observatory was in an acceptable range with a maximum being at 0.9 mm. This information is also summarised in Table 2.1.1.

The $J = 4 - 3$ transition data-cube has a FWHM beam size of 0.340″×0.265″ with a beam position angle of -10.724°. This angular resolution is sufficient to resolve ejecta from the ring, however, unable to resolve within the ejecta with an example of this seen in Figure A.1 in the appendix. Two spectral windows were used to observe the $J = 4 - 3$ transition, which span across 354.8−358.00 GHz (or, −1350 to 1650 km s^{-1} with respect to the rest frequency of the $J = 4 - 3$ HCO$^+$ emission at 356.73 GHz) when combined. While it covers the most of the broadened emission, centred about its transition frequency, we believe it does miss the red-shifted tail of the $J = 4 - 3$ emission (between 1,650 to 1,800 km s^{-1}) if we assume it is broadened to FWHM velocity range of ∼2,000 km s^{-1}, which is the same broadening we assume for HCO$^+$ $J = 3 - 2$. Additionally, like the $J = 3 - 2$ HCO$^+$ emission, there is a non-zero contribution to the continuum present in this data which will be estimated and subtracted from the line emission in Sect. 2.3. Systematic uncertainties in the flux are assumed to be 7% for ALMA observing band 7 (ALMA Partnership et al., 2017). This was combined with the RMS uncertainties taken in an aperture placed off-source taken at each velocity channel from the data cube, which was the same for the $J = 3 - 2$ observations.

2.1.2 Archival Data

Archival observations of CO, SiO and Hα are acquired to infer additional properties of the HCO$^+$ data such as whether it requires CO to form or the ionisation levels of the HCO$^+$ gas.

CO and SiO Observations

Archival ALMA observations of the spatial distributions of emission of the CO $J = 2 - 1$ transition at 230.54 GHz and the SiO $J = 5 - 4$ transition at 217.10 GHz reported in Abellán et al. (2017) and Cigan et al. (2019) are acquired. These observations were made on days 10,054 and 10,479 since the supernova explosion, these observations were then combined to improve the S/N of the observations (Abellán et al., 2017). The resulting data cubes have a beam FWHM of 0.06″×0.04″ and beam position angles of 27.43° and 19.74° for CO and SiO respectively. For comparison with the HCO$^+$ distribution, these data cubes were re-convolved to the coarser HCO$^+$ beam size and angle. Since there is a time difference between the HCO$^+$ observations and the CO and SiO observations, the expansion of the ejecta may effect comparison between the two. I therefore calculate the change in the angular expansion between these two times. Using the same methodology in Sect. 2.1.1, the maximum predicted angular expansion is ∼0.04″ which is roughly half the FWHM width of the HCO$^+$ beam size, therefore showing the angular expansion between the two data sets is negligible and a comparison of their spatial distributions can be done.

Hα

As mentioned previously in Sect. 1.1.2, Hα is a good tracer of the energy deposition of X-rays from the ring onto the ejecta. I used observations of the Hα emission reported in Fransson et al. (2015) and Larsson et al. (2016). This emission was observed for 1,200s using the *Hubble Space Telescope* on day 9,973 after the SN explosion, this equates to the Julian date of June the 15th 2014. This emission was observed using the Wide Field Camera 3 (WFC3) with the F625W filter where the emission is predominantly from the recombination of Hα at this wavelength. This image was obtained already re-aligned to the centre of the ejecta by using the ring as a reference *(P. Cigan, Private communication)*. The angular scale of the individual pixels in the image is ≈ 0.025″.

Dust Continuum Observations at 315 GHz

I utilise observations of the dust emission that was observed at 315 GHz reported by Matsuura et al. (2024). These observations were made using the ALMA observatory on the 2nd of November 2021 ($\mathrm{d_{SN}}$=12,671). These images had a FWHM beam of 0.081″×0.068″ and a beam position angle of 33.66°. This image was re-convolved to the $J = 3 - 2$ HCO$^+$ beam size to aid with the comparison between the two images. Further information regarding this dust observation can be found at Matsuura et al. (2024).

2.2 Analysis of Observations

2.2.1 The Velocity Channel Map

The chemical reactions involved to form HCO^+ in the ejecta of SN 1987A are unknown. We speculate that HCO^+ could form from chemical reactions involving CO such as $H_3^+ + CO \rightarrow HCO^+ + H_2$ (e.g. Panessa et al. 2023). I discuss the likelihood that this reaction is also the same for HCO^+ formation in SN 1987A in Sect. 3.1.1. To investigate this further, I created spatially-resolved velocity channel maps of the $J = 3 - 2$ HCO^+ emission and compared it to the velocity channel maps of the CO $J = 2 - 1$ emission and compared their distributions. If HCO^+ requires CO to form, then their spatial distributions within the ejecta would coincide or at least be similar. As a control comparison, I also compare the spatial distribution of HCO^+ with that of the $J = 6 - 5$ transition of SiO, which I anticipated, is an unrelated molecule to the formation of HCO^+.

The HCO^+ observations are Doppler-broadened to roughly $\sim\pm 2{,}000\,\mathrm{km\,s^{-1}}$, arising from the expansion of the ejecta and thus enabling the plotting of the observations as a velocity channel map. The velocity channel map shows the morphology of the HCO^+ emission along the line of sight of the observer, split across the range of velocities that the emission is Doppler-broadened to. This proves advantageous in order to understand the morphology of the HCO^+ emission as this form of imaging enables the 'peering through' of the ejecta to have an understanding of the three-dimensional structure of HCO^+ emission, represented as a collection of 2-dimensional image slides I will call velocity channels. Figure 2.1 shows the velocity channel map for the $J = 3 - 2$ emission of HCO^+. This emission's velocities range from $-1{,}950$ to $1{,}650\,\mathrm{km\,s^{-1}}$, relative to the rest frequency of HCO^+ at 267.56 GHz (i.e $0\,\mathrm{km\,s^{-1}}$ corresponds to 267.56 GHz). This velocity range is binned in 12-velocity channel increments of $300\,\mathrm{km\,s^{-1}}$. This increment size was chosen to maximise the signal in each velocity bin whilst also retaining some of the velocity structure of the HCO^+ emission. The labels on each velocity channel correspond to the median velocity of each bin. The velocities have been corrected for the Kinematic Local Standard of Rest frame (LSRK) but have not been corrected for the systematic velocity of SN 1987A at $286.7\,\mathrm{km\,s^{-1}}$ (Gröningsson et al., 2008). Figure 2.1 shows that the HCO^+ and continuum emission only begins to appear above the noise in the $-1{,}200\,\mathrm{km\,s^{-1}}$ velocity channel, therefore I attribute slides -1800 and -1500 to be too noisy to analyse further. The HCO^+ emission peaks at 0 to 600 $\mathrm{km\,s^{-1}}$, it then fades in the channels 900 to $1{,}500\,\mathrm{km\,s^{-1}}$. From visual inspection, the emission is quite blobby. The brightest blobs in the channel map are found in the east and western regions of the ejecta from the -600 to $300\,\mathrm{km\,s^{-1}}$ velocity channels and the brightest of these blobs is found to the west in the $300\,\mathrm{km\,s^{-1}}$ channel. The fainter HCO^+ emission extends more towards the north and south regions, particularly in the channels from 600 to $1{,}200\,\mathrm{km\,s^{-1}}$. Overall, this

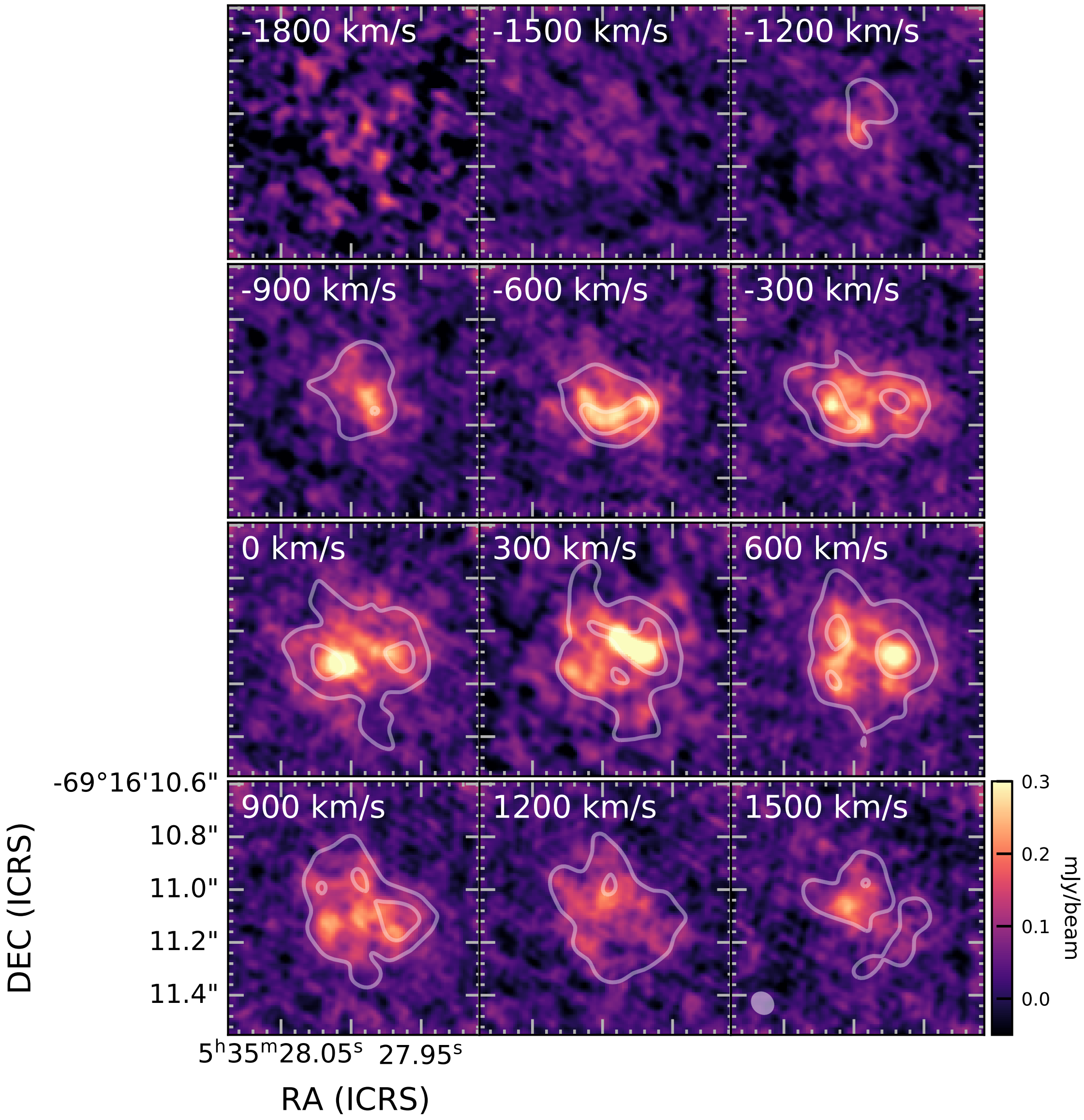

Figure 2.1. A velocity channel map of the morphology of the $J = 3 - 2$ HCO$^+$ emission which ranges from -1950 to 1650 km s^{-1} and is binned in 300 km s^{-1} increments. Each channel is labelled with the central velocity of 300 km s^{-1} binned channel. All velocities are in LSRK. The typical RMS noise in these images are ~2.5–4.3×10^{-2} mJy beam^{-1}. Continuum emission is also present in these HCO$^+$ images, this continuum level, if uniformly spread over the ejecta is roughly 0.02 mJy beam^{-1} - roughly the same level as the RMS. The distribution of the CO $J = 2 - 1$ emission is represented as the white contours superimposed atop the HCO$^+$ emission. Two CO contour levels of brightness levels of 0.5 and 1.20 mJy beam^{-1} were chosen to better display the CO emission in relation to the HCO$^+$ emission. From visual inspection of the CO and HCO$^+$ morphologies, the peaks of brightest emission overlap, particularly in velocity channels 0 km s^{-1} to 600 km s^{-1}, and that their overall shapes are similar across the velocity channels. All enclosed CO contours within the larger-overall CO contour are bright spots in the CO distribution, except for the small ellipse in the central-south region of the 300 km s^{-1} channel, where it is instead a region of lower CO intensity, see Cigan et al. (2019) for further information.

emission is quite compact (from Fig. 2.1, $\lesssim$0.6$''$ across) and located centrally in the ejecta.

2.2.2 Continuum Estimation in the $J = 3 - 2$ HCO$^+$ Image

As mentioned in Sect. 2.1.1, there are continuum levels present in the HCO$^+$ images. A convention of ALMA is that these continuum levels are usually estimated from line-free channels which are adjacent to the channels containing the HCO$^+$ line emission and subtracted from the image cubes during the cleaning process using CASA's UVCONTSUB before cleaning[†]. However, the broadness of the HCO$^+$ line ($\sim\pm$2,000 km s^{-1} (Matsuura et al., 2017)) meant there were no line-free adjacent channels to estimate the continuum and subtract it from the HCO$^+$ emission. Instead, I investigate the impact of the continuum on the spatial distribution of the $J = 3 - 2$ HCO$^+$ emission. Assuming that the continuum levels are caused by dust emission, I compare the spatial distributions of the continuum-included $J = 3 - 2$ HCO$^+$ emission with the dust emission at 315 GHz. This is seen in Fig. 2.2. The HCO$^+$ emission was integrated across the velocity range -1050 to 1650 km s^{-1} and is shown as the colour map in the figure. Contours of the dust emission are superimposed onto the HCO$^+$ emission with intensity levels of 7×10^{-5} and 9×10^{-5} Jy beam^{-1} which roughly correspond to the range of 3×RMS level found in each HCO$^+$ velocity channel ($\sim$7$-$10$\times10^{-5}$ mJy beam^{-1}). By comparing the two distributions, the peak of the dust emission in the south of the ejecta is located in a region of low HCO$^+$ emission. Additionally, the relative weakness of the dust emission to the HCO$^+$ emission in Fig. 2.1 indicates that the dust continuum has little impact on the spatial distribution of the $J = 3 - 2$ HCO$^+$ emission. Therefore, even with continuum being present within the $J = 3 - 2$ HCO$^+$ images, the bright spots of HCO$^+$ are attributed to being predominantly HCO$^+$ emission, making the comparisons of the bright spots of HCO$^+$ to bright spots of CO, SiO and Hα in the subsequent sections valid.

2.2.3 Estimating the Continuum Level

I estimate the HCO$^+$ line emission and infer physical properties such as the mass and temperature from the lines in Sect. 2.3 and 2.4. However, if the continuum levels remain present in the HCO$^+$ line emission, then I will overestimate my HCO$^+$ line emission, and therefore result in an inaccurate HCO$^+$ mass and temperature. I estimate these continuum levels and subtract them from the HCO$^+$ line emission in the following section. I cannot use the dust emission levels present in the 315 GHz image discussed in Sect. 2.2.2 to estimate the dust emission at my HCO$^+$ transitions of

---

[†] `https://casadocs.readthedocs.io/en/stable/api/tt/casatasks.manipulation.uvcontsub.html`

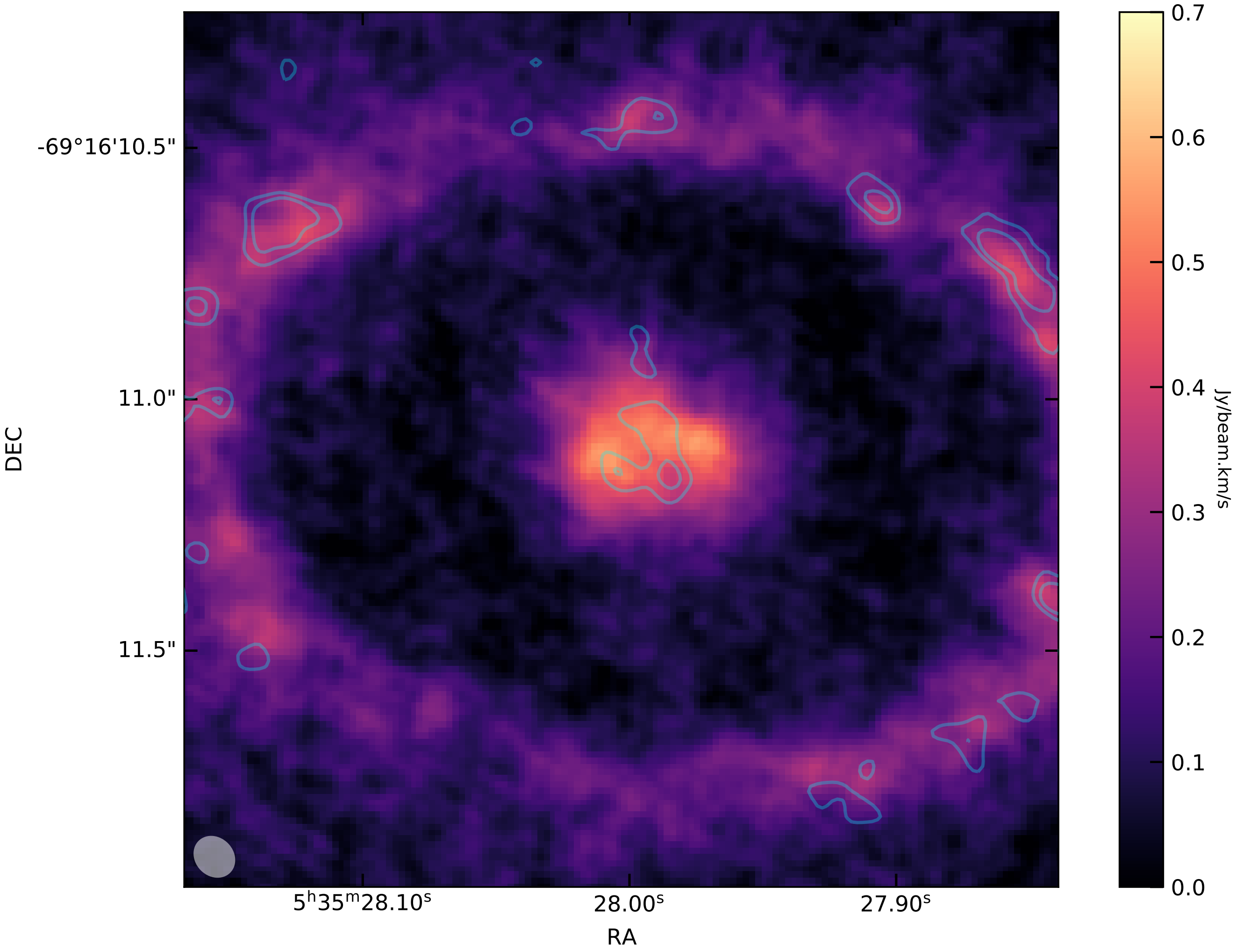

Figure 2.2. An image of the continuum-included $J = 3 - 2$ HCO$^+$ emission which has been integrated across the velocity range of -1,050 to 1,650 km s^{-1}. Emission from the equatorial ring is also present in this image. A contour of the dust emission at 315 GHz is superimposed on top where its contour levels correspond to $7{\times}10^{-5}$ and $9{\times}10^{-5}$ Jy beam. The 315 GHz dust image is originally from Matsuura et al. (2024) and has been smoothed to the coarser HCO$^+$ beam size of 0.085″×0.072″. The lower contour of $7{\times}10^{-5}$ corresponds to roughly the mean threshold value used in the analysis of the correlations in Sect. 2.2.6. The dust emission peaks in the south of the HCO$^+$ emission where the HCO$^+$ emission is quite low.

267 and 356 GHz as dust emission follows a modified blackbody trend and so varies significantly at these frequency ranges. Assuming that the continuum is mostly attributed to thermal dust emission, the continuum levels on HCO$^+$ were estimated via fitting a modified blackbody curve to thermal dust observations in the sub-mm and far-IR. We take the sub-mm observations from (Cigan et al., 2019) which were observed with ALMA Cycle 2. These observations span across days, $\mathrm{d_{SN}}$, 10,352 and 10,441 since the supernova explosion and range from 225.5 to 679.22 GHz which are predominantly in the Rayleigh-Jeans region of the modified blackbody spectrum. The far-IR observations were taken with the *Herschel Space Observatory* at $\mathrm{d_{SN}}$= 9,090 and 9,122 from (Matsuura et al., 2015) spanning 100 to 350 μm (or 3,000.0 to 857.14 GHz). The observations from the far-IR were included in the fit to constrain the peak of the modified blackbody, which constrains the temperature, T_d and $\kappa_{\rm abs}$ of the dust. Without the far-IR observations, our uncertainties in the fit parameters T_d and $\kappa_{\rm abs}$ would be very large and thus induce a large uncertainty in the continuum level fit.

A modified blackbody curve builds upon Planck's definition of a blackbody spectrum with the inclusion of effects from dust. A modified blackbody distibution S_ν, is characterised by dust emission is given by the following equation (e.g. Hildebrand 1983):

$$S_\nu = \frac{3M_d Q(\nu) B(\nu, T)}{4a\rho D^2} \tag{2.1}$$

Where M_d is the mass of the dust, $B(\nu, T)$ is the Planck function across frequency space, D is the distance to the source of the dust emission which in this case, is the distance to SN 1987A. $Q(\nu)$, a and ρ are all properties of the dust grains themselves, respectively the dust grain emissivity, radius and density (Hildebrand, 1983). These three terms are collected up into the dust mass absorption coefficient, called κ_{abs} (e.g. Whittet 1992) defined by:

$$\kappa_{abs} = \frac{3}{4}\frac{Q(\nu)}{a\rho} \tag{2.2}$$

Thus leading to a simplified form of Equation 2.1, by substituting in Equation 2.2.

$$S_\nu = \frac{M_d \kappa_{abs} B(\nu, T)}{D^2} \tag{2.3}$$

κ_{abs} is often estimated using an empirical power-law (Hildebrand, 1983).

$$\kappa_{abs} = \kappa_0 \frac{\lambda}{\lambda_0}^{-\beta} \tag{2.4}$$

Where κ_0 is the empirical value of the mass absorption coefficient at some reference wavelength,

λ_0. For the local ISM, κ_0 is 0.07 m^{2}kg^{-1} at $\lambda_0 = 850\mu$m (James et al., 2002). The empirical relationship in Eq. 2.4 is used to estimate the $\kappa_{\rm abs}$ for my modified blackbody fit.

The values of β, T_d and M_d that best fit the trend of thermal dust observations are unknown. Therefore, a more robust statistical analysis is required to fit the modified blackbody to calculate its continuum levels and its uncertainties. For this, a Monte-Carlo simulation (MC) in combination with the χ^2 goodness-of-fit test are used. The process to obtain the best fitting parameters of β, T_d and M_d and therefore the best-fitting modified blackbody curve to the thermal dust emission are described as follows. Firstly, 5,000 sets of randomly-generated thermal dust emission fluxes are made, which I will call the *simulated* thermal dust emission, the distributions of the 5,000 sets follow a normal distribution where mean values are the values of the observed thermal dust emission and the standard deviation of the distribution of simulated data, $\sigma_{\rm SD}$, are equal to the uncertainties of the observed thermal dust emission. Uncertainties for the observed sub-mm thermal dust flux measurements include the RMS, calibration uncertainty of the flux and spectral leakage from the ER to the ejecta, which are also listed in Cigan et al. (2019). Uncertainties of the observed far-IR data arise from uncertainty in the flux and flux calibration, which are listed in Matsuura et al. (2015). There is an additional, systematic uncertainty of 50 $\%$ only on the positive side of the sub-mm thermal dust fluxes shown as the blue error bar in Figure 2.3. I do not use this uncertainty in the generation of the 5,000 sets of simulated thermal dust emission as this uncertainty has little effect on the variability of the MC modified blackbody fits which is ultimately more tightly constrained by the far-IR dust observations.

Each of the 5,000 sets of simulated thermal dust emission was fitted with a modified blackbody curve to obtain estimations of β, T_d and M_d. This was done using SCIPY's CURVE_FIT (Virtanen et al., 2020) which fitted a curve described by Eq. 2.3 to the simulated sets thermal dust emission via a non-linear least-squares fitting method[‡]. These MC simulated modified blackbody fits are seen in Figure 2.3. To find the best fitting MC modified blackbody, a χ^2 goodness of fit test was set up to evaluate the agreement between each simulated modified blackbody curve and the observed thermal dust fluxes, this generates a χ^2 statistic grading the fit for each simulated modified blackbody to the thermal dust observations and hence, I now have a distribution of χ^2 values. The minimum χ^2 value, denoted $\chi^2_{\rm min}$, indicates the best fitting model and parameters to the observations. The uncertainties in the best fitting modified blackbody curve and in the best fitting β, T_d and M_d were calculated by setting up a confidence interval in the distribution χ^2 values. This confidence interval is defined via $\chi^2_{\rm min} + \Delta\chi^2$ where $\Delta\chi^2$ =3.5 (e.g. Avni (1976); Press et al. (1999)), which encloses a 1σ width $\Delta\chi^2$ where three interesting parameters are varied (β, T_d and M_d) at the same time. The pink shaded region in Figure 2.3 shows the 1σ confidence interval on the modified blackbody fits to the thermal observations. The best fit and confidence

---

[‡] `https://docs.scipy.org/doc/scipy/reference/generated/scipy.optimize.curve_fit.html`

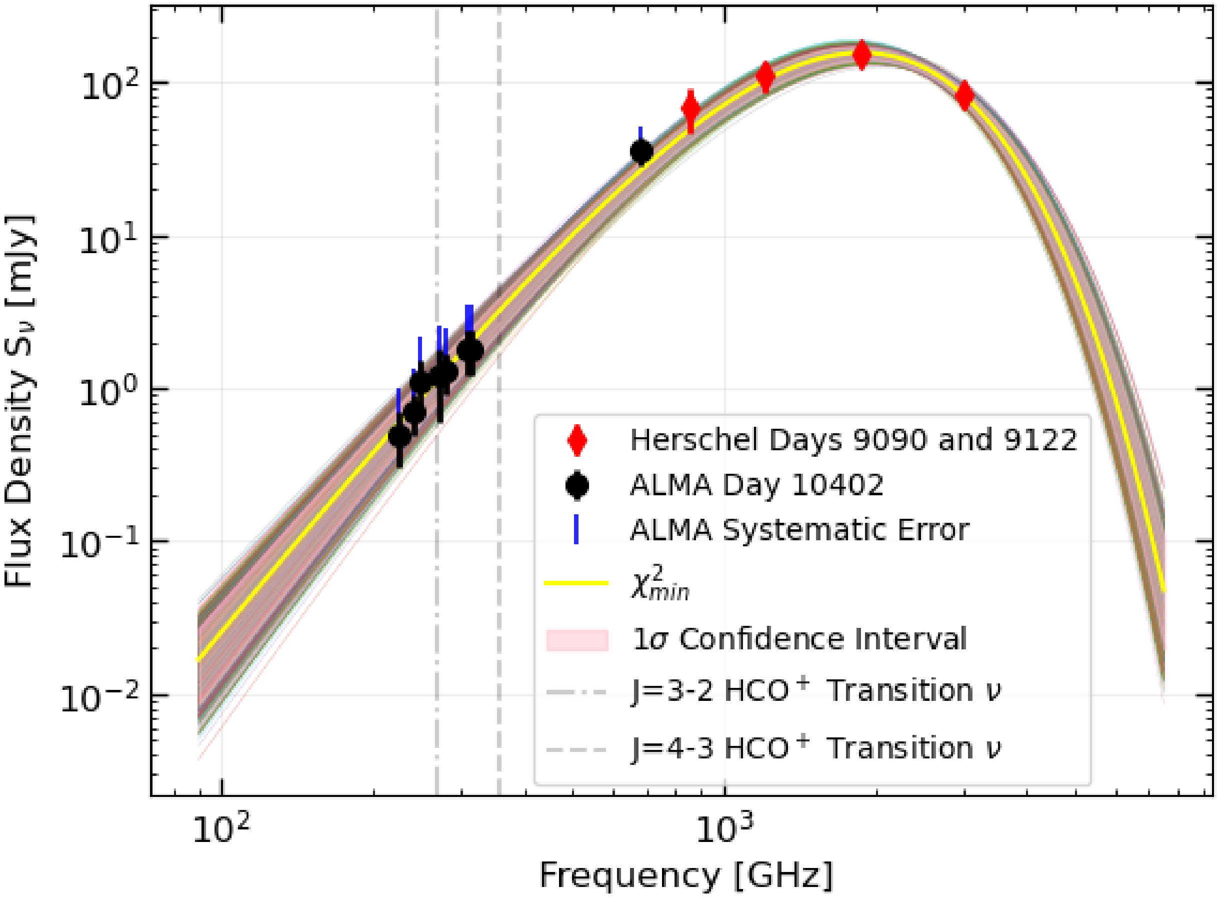

Figure 2.3. Modified blackbody fits to the thermal dust emission using a Monte-Carlo technique. Black circles denote the sub-mm ALMA thermal dust observations at day ~10402 and associated errors (Cigan et al., 2019). The blue error bars on the positive end of the observations denote the additional systematic 50% ALMA cycle 2 uncertainty which was not included in the MC analysis. The red diamonds denote the far-IR Herschel thermal dust observations to constrain the peak of the modified blackbody (Matsuura et al., 2015). The yellow line indicates the best fit for the continuum level. The pink interval indicates the 1σ uncertainty of the varying β, T_d and M_d as a result from perturbing the thermal dust data. The grey dot-dashed and dashed lines indicate the central transition frequencies of the $J = 3-2$ and $J = 4-3$ HCO$^+$ transitions respectively which have been corrected for the heliocentric velocity of SN 1987A at -287 km s^{-1}. (Gröningsson et al., 2008).

interval analysis returned parameter values of β=2.1$^{+0.3}_{-0.3}$, T=17.8$^{+1.6}_{-1.4}$ K and M_d=1.4$^{+0.3}_{-0.3}$ M$_\odot$. Using the best fitting modified blackbody curve and uncertainties, the continuum fluxes at the two HCO$^+$ frequency ranges (of corresponding velocity ranges of -1050 to 1650 km s^{-1} for the $J = 3 - 2$ HCO$^+$ transition and -1350 to 1650 km s^{-1} for the $J = 4 - 3$ HCO$^+$ transition) are integrated across these frequency ranges giving continuum levels of (2.69±0.29) $\times$10^{-29} W m^{-2} and (1.02±0.92) $\times$10^{-29} W m^{-2}. The uncertainties of the continuum level estimations originate from the minimum and maximum continuum values of the simulated MC fits within the χ^2 confidence interval.

A pit-fall to this analysis stems from the *Herschel* thermal dust observations, which were taken $\sim$7 years before our HCO$^+$ observations. Due to the evolution of the remnant and its on-going cooling, the *Herschel* dust fluxes and therefore the peak of the modified blackbody is expected to be lower if the *Herschel* observations were taken at the same time as our HCO$^+$ observations. I investigate how much this affects the continuum levels at the HCO$^+$ transition frequencies. This decrease in the peak can be quantified from following the calculations set out by Cigan et al. (2019) and assuming that the heating of the dust, powered by the radioactive decay of ^{44}Ti (e.g. Matsuura et al. 2011), is proportional to the decrease in luminosity of the modified blackbody. The decrease in decay energy from the radioactive decay of ^{44}Ti, which has a half life of 58.9 years (Ahmad et al., 2006), is calculated from the *Herschel* observations to the end of the HCO$^+$ observations at d$_{\mathrm{SN}}$= 11,844 days, which would decrease by $\sim$9 %. Then through using the Stefan-Boltzmann law, $L \propto T^4$, this results in the temperature decrease of the modified blackbody initially at 20 K to decrease to 19.54 K across the $\sim$7 year time difference. This results in a continuum level decrease in the modified blackbody curve at the HCO$^+$ transition frequency ranges centred at $\sim$267 and $\sim$356 GHz of 3.1$-$3.4 %. Therefore, the time-difference between the *Herschel* and the HCO$^+$ observations has a negligible impact on the continuum level estimations as this change in continuum level is within our uncertainties of the MC fits to the thermal dust emission.

2.2.4 HCO$^+$ Comparison with CO

Figure 2.1 shows line contours of the $J = 2 - 1$ CO emission superimposed atop the colour-map images of the $J = 3 - 2$ HCO$^+$ emission at their corresponding velocity bin increments so that I may visually compare the spatial distributions of both. To best represent the comparison between the CO and HCO$^+$ emission, a two-level contour of the CO emission was chosen. The CO level contours correspond to 0.5 and 1.2 mJy beam^{-1} which indicate the extended low-brightness and bright-spot emission of CO respectively. The line emission of CO is roughly 6.3 times brighter than that of HCO$^+$. The spatial distributions of the HCO$^+$ and CO emission are quite similar, particularly for the brightest CO and $\mathrm{HCO^+}$ channels at 600 to 900 $\mathrm{km\,s^{-1}}$. Bright spots of CO coincide with the bright spots of $\mathrm{HCO^+}$ from channels -300 to 600 $\mathrm{km\,s^{-1}}$. A discrepancy arises when one compares the fainter, more extended emission of CO with that of $\mathrm{HCO^+}$, where the CO emission in channels 0 to 600 $\mathrm{km\,s^{-1}}$ extends further in the north-south direction. This is attributed to the better sensitivity of the CO image, which means more of the extended CO emission was captured in the image.

2.2.5 $\mathrm{HCO^+}$ Comparison with SiO

Figure 2.4 shows line contours of the $J = 5 - 4$ SiO emission superimposed on the colour-map channels of $J = 3 - 2$ $\mathrm{HCO^+}$ emission at their respective velocity increments. Visual inspection of the two molecular morphologies show that there are fewer similarities than the comparison made with $\mathrm{HCO^+}$ and CO. There is an overlap of bright spots in the velocity channel of 300 $\mathrm{km\,s^{-1}}$, and two partial bright spots overlap in the velocity channels of -600 $\mathrm{km\,s^{-1}}$ and 0 $\mathrm{km\,s^{-1}}$. The weaker emission of SiO extends to the south in velocity channels 0 and 300 $\mathrm{km\,s^{-1}}$ and then extends north in the velocity channels 600 to 1200 $\mathrm{km\,s^{-1}}$ whereas the $\mathrm{HCO^+}$ extended emission is more concentrated to the centre of the ejecta. Again, the discrepancy between the extended emission is attributed to the better sensitivity of the SiO images.

2.2.6 Correlations

The similarities between the spatial distributions of CO and $\mathrm{HCO^+}$ were investigated further by testing the strength of the correlation between their emissions. I also tested the correlation strength between $\mathrm{HCO^+}$ and SiO as a control. This was done by creating a Spearman rank correlation which is defined as a simplified equation below (e.g. Press et al. 1999).

$$\rho_s = 1 - \frac{\sum_{i=1}^{N} \Big(R(\mathrm{CO}_i) - R(\mathrm{HCO^+}_i) \Big)^2}{N(N^2 - 1)} \tag{2.5}$$

Where ρ_s is the correlation strength, $R(\mathrm{CO}_i)$ is the ith ranked CO brightness, $R(\mathrm{HCO^+}_i)$ is the ith ranked $\mathrm{HCO^+}$ brightness and N is the number of data point pairs of the CO and $\mathrm{HCO^+}$ brightness values. The 'rank' term means that the brightness values are sorted into pairs of CO and $\mathrm{HCO^+}$ brightnesses which are at the same spatial location in the images. This type of correllation was preferred over the Pearson rank correlation as it can test the correlation of monotonic data as well as data that shows a linear relationship. A way to implement a Spearman

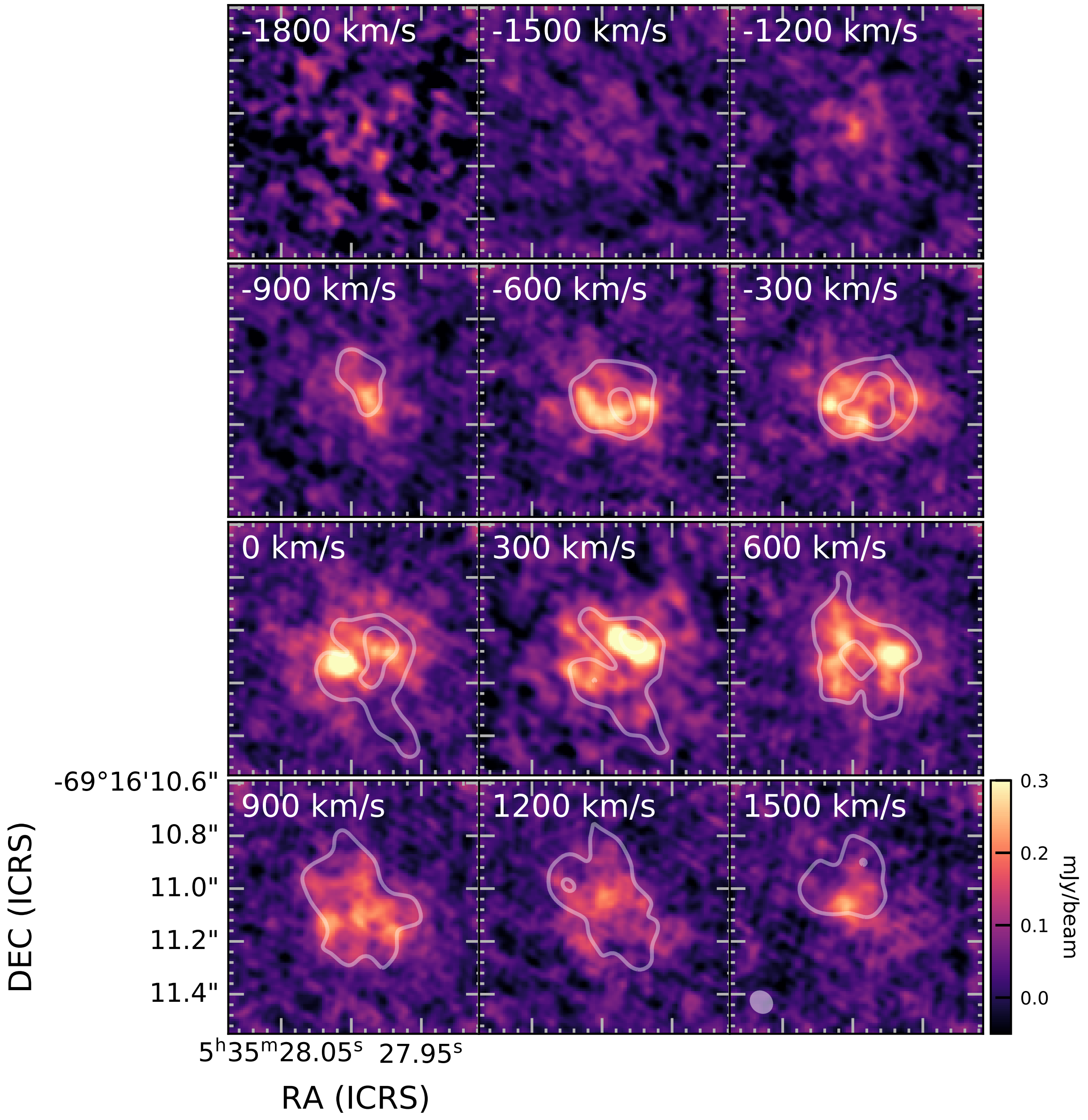

Figure 2.4. A velocity channel map displaying the morphology of the $J = 3 - 2$ HCO$^+$ emission with the $J = 5 - 4$ SiO emission superimposed as the white contour on top. This velocity channel set up is the same as in Fig. 2.1. The SiO contour levels have brightness levels of 0.5 and 1.20 mJy beam^{-1} which are the same as the CO intensity levels in Fig. 2.1. A visual inspection of the SiO and HCO$^+$ morphologies shows more differences between SiO and HCO$^+$ compared to CO and HCO$^+$ in Figure 2.1. There is however, overlap between bright spots of HCO$^+$ and SiO in the velocity channel 300 km s^{-1} with partial overlap in channels -600 and 0 km s^{-1}. The enclosed SiO contours within the larger contours are bright spots of SiO emission, except for a large ellipse in the centre of the SiO emission in the 600 km s^{-1} channel, where it is a 'hole' instead. See Cigan et al. (2019) for more details.

rank correlation is to compare the pixel-to-pixel brightnesses of HCO^+ and CO. For this, the pixels in each channel map are smoothed to the same beam and the pixels have the same scale (i.e. have identical areas in arcseconds, or project the same area in WCS coordinates). This was done by firstly convolving the CO and SiO images to match the coarser HCO^+ beam size using CASA's IMSMOOTH function. To prevent the data from being over-sampled, the pixel scale of each of the HCO^+, CO and SiO images was Nyquist sampled (e.g. Rieke 2012), hence the pixel sizes are roughly half of the FWHM of the beam, which was done using CASA'S IMREBIN function which helps to conserve flux when converting the pixel scale to a coarser grid. This leads to a pixel scale of $0.036'' \times 0.036''$. Figure 2.5 shows Nyquist-sampled HCO^+ pixel brightnesses versus CO pixel brightnesses. A clear monotonic relationship is seen in the velocity channels -600 to $600\,\mathrm{km\,s^{-1}}$ where brightnesses of HCO^+ and CO are the highest. Hence, the Spearman rank correlation strength was measured across the brightest velocity channels, ranging from -600 to $600\,\mathrm{km\,s^{-1}}$ and calculated through use of STATS.SPEARMANR which is a function of the SCIPY statistics module[§]. A correlation strength between HCO^+ and CO emission was calculated to be 0.72 thus indicating a moderately strong, positive correlation. Low-level signal was omitted from each channel using a threshold of 3×RMS of that channel (ranging from $\sim$7.5 to $10.5\times10^{-5}\,\mathrm{Jy\,beam^{-1}}$), this was done to limit the effect of the continuum and background intensities on the correlations.

This will not impact the correlations too greatly however, as the similarities between HCO^+ and CO are found between the bright spots of their emissions. There may still be a contribution of continuum in the correlation analysis. I argue however, that this has little impact on the correlations. I investigate this further by scaling the continuum level at the frequency range of the $J = 3-2$ HCO^+ emission found in Sect. 2.2.3 by the beam in image of the $J = 3-2$ HCO^+ emission in Fig. 2.1. This gives a value of $0.02\,\mathrm{mJy\,beam^{-1}}$ if the continuum emission was uniformly spread across the ejecta. Since this is $\sim$4 times smaller than the RMS threshold for the correlations, low brightness levels of continuum will not affect the correlations. It was found by Cigan et al. (2019) that the thermal dust emission is also uncorrelated with the $J = 2-1$ CO emission. From the 315 GHz dust emission in Fig. 2.2, one can see that the dust emission is not uniformly spread across the ejecta, it is distributed in clumps. However, the brightest clump of dust emission peaks in a region of low HCO^+ emission, therefore will also not affect the correlation analysis. The same Spearman rank correlation calculation was applied between the HCO^+ and SiO pixel brightnesses, a plot of this is seen in Fig. A.2 in the appendix. The Spearman rank correlation calculation of HCO^+ vs SiO returned a correlation strength of 0.65. Despite this correlation being weaker compared to the HCO^+ and CO correlation, it still indicates a moderately strong correlation. This could be due to the Spearman correlation showing a strong correlation for the

---

[§] `https://docs.scipy.org/doc/scipy/reference/generated/scipy.stats.spearmanr.html` ejecta itself instead of the small-scale structures of the molecules within the ejecta. Despite this, from visual inspection of the Figures 2.1 and 2.4, the HCO^+ spatial distribution more closely follows that of CO's thus showing they are somewhat co-spatial.

2.2.7 Comparison with Hα

Despite the gas in which we find HCO^+ being predominantly molecular, HCO^+ is a molecular ion which requires some degree of ionisation to occur for it to form. To give an indication of how ionised the HCO^+ gas is, I can compare the morphology of the HCO^+ emission to that of Hα. As discussed in the introduction, the dominant source of ionisation in the ejecta is energy deposition of X-rays from the ring which is traced by the Hα emission in the ejecta (e.g. Larsson et al. 2011, 2013, 2016). A comparison between the $J = 3 - 2$ HCO^+ and Hα distributions can help to infer details on the ionisation levels of the HCO^+ gas. This comparison is shown in Figure 2.6. This shows the *HST* WFC3 F625W band image which is dominated by Hα emission. Superimposed on the Hα is a two-level brightness contour of the $J = 3 - 2$ HCO^+ emission. The HCO^+ emission was collapsed along its velocity axis from -1,050 to 1,650 $\mathrm{km\,s^{-1}}$ to produce a zero moment image. A zero moment image of HCO^+ is more suitable for comparison with the Hα observation due to the Hα observation not being available as a channel map. The conversion of the HCO^+ data-cube to a zero moment image was done via CASA's IMMOMENTS package. The outer and inner HCO^+ contour levels correspond to brightnesses of 0.3 and 0.6 $\mathrm{Jy\,beam^{-1}}$ respectively. There is a difference of ~1,400 days between the Hα and HCO^+ observations, however during this time, the morphology of the Hα emission has not changed significantly (Larsson et al., 2019b), therefore a comparison of these two observations can still reliably be made.

From visual inspection of Figure 2.6, the spatial distribution of the HCO^+ emission is more compact than that of Hα where it is mainly located to the south of the Hα 'keyhole'. The compactness of HCO^+ indicates that the HCO^+ gas does not form in the strongly-ionised regions of the ejecta indicated by the Hα emission, instead it is found deeper within the ejecta where the ionisation levels are milder. This is expected since too strong an ionisation field would dissociate HCO^+ and CO molecules. There is an overlap between the regions of brightest intensity between the Hα and HCO^+ at the western side of the ejecta. This was investigated further by comparing the Hα line velocity profiles in Larsson et al. (2016) with the HCO^+ line velocities in Figure 2.1. While factoring in the systemic velocity of SN 1987A at ~300 $\mathrm{km\,s^{-1}}$ in which the Hα line velocities are corrected for, the majority of the Hα emission is blue-shifted in the western part of the ejecta. Most of the HCO^+ emission in the west is at low red-shifts however, meaning that the HCO^+ and Hα emission do not share co-spatiality in velocity space. In other words, most of the HCO^+ emission in the west appears behind the Hα emission. The regions of low Hα intensity also align

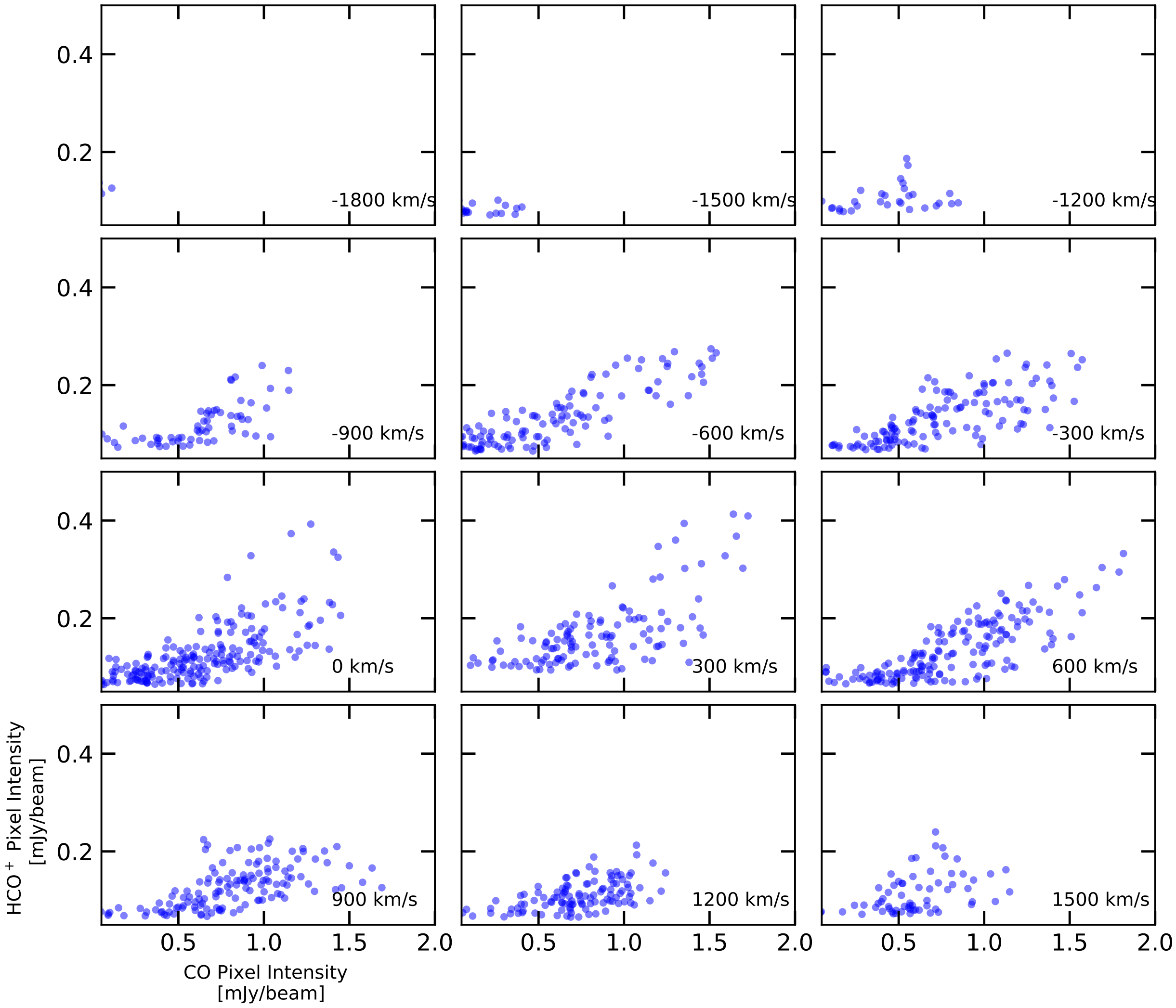

Figure 2.5. Scatter plots of the pixel brightesses of HCO$^+$ (y-axis) versus CO (x-axis) of each 300 km s^{-1} velocity channel. The pixel brightnesses are in units of mJy beam^{-1}. A threshold of 3 times the RMS (~0.07–0.10 mJy beam^{-1}) is introduced to each channel to omit low-brightness pixels belonging to the background. A clear, positive monotonic relationship is seen between HCO$^+$ and CO in channels -600 to 600 km s^{-1}.

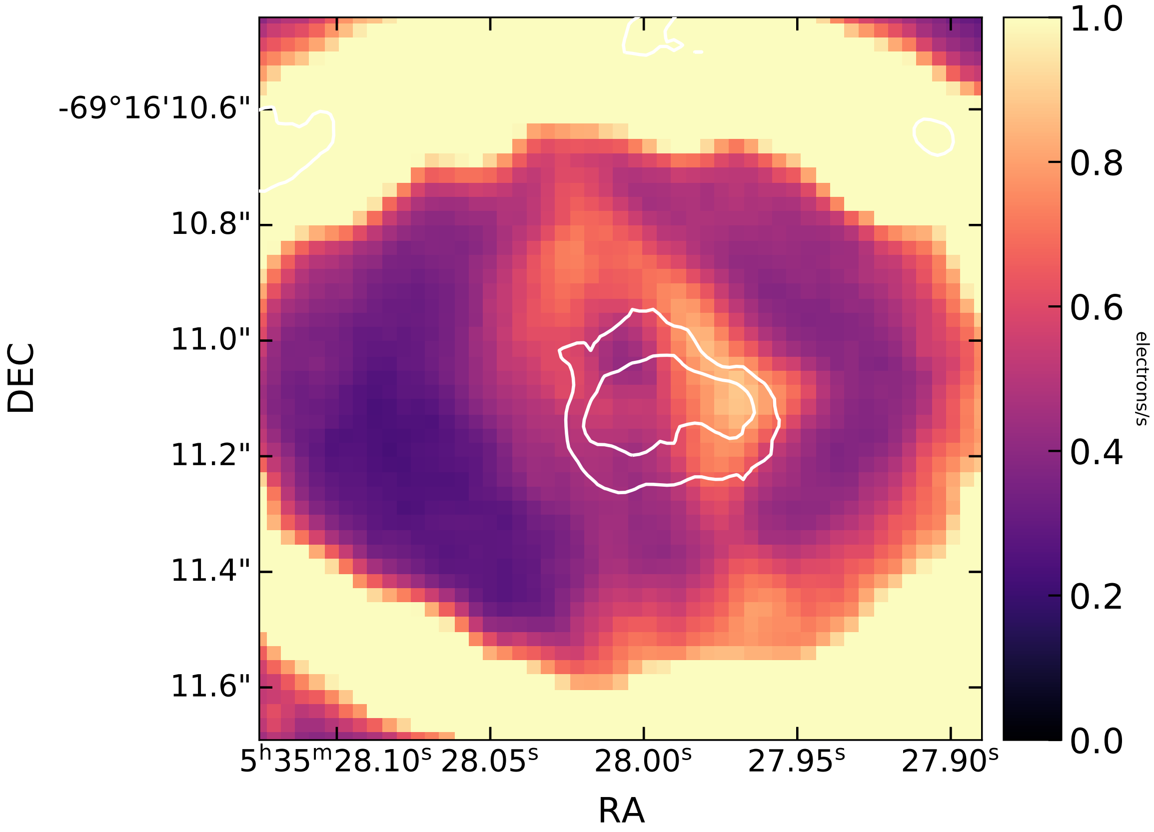

Figure 2.6. The colour image is the *HST* WFC3 F625W observation of the Hα emission which is the predominant emission in this image. This image shows the prominent 'keyhole' shape of Hα emission in the ejecta of SN 1987A. The ring which also contains Hα emission is over-saturated. This is due to the brightness boundaries in this image being chosen to best display the fainter Hα emission of the ejecta. The white contours shows the brightness levels of the continuum-included $J = 3 - 2$ HCO$^+$ emission which has been integrated across its velocity space. These contour levels correspond to HCO$^+$ emission brightnesses of 0.3 and 0.6 Jy beam^{-1} s^{-1}. Both the Hα emission and the HCO$^+$ peak in the western side of the ejecta. There are no other similarities between the two molecular distributions.

with some of the high-intensity HCO^+ emission; particularly in the south.

This comparison cannot be used to decide what heating mechanism powers the HCO^+ emission whether it is energy deposition of X-rays from the ring or whether it is from positron heating of ^{44}Ti. This is due to there being an uncertainty in what causes the lower Hα emission in the south and south-east of the ejecta. Whether it is because the X-ray energy deposition from the ring is low at these regions or alternatively, the Hα emission could be obscured by dust (Cigan et al., 2019; Matsuura et al., 2024).

2.3 Line Intensity Analysis of HCO^+

Physical properties of HCO^+ such as the temperature and mass can be estimated by analysing the HCO^+ line intensities. To begin this analysis, the HCO^+ flux density profile is extracted from the velocity channel map and integrated across frequency space to obtain a line intensity. Then the line intensities can be used as a comparison with modelled HCO^+ line intensities calculated from the radiative transfer code RADEX in which best-fitting values for the temperature and mass of HCO^+ can be found.

Measurement of the flux density profile for the HCO^+ $J = 3 - 2$ transition was done via aperture photometry using CASA's IMAGE.GETPROFILE function. This image and therefore the HCO^+ flux profile contains a contribution from the continuum. The flux is measured from velocities -1050 to 1650 km s^{-1} (corresponding velocity channels in Figure 2.1 are 900 to 1,500 km s^{-1}) due to there being low levels of HCO^+ flux present at velocities ranging from $-1{,}800$ to $-1{,}050$ km s^{-1} (channels$-1{,}800$ to $-1{,}200$ km s^{-1} in Figure 2.1). To investigate the impact of including these channels with low HCO^+ flux in the analysis, the total HCO^+ intensity and its uncertainties was calculated with and without using the velocity channels from $-1{,}800$ to $-1{,}200$ km s^{-1}. It was found that the channels ranging from -1800 to -1200 km s^{-1} would only contribute $\sim$9$-$12 % of the total HCO^+ flux, therefore, due to the low signal of HCO^+ emission in these channels, they were excluded from further analysis.

Across the velocity range, the beam size, velocity increments and aperture for flux extraction size were kept constant. The aperture dimensions for flux extraction had semi-major and semi-minor axes of $0.368'' \times 0.446''$ respectively and an orientation angle of 0°. The semi-major and minor axes are aligned to the declination and right-ascension sky coordinates respectively. The aperture size was chosen to capture most of the HCO^+ emission while avoiding to capture any flux from the ER.

Transition	$I_{\rm tot}$ $\times10^{-20}$ [W/m^2]	$C_{\rm dust}$ $\times10^{-20}$ [W/m^2]	$I_{\rm HCO^+}$ $\times10^{-20}$ [W/m^2]	Error^a $\times10^{-20}$ [W/m^2]	Error^b 10^{-20} [W/m^2]	Error^c $\times10^{-20}$ [W/m^2]
$J=3-2$	10.52	2.69	7.83	$\pm$0.55	$\pm$0.18	$\pm$0.78
$J=4-3$	15.87	10.17	5.69	$\pm$0.40	$\pm$0.24	$\pm$2.54

Table 2.1. Line intensities and continuum estimations for HCO$^+$ along with uncertainties in the line emission measurements. $I_{\rm tot}$ - the total integrated intensities for the respective transitions, this is the sum of the HCO$^+$ line intensity and the dust continuum intensity level. $C_{\rm dust}$ - the dust continuum intensity levels estimated using the fitted modified blackbody to thermal dust observations in Figure 2.3. $I_{\rm HCO^+}$ - the line intensity for HCO$^+$ with the continuum levels subtracted. Error ^{a} - Uncertainty of flux calibration in ALMA data cubes. Error ^{b} - RMS in data cubes. Error ^{c} - Uncertainty in continuum level estimation (30% of $C_{\rm dust}$).

2.3.1 Continuum-Subtracted HCO$^+$ Line Intensities

The continuum-included HCO$^+$ fluxes from Sect. 2.3 are integrated across the $J=3-2$ and $J=4-3$ frequency ranges to obtain the HCO$^+$ line intensities. The continuum levels found in the previous subsection were subtracted from the continuum-included HCO$^+$ line intensities. There are three predominant contributions to the uncertainties of the HCO$^+$ line intensities. These are the RMS in the velocity channel maps, the flux calibration uncertainty and the uncertainty in the estimated continuum level, all discussed in Sections 2.1.1 and 2.2.3. Continuum included and subtracted HCO$^+$ line intensities, continuum levels and uncertainties are found in Table 2.1. The largest uncertainty originates from the uncertainties in the continuum level estimation. For the $J=3-2$ and $J=4-3$ HCO$^+$ transitions these are $\pm0.78\times10^{-20}$ and $\pm2.54\times10^{-20}\,\mathrm{W\,m^{-2}}$. These are larger than the summed flux calibration and RMS uncertainties of $\pm0.73\times10^{-20}$ and $\pm0.64\times10^{-20}$ $\mathrm{W\,m^{-2}}$ for the $J=3-2$ and $J=4-3$ HCO$^+$ transitions respectively, seen also in Table 2.1.

Figure 2.7 shows the flux density profiles of the $J=3-2$ and $J=4-3$ HCO$^+$ transitions and how they compare to the estimated continuum levels and the uncertainties associated with the HCO$^+$ flux. The observed fluxes of the HCO$^+$ emission are shown as solid black circles. The red and blue error bars on the HCO$^+$ fluxes are the flux calibration uncertainty and RMS uncertainty respectively. The yellow line and pink-shaded region show the continuum level MC fit and its associated uncertainty in the fit respectively.

To model these line intensities in the subsequent section (Sect. 2.4.1), the FWHM of the HCO$^+$ flux density profiles need to be estimated. This was done by fitting a gaussian profile to the continuum-subtracted HCO$^+$ fluxes, the fit was extrapolated to the high velocity 'wings' of potential HCO$^+$ emission at around $\pm$2,000 $\mathrm{km\,s^{-1}}$ and the uncertainties of the RMS, flux calibration and continuum level estimation are included for the error in the fit. The resulting gaussian fit to the HCO$^+$ flux density profile is shown as the solid black line in Figure 2.7, but note that the continuum level has been added back onto the fit and HCO$^+$ flux points. The standard deviation, v_σ, of the gaussian fitted to the HCO$^+$ flux points is used to calculate the FWHM, $v_{\rm FWHM}$, of the HCO$^+$ line emission, via $v_{\rm FWHM}$= $2v_\sigma\sqrt{2\ln 2}$ and for the $J = 3-2$ HCO$^+$ flux density profile, the FWHM was 1,906 km s^{-1}. This FWHM was fixed at 1,906 km s^{-1} to fit the $J = 4-3$ HCO$^+$ transition since doppler-broadening of the lines should be equal as the expansion of the ejecta is homologous. These gaussian fits to the flux density profiles also enabled the estimation of the symmetrical center of the flux density profiles, which were 260±60 km s^{-1} and 250±200 km s^{-1} for the $J = 3-2$ and $J = 4-3$ HCO$^+$ transitions respectively. The large symmetrical center uncertainties arise from the large uncertainties in the continuum level. The ∼250 km s^{-1} offset of the symmetrical centers of the lines are consistent to the systematic regressional velocity of SN 1987A at 286.7 km s^{-1} (Gröningsson et al., 2008).

The continuum-subtracted HCO$^+$ line intensities are found to be $I_{\rm HCO+}$ = (7.83 ± 0.45) $\times 10^{-20}$ W m^{-2} and (5.69 ± 1.04) $\times 10^{-20}$ W m^{-2} for the $J = 3-2$ and $J = 4-3$ HCO$^+$ transitions respectively. A study by Matsuura et al. (2017) conducted a spectral line survey of the ejecta of SN 1987A in the sub-mm, found a $J = 3–2$ HCO$^+$ line intensity of (6.7±0.6)×10^{-20} W m^{-2} which is in agreement with my $J = 3-2$ HCO$^+$ line intensity by 3σ, with my HCO$^+$ line intensity being slightly larger.

2.4 RADEX

2.4.1 RADEX and Model Inputs

To help infer properties of the HCO$^+$ gas such as its mass and temperature, my observed line intensities can be compared to theoretical line intensities calculated using RADEX (van der Tak et al., 2007). The computer software program RADEX can solve the radiative transfer equation for a wide range of molecules, via LTE and non-LTE assumptions whilst also considering simple background and internal radiation sources. I used the python version[¶] of RADEX which required the input of kinetic temperature ($T_{\rm kin}$), column density of HCO$^+$ ($N_{\rm HCO^+}$) and so, through fine-tuning of these parameters and in order to replicate the observed HCO$^+$ line intensities, values for ($T_{\rm kin}$) and ($N_{\rm HCO^+}$) can be found which are representative of the HCO$^+$ observed in SN 1987A. The inputs of ($T_{\rm kin}$) varied from 10 to 100 K and ($N_{\rm HCO^+}$) varied from 10^{14} to 10^{16} cm^{-2}, with both being varied using a logarithmic scale.

[¶] `https://pythonradex.readthedocs.io/en/latest/`

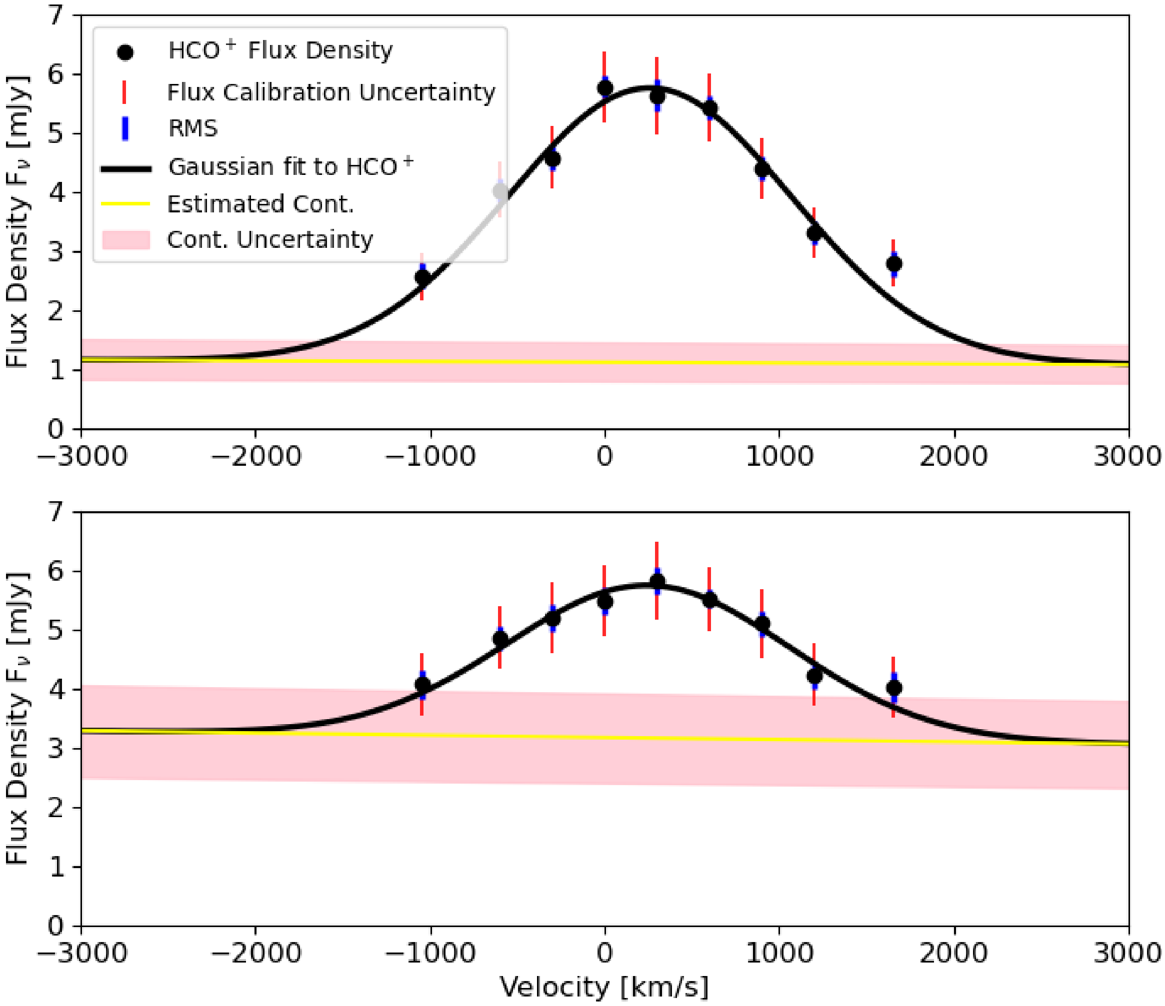

Figure 2.7. The upper panel displays the flux density profile of the $J = 3 - 2$ HCO$^+$ line emission is seen as the solid circle markers. The RMS and systematic flux calibration uncertainties associated with these flux measurements are shown as the blue and red error bars respectively. The profile is fitted with a gaussian fit to measure the emission line's FWHM; found to be $\pm 1906\,\mathrm{km\,s^{-1}}$. The same is done for the $J = 4 - 3$ HCO$^+$ emission in the lower figure panel. The best-fitting continuum level estimated via the Monte-Carlo analysis to thermal dust emission is seen as the yellow line. The uncertainty in the continuum fit is shown as the pink shaded region.

The RADEX code also requires the inputs of Einstein coefficients A, B and C of HCO$^+$, statistical weights of level populations g_i and g_j, a homogenous geometry of the emitting medium, any background radiation fields and properties of the line emission such as its FWHM and projected solid angle. A, B and C and the statistical weights are obtained from the LAMDA database (Schöier et al., 2005). The geometry of the HCO$^+$ cloud, used to calculate the escape probability of photons from the cloud is assumed to be that of a static and uniform spherical geometry, thus leading to an escape probability defined Eq. 1.21 from Sect. 1.3.2 (van der Tak et al., 2007). No external emitting field other than the ambient Cosmic Microwave Background is assumed which RADEX has its own in-built function for. Line properties such as the solid angle of emission and the line's FWHM are taken from my HCO$^+$ line observations in Sect. 2.3 and 2.3.1. The final input parameter is the collisional partner density. The collisional partner density is assumed to be H$_2$ due to there being no other HCO$^+$ collisional partners available in LAMDA. I estimate the H$_2$ densities of the remnant at 30 years since its explosion by the following simple estimation. The expansion velocity of the ejecta can be estimated using $v_{\mathrm{ejecta}}=\frac{v_{\mathrm{FWHM}}}{\sqrt{2}}$ (McCray, 1993) where v_{FWHM} is the FWHM line width of my HCO$^+$ emission, at 1,900 km s^{-1} which therefore gives an ejecta expansion velocity of 1,300 km s^{-1}. Assuming the hydrogen envelope is $\sim$6 M$_\odot$, then, at the end day of our HCO$^+$ observations (d$_{\mathrm{SN}}$ = 11,844), the H$_2$ density is $\sim$3$\times$10^5 cm^{-3}. Hence, I adopt a H$_2$ collisional partner density of 10^5 cm^{-3}. I also adopt a H$_2$ collisional partner density of 10^6 cm^{-3}, to aid with comparison of the HCO$^+$ mass found in Matsuura et al. (2017) who use a H$_2$ density of 10^6 cm^{-3}. Two caveats to this analysis is that it is likely that only part of the 6 M$_\odot$ hydrogen envelope is inwardly mixed to the inner regions of the ejecta to form HCO$^+$ thus leading to a lower H$_2$ density. The exact quantity of inwardly mixed H$_2$ is unknown but models assume it to be $\sim$2 M$_\odot$ (e.g. Kozma & Fransson 1998; Jerkstrand et al. 2011). Additionally, my simple H$_2$ density estimation using the expansion velocity of the ejecta assumes a uniform distribution of H$_2$ in the ejecta, which is quite unlikely, since HCO$^+$ and CO appear to be clumpy, therefore the high densities of 10^5 and 10^6 cm^{-3} are more representative of the densities of clumps of H$_2$ in the ejecta. I adopt collisional partner densities of 10^5 and 10^6 cm^{-3} with the assumption that these densities are representative of not the whole ejecta, but of the regions where HCO$^+$ is present instead. The outputs of RADEX are the level populations, excitation temperatures, optical depth and most importantly, the line intensities.

2.4.2 Chi Square Analysis

A chi-square, χ^2, goodness-of-fit test is required to finely tune the input parameters T_{kin} and $N_{\mathrm{HCO^+}}$ to replicate theoretical line intensities that closely match with the observed HCO$^+$ line intensities. The χ^2 test itself is set up between the observed and theoretical HCO$^+$ line

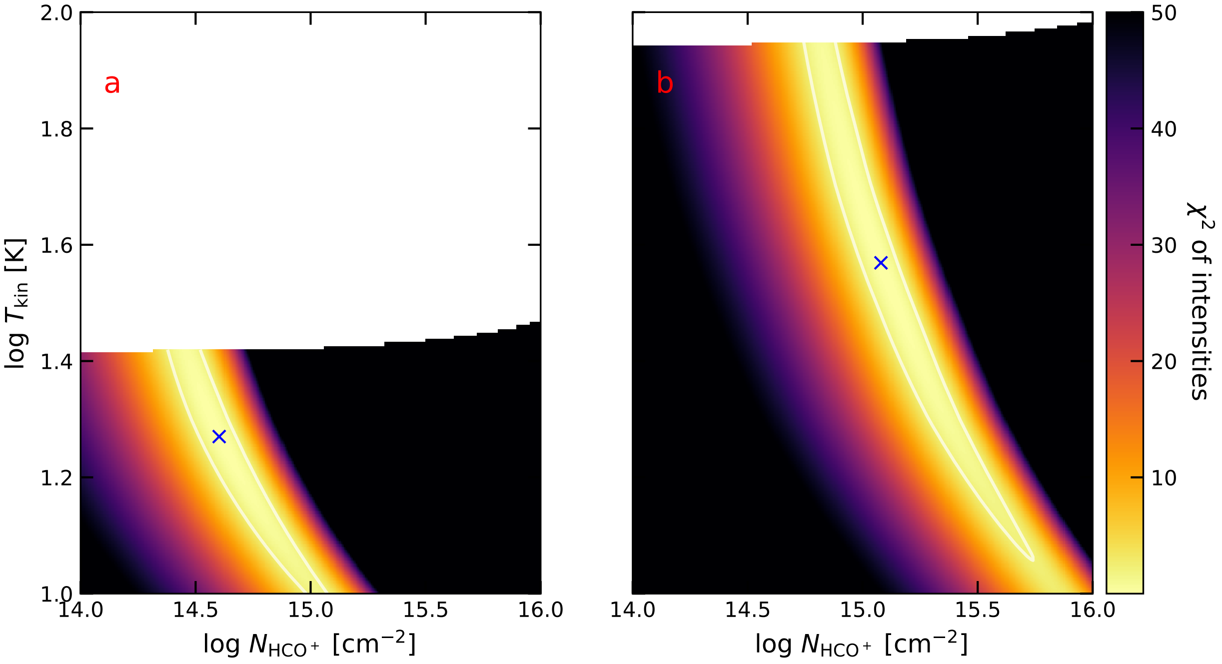

Figure 2.8. The χ^2 distributions for the comparison of calculated RADEX HCO$^+$ line emissions with the observed continuum-subtracted line emission with respect to the input RADEX parameters of column density of HCO$^+$, $N_{\rm HCO^+}$, and kinetic temperature of the HCO$^+$ gas, $T_{\rm kin}$. The sub-plots (a) and (b) show the χ^2 distributions for the HCO$^+$ line intensities at H_2 collisional partner densities of 10^6 and 10^5 cm^{-3}, respectively. The blue cross marks the location of the minimum χ^2 value and therefore the best-fitting $T_{\rm kin}$ and $N_{\rm HCO^+}$ to the observed HCO$^+$ line emission. The white countour on the χ^2 distributions the 1σ level standard deviation of the χ^2 distributions. The white spaces at the top of the subplots show regions in the parameter space which returned a negative τ in the running of RADEX, the resulting χ^2 distributions were omitted from further analysis.

intensities. The colour plot of Figure 2.8 shows the summed χ^2 distribution for the $J = 3-2$ and $J = 4-3$ transitions of HCO$^+$ with respect to the corresponding RADEX input parameters of T_{kin} and $N_{\mathrm{HCO^+}}$. The subplots (a) and (b) display the χ^2 distributions for the fixed H$_2$ collisional partner densities of 10^6 and 10^5 cm^{-3}, respectively. χ^2_{min} returns the best fit of the RADEX line intensities with the observed HCO$^+$ line intensities which are denoted by the blue crosses in Figure 2.8. The χ^2_{min} values are 0.4$\times10^{-3}$ for subplot (a) and 0.6$\times10^{-3}$ for subplot (b). The white contour in Fig. 2.8 shows the 1σ significance level for the χ^2 distribution which was calculated by setting a χ^2 confidence interval of $\chi^2_{\mathrm{min}} + \Delta\chi^2$, where $\Delta\chi^2$ for two interesting parameters at 1σ is $\Delta\chi^2$=2.30 (Avni, 1976; Press et al., 1999). As seen from Figure 2.8, T_{kin} and $N_{\mathrm{HCO^+}}$ show a fair degeneracy. This originates from the large uncertainties associated from the observed HCO$^+$ line intensity which were used as the error input for the χ^2 analysis. The best fitting values for T_{kin} and $N_{\mathrm{HCO^+}}$ are T_{kin}=($18.6^{+7.6}_{-8.6}$) K and $N_{\mathrm{HCO^+}}$=($4.0^{+7.8}_{-1.6}$)$\times10^{14}$ cm^{-2} for a collisional partner density of 10^6 cm^{-3} and T_{kin}=($37.1^{+51.7}_{-25.6}$) K and $N_{\mathrm{HCO^+}}$=($1.2^{+4.3}_{-0.6}$)$\times10^{15}$ cm^{-2} for a collisional partner density of 10^5 cm^{-3}.

A limitation to the RADEX analysis was encountered, affecting the range of T_{kin} input parameters and therefore the χ^2 analysis. A negative optical depth value (τ) was returned in the outputs for the HCO$^+$ $J = 1-0$ for T_{kin} of ~26 K and ~89 K for the 10^6 and 10^5 cm^{-3} collisional partner densities respectively. This is a known numerical error with RADEX (van der Tak et al., 2007) rather than a physical solution. Therefore any RADEX outputs with a negative τ in any of the transition solutions, were discarded from further analysis. The negative τ regions in Fig. 2.8 are shown as the white regions at the top of the χ^2 distributions. An assumption in this analysis is that the dominant collisional partner for HCO$^+$ is H$_2$, this is due to it being the only collisional partner available for HCO$^+$ on LAMDA.

2.5 Calculation of the HCO$^+$ Mass

The mass of HCO$^+$, $M_{\mathrm{HCO^+}}$, can be calculated from the column densities found in the previous section via the equation below.

$$M_{\mathrm{HCO^+}} = f\Omega N_{\mathrm{HCO^+}} D^2 m \tag{2.6}$$

f is the filling factor, which is assumed to be 1, Ω is the solid angle of the HCO$^+$ emission in steradians, $N_{\mathrm{HCO^+}}$ is the HCO$^+$ column density in cm^{-2}, D is the distance to SN 1987A, taken to be 51.2 kpc (Panagia et al., 1991) and m is the mass of 1 HCO$^+$ molecule in kg. Using the best-fitting $N_{\mathrm{HCO^+}}$ values found from the χ^2 analysis in Sect.2.4, leads to HCO$^+$ masses of ($2.9^{+5.7}_{-1.2}$)$\times10^{-6}$ M$_\odot$ for a collisional partner density of 1$\times10^6$ cm^{-3} and ($8.80^{+31.5}_{-4.7}$)$\times10^{-6}$ M$_\odot$ for a collisional partner density of 1$\times10^5$ cm^{-3}.

A previous study by Matsuura et al. (2017) estimated the HCO$^+$ mass from the HCO$^+$ $J = 3-2$ and $J = 4-3$ emission, where the $J = 4-3$ emission was treated as an upper limit. A mass of M_{HCO^+} $\leq$5×10^{-6} M$_\odot$ was calculated at a H$_2$ collisional partner density of 10^6 cm^{-3}. My mass, (2.9$^{+5.7}_{-1.2}$)×10^{-6} M$_\odot$, at the same collisional partner density, is consistent within error but its value is smaller than Matsuura et al. (2017).

Chapter 3

Discussions, Conclusion and Future Work

> *"To see the world, things dangerous to come to,*
> *to see behind walls, to draw closer,*
> *to find each other and to feel.*
> *That is the purpose of life."*

Secret Life of Walter Mitty. *2013*

3.1 Discussion

In this work, the emission of two HCO$^+$ transitions at 267.56 and 356.73 GHz have been analysed. The detection of HCO$^+$ within the ejecta of SN 1987A is a novel one with the first detection being reported in (Matsuura et al., 2017). Due to this, there are very few studies predicting the formation of HCO$^+$ within supernova remnants. Using the HCO$^+$ observations, I discuss potential HCO$^+$ formation chemical reactions which may occur in SN 1987A. I also discuss the possible scenarios before and during the supernova explosion which cause hydrodynamical mixing between the stratified layers of different elemental compositions, and how this mixing can benefit the formation of HCO$^+$ in later years.

3.1.1 Chemistry of Formation of HCO$^+$

The spatial distributions of the $J = 3 - 2$ HCO$^+$ emission and the $J = 2 - 1$ CO emission were found to be very similar and with a strong correlation strength of 0.72 in Sect. 2.2.4 and 2.2.6. This could imply that HCO$^+$ forms from chemical reactions involving CO. Furthermore, a reaction with CO may be the dominant formation of HCO^+ in the remnant, as large abundances of CO in the ejecta of SN 1987A of 0.02−1 $M_\odot$ were observed by Matsuura et al. (2017). I investigate this further by calculating a simple order of magnitude estimate of how much HCO^+ is formed in the ejecta across time by using a HCO^+ formation reaction rate which involves CO as a reactant. A starting point of this estimation is the rate equation for a reaction:

$$R_{\mathrm{HCO^+}} = k(T)[A][B] \tag{3.1}$$

where $R_{\mathrm{HCO^+}}$ is the rate of the reaction in $\mathrm{cm^{-3}s^{-1}}$, $k(T)$ is the reaction rate coefficient for a specific reaction in $\mathrm{cm^3s^{-1}}$ and [A] and [B] are the number densities of the chemical reactants A and B in $\mathrm{cm^{-3}}$. There is little literature on potential chemical reactions of HCO^+ formation in supernova remnants (e.g. Rawlings & Williams 1990; Cherchneff & Dwek 2009). Therefore, I use the UMIST database for astrochemistry to search for a HCO^+ formation reaction which: occurs in the ISM, has CO as one of the reactants and has the potential to occur in supernova remnants. The UMIST database (Millar et al., 1991, 1997; Le Teuff et al., 2000; Woodall et al., 2007; McElroy et al., 2013; Millar et al., 2024) provides the $k(T)$ of ~8,000 molecular formation reactions in the ISM which are derived from literature, lab measurements and modelling. One such reaction which satisfies the above criteria is shown in Eq. 3.2. Other HCO^+ formation reactions in the ISM involving other molecules such as $CH^+ + H_2O \rightarrow HCO^+ + H_2$ and $CO^+ + HCO \rightarrow HCO^+ + CO$ (Millar et al., 2024), could also occur in supernova environments. Reaction 3.2 was chosen as the reaction to analyse because the number densities of CO in SN 1987A can be derived from observations and the number density of H_3^+ can be estimated from my H_2 collisional partner densities (see later). Whereas molecules like CH^+ and H_2O have yet to be observed in SN 1987A and therefore their number densities are unknown.

$$\mathrm{H_3^+ + CO \rightarrow HCO^+ + H_2} \tag{3.2}$$

Reaction 3.2 has a high $k(T)$ across a temperature range of 10 K to 300 K which from Sect. 2.4 is fairly representative of the temperatures of the HCO^+ gas in the remnant at present day. A high $k(T)$ indicates that the HCO^+ formation reaction can occur more rapidly, and therefore create more HCO^+ within a set timescale compared with a formation reaction with a lower $k(T)$. Therefore, the rate equation in 3.1 now becomes:

$$R_{\mathrm{HCO^+}} = k(T) n_{\mathrm{CO}} n_{\mathrm{H_3^+}} \tag{3.3}$$

where n_{CO} and $n_{\mathrm{H_3^+}}$ are the number densities of the reactants CO and H_3^+ respectively from the formation reaction in Eq. 3.2.

Next, I set a suitable timescale for HCO^+ to form in the remnant. This is between d_{SN}=1,000 and d_{SN}=11,499 which correspond to dates in November 1989 and August 2018. d_{SN}=1,000 corresponds to the time when masses of CO and H_2, calculated from chemical models, reach stability within the ejecta (Culhane & McCray, 1995; Sarangi & Cherchneff, 2013; Ono et al., 2024). The latter day of d_{SN}=11,499 corresponds to the middle day of the HCO^+ observations, the middle day was selected since these observations spanned across 2 years.

The number density of CO, $n_{\rm CO}$, can be calculated from its mass found in Matsuura et al. (2017), assuming that the CO mass remains stable past d_{SN}=1,000 (e.g. Sarangi & Cherchneff 2013) and therefore the number of CO particles remains constant across 30 years. Additionally, I assume that the CO and H_3^+ molecules in the remnant have a uniform distribution, in other words, the gas is chemically well-mixed. Observations of H_3^+ in SN 1987A have not yet been confidently confirmed, with a tentative observation reported in Miller et al. (1992), therefore estimating its number density for the formation rate of HCO^+ is uncertain. Instead, the number density of H_3^+, $n_{\rm H_3^+}$ is approximated using its number density relationship for dense clouds in the ISM; (Oka, 2006). This relationship is given by:

$$n(H_3^+) = \frac{\zeta}{k_{\rm H_3^+}} \times \left(\frac{n(H_2)}{n(CO)}\right) \tag{3.4}$$

where ζ is the rate of cosmic-ray ionisations of H_2 within the dense cloud which forms H_3^+ via H_2^++H_2 →H_3^++H_2. $n_{\rm H_2}$ is the number density of H_2. $k_{\rm H_3^+}$ is the reaction rate coefficient for the dominant reaction which destroys H_3^+ in the dense cloud in which Oka (2006) assumed to be Eq. 3.2. Therefore, $k(T)$ in Eq. 3.2 and $k_{\rm H_3^+}$ in Eq. 3.4 are for the same chemical reaction, which I set to be equal to each other.

A constant value of $k(T)$ of 2×10^{-9} $cm^3\,s^{-1}$ is assumed by Oka (2006). I investigate the change in $k(T)$ across my 30-year timescale by estimating how much the temperature of the remnant changes in this time and how it affects $k(T)$. I use the approximation from Sarangi & Cherchneff (2013) to estimate the change in the ejecta's temperature with time, which is given by:

$$T_{gas}(m_{\rm C+O}, d_{\rm SN}) = T_{gas}(m_{\rm C+O}, 100) \times (d_{\rm SN}/100)^{-1.26} \tag{3.5}$$

where $T_{gas}(m_{\rm C+O}, d_{\rm SN})$ is the temperature of the gas at the carbon and oxygen zone inside the ejecta at a time in days since the supernova explosion $d_{\rm SN}$, $T_{gas}(m_{\rm C+O}, 100)$ is the temperature of the same mass coordinate at $d_{\rm SN}$=100 days which is taken to be 7580 K for the C+O zone (see Table 2, Zone 4B in Sarangi & Cherchneff (2013)). The temperature, initially at 417 K, at $d_{\rm SN}$=1,000 decreases to about 20 K by $d_{\rm SN}$=11,499. This results in a change in $k(T)$ from 1.3×10^{-9} $cm^3\,s^{-1}$ at $d_{\rm SN}$=1,000 to 2.4×10^{-9} $cm^3\,s^{-1}$ at $d_{\rm SN}$=11,499. Since I am interested in a simple order of magnitude estimate of the HCO^+ mass that forms from the reaction rate via Eq. 3.2, and the fact that the change in $k(T)$ is quite small across my timescale for HCO^+ formation, the constant value of $2\times10^{-9}\,cm^3\,s^{-1}$ in (Oka, 2006) is sufficient to use for my mass estimate.

Substituting in the dense cloud relation for $n_{\mathrm{H}_3^+}$ (Eq. 3.4 into Eq. 3.3) reduces the HCO^+ formation rate equation to:

$$R_{\mathrm{HCO}^+} = \zeta \times n(H_2) \tag{3.6}$$

ζ is taken to be $3\times10^{-17}\,s^{-1}$ (Oka, 2006) which is a typical ionisation rate for the ISM as a starting point for the calculations. The picture of the ionisation rate of H_2 in the inner ejecta regions of SN 1987A however, is more complex and relatively unknown. I discuss the effect this has on the mass calculations at the end of this section.

The parameter of n_{H_2} is dependent on the expansion of the ejecta which expands with time. This leads to R_{HCO^+} also having a dependency on time. The expanding volume of HCO^+ across the 30 year timescale also needs to be estimated to calculate the total amount of HCO^+ particles formed later on. To estimate the HCO^+ volume in the ejecta, denoted V_{HCO^+}, the HCO^+ aperture in Sect. 2.3 is used as the extents of HCO^+ at d_{SN}=11,499 which is converted into a cylindrical volume. The collisional partner densities of H_2 in Sect. 2.4.1 are used as the n_{H_2} values for d_{SN}=11,499. The n_{H_2} and V_{HCO^+} at d_{SN}=11,499 are evolved backwards to d_{SN}=1,000 assuming a homologous t^{-3} relationship. This accounts for the ejecta being more compact at earlier days due to the expansion velocity of the ejecta. The volume of the HCO^+ is overestimated however due to the fact that the HCO^+ aperture in Sect. 2.3 was designed to encapsulate all of the HCO^+ flux and the size of the aperture is kept constant across each velocity channel in the HCO^+ channel map. It is most likely however, that the HCO^+ emission follows an ellipsoidal/toroidal distribution like that of CO (e.g. Abellán et al. 2017; Cigan et al. 2019) rather than a cylindrical case which I calculated from the HCO^+ aperture. This volume will ultimately overestimate the HCO^+ mass formed over the 30 year timescale.

The rate of HCO^+ formation, R_{HCO^+} has the units: $cm^{-3}\,s^{-1}$. So, to find the number of HCO^+ particles formed across the 30-year timescale, I need to multiply it by V_{HCO^+} per time-step, then integrate across the timescale, as shown by the equation below.

$$N_{p\,\mathrm{HCO}^+} = \int_{d=1000}^{d=11499} R_{\mathrm{HCO}^+} \times V_{\mathrm{HCO}^+}\, dt \tag{3.7}$$

N is traditionally used for denoting the number of particles in chemistry, which has already been defined in this thesis as the column density, N_{col} (Sect. 1.3.2) and N_{HCO^+} (Sect. 2.4); as the number of energy levels of molecular transitions, N_E (Sect. 1.3.2), as number of observations N_o

in (Sect. 2.4.2), and the number of models N_m in (Sect. 2.4.2). Therefore, I denote the number of particles in this thesis as N_p and hence, number of HCO$^+$ particles as $N_{p\,\mathrm{HCO^+}}$. The number of particles can therefore be converted into a mass via the equation below.

$$M_{\mathrm{HCO^+}} = N_{p\,\mathrm{HCO^+}} \times \frac{m_r}{N_A} \tag{3.8}$$

Where m_r is the molar mass of HCO$^+$, taken to be 0.029 kg mol^{-1} and N$_A$ is Avogadro's constant: 6.02×10^{23} mol^{-1}. The mass of HCO$^+$ formed by d_{SN}=11,499 is of the order of ∼10^{-5} M$_\odot$. This is an order of magnitude above the mass calculation from my observations which are 3−9×10^{-6} M$_\odot$. This creates more HCO$^+$ than what is observed due to the assumption that CO and H$_2$ (and therefore H$_3^+$) having a uniform distribution across the ejecta, i.e. CO and H$_3^+$ are completely mixed within the ejecta. In reality, the existence of CO clumps in the ejecta (Abellán et al., 2017) shows mixing is finite. The more realistic approach would in-fact limit the places where CO and H$_3^+$ are mixed with each other, effectively reducing the volume across which HCO$^+$ forms. This would reduce HCO$^+$ mass formed. Future work on chemical reactions must consider a more realistic mixing scenario. Another uncertainty in this calculation is the choice of ζ at 3×10^{-17} s^{-1}. Although this is a typical cosmic-ray ionisation rate for the ISM, it may not be representative of the ionisation rate in the remnant of SN 1987A where the ejecta is subjected to additional sources of ionising radiation, and therefore I suspect the ionisation rate to be higher. In fact, in supernova remnants such as the Crab, the ionisation rate is roughly 10^{10} s^{-1} (e.g. Priestley et al. 2017). I suspect sources of ionising radiation in the outer layers of the ejecta to originate from the energy deposition of X-rays from the ring (e.g. Fransson et al. 2013) and the source of ionisation of the inner layers of the ejecta to arise from the pulsar wind nebula from the compact object (Fransson et al., 2024) and/or from the decay of ^{44}Ti, albeit ionisations resulting from ^{44}Ti decay are quite low (see McCray & Fransson 2016 and references therein). A higher ionisation rate of H$_2$ would lead to a greater amount of H$_3^+$ in the ejecta which, reacting with the abundant CO will therefore increase the HCO$^+$ mass formed. The ionisations which occur in the region of HCO$^+$ formation must also be relatively mild as stated in Sect. 2.2.7 as introducing higher levels of ionisation would begin to dissociate the molecules.

This order of magnitude mass estimate is ∼12 orders of magnitude greater than the HCO$^+$ mass calculated from the HCO$^+$ abundance estimate in Rawlings & Williams (1990), who predicted a HCO$^+$ abundance of 10^{-18}. The mass of HCO$^+$ from this abundance was found by multiplying the abundance by the assumed mass of the 'core' and 'envelope' taken to be ∼16 M$_\odot$ (Woosley, 1988). The reason for the large difference in values is that Rawlings & Williams (1990) considered HCO$^+$ formation in a hydrogen-poor environment in the ejecta of SN 1987A with H-abundances in the core as high as ∼10^{-4}. From this, I speculate that HCO$^+$ formation is more efficient when there is a greater amount of hydrogen present in the CO gas. However, a caveat to this is that hydrogen mixed into the inner layers of the ejecta can greatly impact the chemistry in the remnant. An example of this is the study by Cherchneff & Dwek (2009), who model the formation of molecules in population III supernova remnants, they found that inwardly mixing the hydrogen by 10% introduces hybrid molecules such as OH and H_2O. These molecules have yet to be seen in SN 1987A however. To confidently validate the claim that Eq. 3.2 is the dominant HCO^+ formation route in SN 1987A, a full chemical network of HCO^+ formation in the ejecta is required, where alternative HCO^+ formation molecules such as CH^+, OH, H_2O, HCO, CO_2 and CO^+ (e.g. Millar et al. 2024), in addition to CO, are taken into account. However, the simple calculation of how much HCO^+ forms from a single formation reaction with CO makes a reasonable amount of mass thus supporting the feasibility of HCO^+ forming from CO in the ejecta, provided that hydrogen is also co-located with the CO.

3.1.2 Mixing

The previous estimation of HCO^+ mass formed in the ejecta using CO as a reactant comes with the condition that a large amount of hydrogen needs to be present within the CO gas in order for HCO^+ to form. Now I will discuss how this could be met in the ejecta of SN 1987A. This hydrogen needs to be inwardly mixed from the hydrogen-rich envelope which surrounds the inner ejecta. In an unmixed scenario, the carbon and oxygen-rich gasses remain separated from the hydrogen-rich gas due to the the structure of the progenitor star (e.g. Woosley et al. 1988a,b) and in Sect. 1.2.4, being retained post-explosion and so, HCO^+ cannot form in the remnant. I also assume, in my HCO^+ mass formed from its formation rate with CO estimation, that H_3^+ and CO are uniformly, and thoroughly mixed. This is not realistic given that the progenitor structure is partially retained after the explosion due to the distribution of molecular clumps in the ejecta which are spatially separate (e.g. Abellán et al. 2017). Therefore, the extent of the mixing the ejecta has undergone and how it is mixed is still a questions that needs to be answered.

Firstly, I'll discuss a form of mixing that does occur in SN 1987A, then I'll speculate about two additional forms of mixing which could also occur in the remnant which could enhance the formation of HCO^+ and therefore lead to a HCO^+ mass to match my observed HCO^+ mass of $10^{-6}\ M_\odot$. The first form of mixing, is macroscopic mixing. As introduced in Sect. 1.2.4, macroscopic mixing is a form of large-scale mixing of heavy metals (such as Ni) outwards from the core and hydrogen mixing inwards from the envelope. This mixing occurs as massive clumps of material through the different layers of nuclear burning zones left behind by the progenitor star. It is caused by Rayleigh-Taylor instabilities which arise from density discontinuities at the interfaces of nuclear burning zones (Herant & Benz, 1992; Hammer et al., 2010; Wongwathanarat et al., 2015; Utrobin et al., 2015, 2019; Gabler et al., 2021). This type of mixing, which occurs within a few days after the supernova explosion, can transport clumps of hydrogen from the outer envelope into the CO gas which resides in the inner ejecta. However, as mentioned earlier, the clumps themselves retain their hydrogen compositions and do not mix with the surrounding CO gas. I speculate that other forms of mixing are required to mix hydrogen into the carbon and oxygen-rich gas. Two potential forms of mixing that can do this are described below. This first is called microscopic mixing which can occur alongside macroscopic mixing and it can enhance HCO^+ formation by mixing the hydrogen gas from the clumps into the CO-rich gas. This form of mixing however, fails to support the observations of the mass of CO at early epochs. Chemical models of early (d_{SN} $\lesssim$1,000) CO formation in SN 1987A by Lepp et al. (1990) and Liu & Dalgarno (1995) showed that microscopic mixing would also incorporate destructive He^+ into regions of the CO gas, where He^+ dissociates it thus leading to lower CO masses than what was observed. CO masses in the model could only replicate the CO mass observations when no microscopic mixing was considered in the model. Additionally, clumps of CO and SiO are distinctly separate in the ejecta, which argues against microscopic mixing (Abellán et al., 2017) which would otherwise appear to be blended if microscopic mixing was prevalent in the ejecta. The second type of mixing I speculate could also occur is a type of small-scale mixing which occurs in the progenitor star before it goes supernova (Groh et al., 2019; Farrell et al., 2021). This involves interactions between the He/H zones in BSG stars which mix hydrogen into the helium nuclear burning zone where small abundances of carbon and oxygen also exist (e.g. Woosley et al. 1988a). However, this type of pre-SN mixing has only been researched in evolved stars of low metallicity ($Z{\sim}0.0004\,Z_\odot$). Despite SN 1987A's progenitor is assumed to have a low metallicity which is $\sim \frac{1}{2} Z_\odot$ (e.g. Woosley et al. 1988a; Russell & Dopita 1992), this form of mixing may only be efficient in stars with an extremely low metallicity such as population III stars in the early universe. Another form of pre-SN mixing can also occur which can enhance the HCO^+ formation and that is mixing due to turbulent convection in stars $\geq$20 $M_\odot$ (Frey et al., 2013). This turbulent mixing can deform the boundary interfaces of the nuclear burning zones (Young et al., 2005). Furthermore, convective modelling by Frey et al. (2013) has found that some of the helium in its layer can get mixed further within the star where, thanks to greater temperatures, can get burned into oxygen, thus depleting the helium layer slightly. I speculate that this creates less of a boundary for the hydrogen to pass when it gets inwardly mixed so that it may reach the layer of CO (in the remnant phase) and therefore it is easier to become co-located with the CO and can form HCO^+. These two forms of mixing at the pre-SN stage involve the mixing of hydrogen in with the carbon and oxygen rich gas which could help to form HCO^+ in the latter years after the supernova explosion when the regions of the ejecta are cool enough to start forming molecules.

3.1.3 The Spatial Distributions of HCO^+, CO and H_2

The rate of HCO^+ formation, $R_{\mathrm{HCO^+}}$, in Sect. 3.1.1, through some simplifications appeared to be no longer dependent on the number density of CO n_{CO}. However, this is a simplification for the estimation of HCO^+ mass only, in reality, HCO^+ formation would depend on CO in some way, through chains of reactions in the ejecta that eventually form HCO^+ or possibly directly via Eq. 3.2. Therefore, I postulate that HCO^+ formation is still dependent on n_{CO} in the ejecta as well as $n_{\mathrm{H_2}}$. It is commonly-known that $n_{\mathrm{H_2}}$ is a tracer of n_{CO} of most regions in the ISM (e.g. Oka 2006). This relationship however appears not to be apparent in the ejecta of SN 1987A as the spatial distributions of CO compared to H_2 are different (Larsson et al., 2019b; Matsuura et al., 2024). The H_2 emission in the NIR observations show the location of the excitation mechanisms which power the H_2 emission rather than showing the location of the H_2 molecules themselves. The process which powers the H_2 emission in the NIR is likely to be from the UV field generated either by degraded X-rays from the ring or by the decay of ^{44}Ti (Larsson et al., 2023; Fransson et al., 2016). The UV field however does not power the CO emission nor the HCO^+ emission in the sub-mm which leads to the apparent spatial differences between the H_2 and the CO and HCO^+ emissions.

3.2 Conclusions

The aims of this master's thesis was to infer details on how HCO^+ is able to form in the ejecta of SN 1987A. Since it is still quite a novel molecule to be observed in the ejecta of supernovae, there is a lot of uncertainty regarding what chemical pathways form HCO^+ in such an environment. Additionally, analysing the HCO^+ emission can infer details on the hydrodynamical mixing that has occurred in the remnant as HCO^+ formation requires the interaction of hydrogen with carbon and oxygen, which are confined to different locations within the progenitor star. ALMA observations of the $J = 3 - 2$ and $J = 4 - 3$ HCO^+ line emission at 265.6−269.2 and 354.7−358.0 GHz were analysed for this master's thesis. To investigate its chemical formation pathways, I compare the spatial distributions of HCO^+ to that of the $J = 2 - 1$ CO emission which: (1) has very similar morphologies, and (2) returned a correlation strength of 0.72, showing a strong correlation. These results indicate that HCO^+ may form from CO.

In order to form HCO^+, a degree of ionisation needs to be present, to infer details about this ionisation level, I compare the $J = 3 - 2$ HCO^+ emission morphology to the morphology of Hα emission, which exists in the more strongly-ionised regions of the ejecta (e.g. Fransson et al. 2013). The HCO^+ emission had a more compact distribution to the Hα emission. From this, I infer that HCO^+ forms deeper within the ejecta where ionisation levels are relatively milder.

The HCO^+ line emission was also analysed and used to calculate a HCO^+ mass estimation. This was done by using the HCO^+ line intensities and comparing them to modelled line intensities from the radiative transfer code RADEX in which the HCO^+ column density (used to calculate the mass) is a free parameter. The HCO^+ masses were calculated to be: $(2.94\,^{+5.7}_{-1.2})\times10^{-6}\,M_\odot$ and $(8.80\,^{+31.5}_{-4.7})\times10^{-6}\,M_\odot$ if a H_2 collisional partner density of 10^6 or $10^5\,cm^{-3}$ was used respectively.

I investigate the feasibility of forming HCO^+ from CO by calculating a simple order of magnitude estimate of the HCO^+ mass formed from a single reaction with CO as a reactant. I utilise the reaction: $CO+H_3^+ \rightarrow HCO^++H_2$ to investigate how much HCO^+ forms over a 30-year timescale with a basic, uniformly mixed ejecta. A HCO^+ mass of $10^{-5}\,M_\odot$ is able to form which is a magnitude above the observed HCO^+ masses. This simple estimation has proved that a large amount of HCO^+ forming from CO is feasible in young supernova remnants on the timescale of decades. This analysis has also lead me to speculate that a moderate amount of H_2 needed to be co-located with CO to form HCO^+. Macroscopic mixing can inwardly mix some clumps of hydrogen from the outer envelope of the remnant down into the carbon-rich layers that would later form CO. However, I speculate that the HCO^+ formation can only be achieved if other forms of mixing also occurred, to mix the material of the clumps into its surroundings. One of these forms is microscopic mixing which can mix clumps of CO and H_2 at the molecular level. The others forms of mixing occur during the progenitor's star's lifetime and can inwardly mix hydrogen in alternative ways to that of macroscopic mixing. These include mixing at the He/H boundary due to a star's rotation, which can mix hydrogen further into the helium layer where there carbon and oxygen abundances begin to grow and also mixing at the O/He interface, which depletes helium through it burning and thus leaving less of a boundary for hydrogen to cross during the remnant phase in order to react with CO. This in-depth analysis of the HCO^+ emission opens up new avenues of further study to investigate; such as expanding upon chemical networks to include more hydrogen chemistry, and considering smaller scale mixing in hydrodynamical models of of SN remnants.

3.3 Future Work

This study into HCO^+ can open up many new avenues of further study. As mentioned previously, HCO^+ is a novel detection in supernova remnant environments which have yet to interact with the surrounding ISM. Therefore I discuss two avenues of future work. The first expansion of this analysis comes in the form of constructing a more extensive HCO^+ formation network in a SN 1987A-like environment. As stated in Sect. 3.1.1 I offer a simplistic approach to forming HCO^+ in the ejecta of SN 1987A. Since information regarding the masses and number densities of other potential HCO^+ reactants, such as CO_2, H_2O to name a few, are unknown, I focus on forming HCO^+ from only one reaction; H_3^+ + CO → HCO^+ +H_2. So one obvious avenue to pursue in the future would be to set up an extensive molecular formation network in the ejecta of SN 1987A. Starting with initial elemental abundances of SN 1987A such as in Woosley et al. (1988a); Thielemann et al. (1990) as examples, one can investigate what molecules form across time in the remnant. This has already been done for SN 1987A (e.g. Rawlings & Williams 1990; Lepp et al. 1990; Ono et al. 2024) and other supernovae (e.g. Cherchneff & Dwek 2009; Sarangi & Cherchneff 2013), but I suggest one step further, to add the amount of hydrogen inwardly mixed into the carbon and oxygen-rich regions which would later form CO, as a free parameter. This way, one can quantitatively infer how much hydrogen is inwardly mixed to replicate the HCO^+ observed masses. This opens up consideration for what other hydrogen-bearing molecules may exist in SN 1987A and indeed, other supernova remnants such as H_2O, CH or OH. Thus prompting astronomers to look for their emissions in remnants for future analysis and ultimately, uncovering more on the chemistry of supernova remnants.

APPENDIX A

An Appendix

A.1 An Appendix

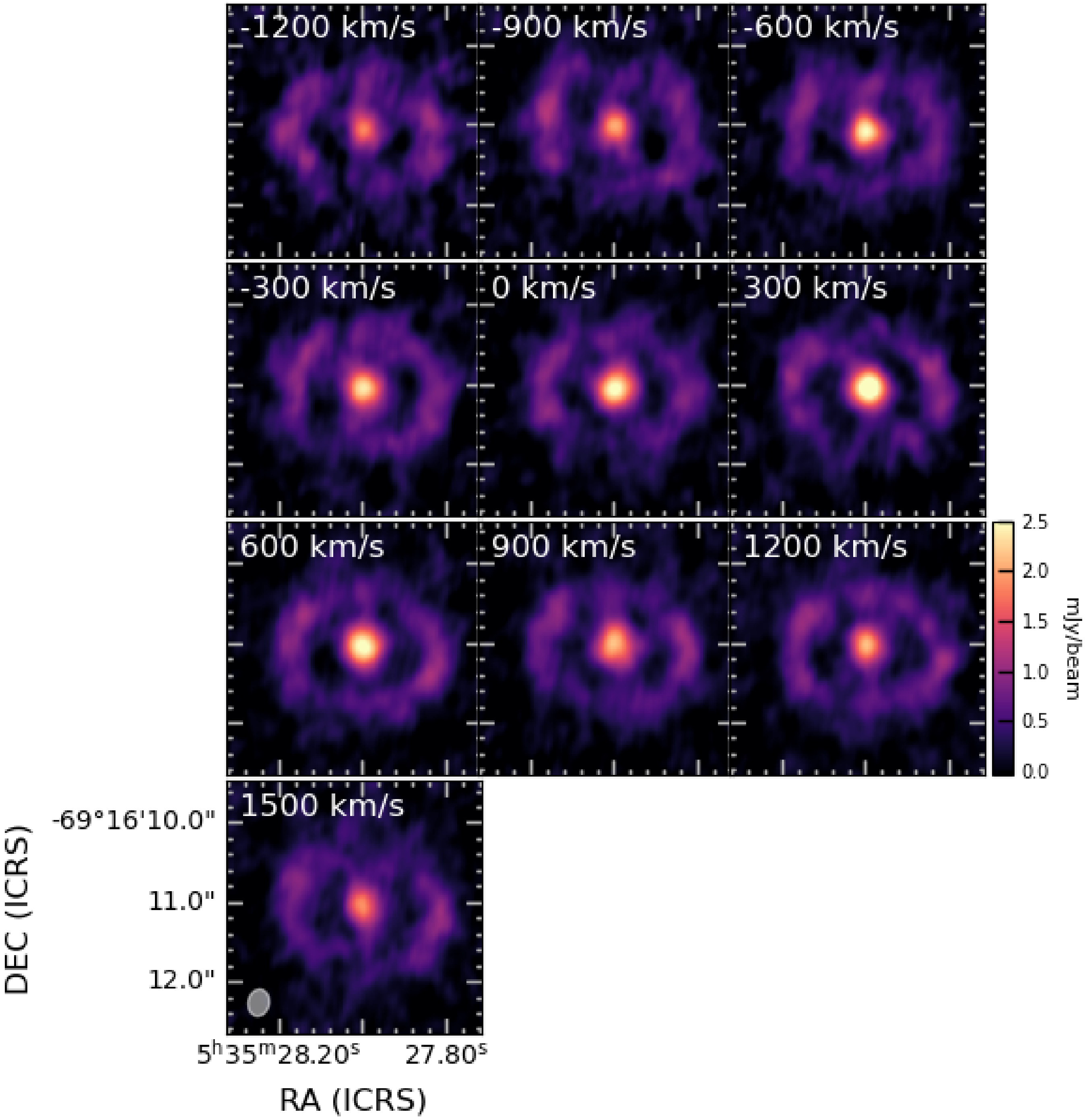

Figure A.1. A velocity channel map of the $J = 4 - 3$ HCO$^+$ emission. A non-zero continuum level is present in these images. The emission spans across a velocity range of -1350 to 1650 km s^{-1} which is binned in 300 km s^{-1} increments. Each slide is labelled with the median velocity of the 300 km s^{-1} bin. The velocities are respective to the $J = 4 - 3$ HCO$^+$ rest frequency at 356.7 GHz. The HCO$^+$ emission which originates in the ejecta is seen as a bright-blob due to it being not spatially resolved. There is also synchrotron emission from the ring present in this channel map which surrounds the ejecta.

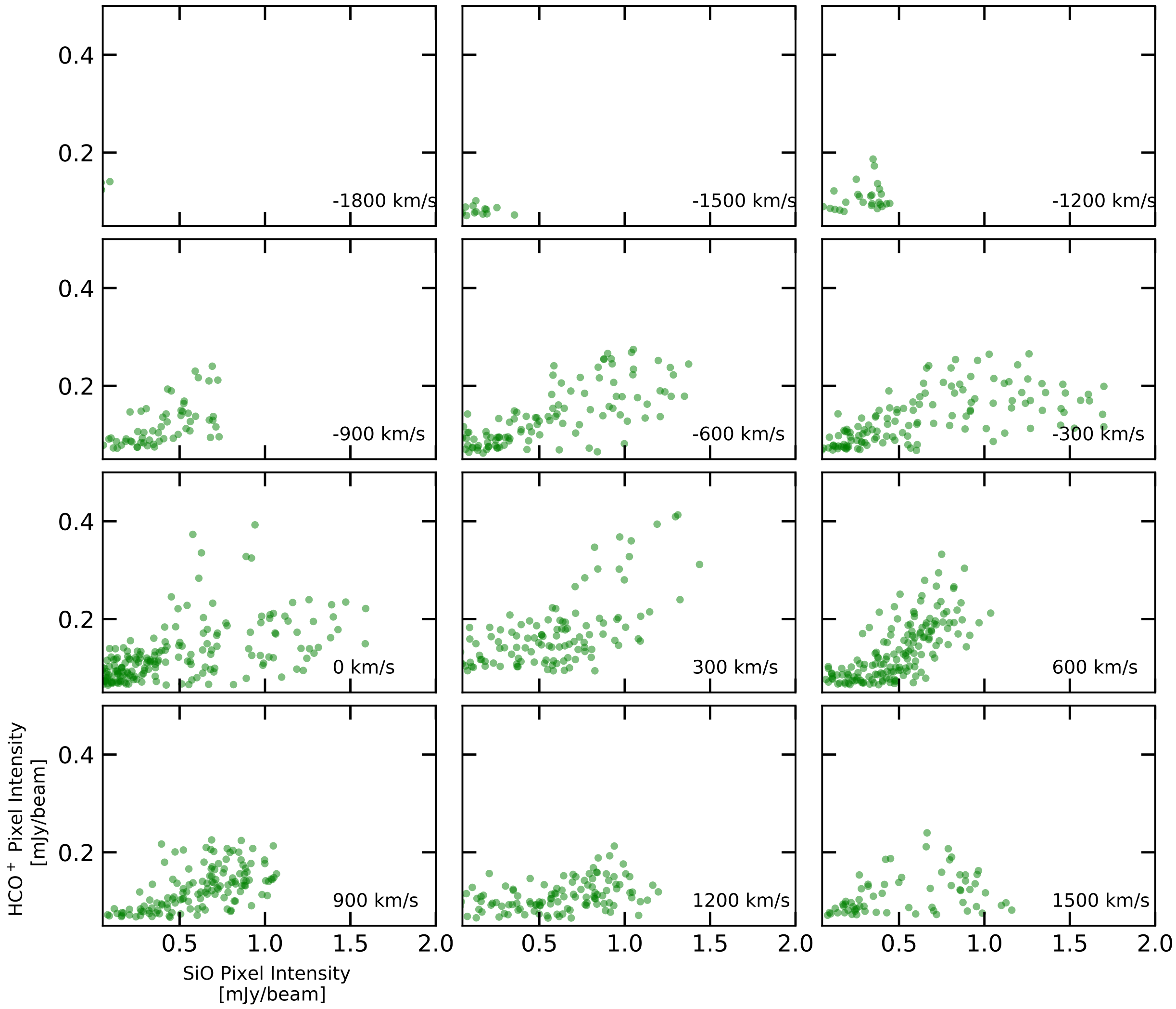

Figure A.2. Scatter plots of the pixel brightesses of HCO$^+$ (y-axis) versus SiO (x-axis) of each 300 km s^{-1} velocity bin. A threshold of 3 times the average RMS is introduced to each slide to omit low-brightness pixels belonging to the background. A monotonic relationship may be seen in the velocity slides of brightest intensity, these are ranging from -600 to 600 km s^{-1} but this relationship is faint due to the pixel brightnesses being scattered.

Bibliography

ALMA Partnership et al., 2015, *ApJ*, 808, L3

ALMA Partnership et al., 2017, ALMA Cycle 5 Technical Handbook

Abellán F. J., et al., 2017, *ApJ*, 842, L24

Ahmad I., Greene J. P., Moore E. F., Ghelberg S., Ofan A., Paul M., Kutschera W., 2006, Phys. Rev. C, 74, 065803

Aitken D. K., Smith C. H., James S. D., Roche P. F., Hyland A. R., McGregor P. J., 1988, *MNRAS*, 235, 19P

Arnett W. D., Bahcall J. N., Kirshner R. P., Woosley S. E., 1989, Annual Review of Astronomy and Astrophysics, 27, 629

Arnett D., Meakin C., Young P. A., 2007, in Kupka F., Roxburgh I., Chan K. L., eds, IAU Symposium Vol. 239, Convection in Astrophysics. pp 247–257, doi:10.1017/S1743921307000518

Asaki Y., Alcalde Pampliega B., Edwards P. G., Iguchi S., Murphy E. J., 2023, Nature Reviews Methods Primers volume 3, 3, 89

Astropy Collaboration et al., 2013, *A&A*, 558, A33

Astropy Collaboration et al., 2022, *ApJ*, 935, 167

Avni Y., 1976, *ApJ*, 210, 642

Bottke William F. J., Vokrouhlický D., Rubincam D. P., Nesvorný D., 2006, Annual Review of Earth and Planetary Sciences, 34, 157

Burbidge E. M., Burbidge G. R., Fowler W. A., Hoyle F., 1957, Reviews of Modern Physics, 29, 547

CASA Team et al., 2022, *PASP*, 134, 114501

Cherchneff I., Dwek E., 2009, *ApJ*, 703, 642

Chita S. M., Langer N., van Marle A. J., García-Segura G., Heger A., 2008, *A&A*, 488, L37

Cigan P., et al., 2019, *ApJ*, 886, 51

Comrie A., et al., 2021, CARTA: The Cube Analysis and Rendering Tool for Astronomy, doi:10.5281/zenodo.3377984

Cortes P. C., et al., 2024, ALMA Technical Handbook,ALMA Doc. 11.3, ver. 1.4, 2024, ALMA Technical Handbook, ALMA Doc. 11.3, ver. 1.4, ISBN 978-3-923524-66-2, doi:10.5281/zenodo.4511521

Crotts A. P. S., Heathcote S. R., 2000, *ApJ*, 528, 426

Culhane M., McCray R., 1995, *ApJ*, 455, 335

Draine B. T., 2011, Physics of the Interstellar and Intergalactic Medium

Dutrey A., et al., 2007, *A&A*, 464, 615

ESO The ALMA Partnership 2023, ALMA Receiver Bands, `https://www.eso.org/public/teles-instr/alma/receiver-bands/`

Einstein A., 1916, Deutsche Physikalische Gesellschaft, 18, 318

Farrell E., Groh J. H., Hirschi R., Murphy L., Kaiser E., Ekström S., Georgy C., Meynet G., 2021, *MNRAS*, 502, L40

France K., et al., 2010, Science, 329, 1624

Frank K. A., Zhekov S. A., Park S., McCray R., Dwek E., Burrows D. N., 2016, *ApJ*, 829, 40

Fransson C., Kozma C., 2002, New A Rev., 46, 487

Fransson C., et al., 2013, *ApJ*, 768, 88

Fransson C., et al., 2015, *ApJ*, 806, L19

Fransson C., Larsson J., Spyromilio J., Leibundgut B., McCray R., Jerkstrand A., 2016, *ApJ*, 821, L5

Fransson C., et al., 2024, Science, 383, 898

Frey L. H., Fryer C. L., Young P. A., 2013, *ApJ*, 773, L7

Gabler M., Wongwathanarat A., Janka H.-T., 2021, *MNRAS*, 502, 3264

Goldsmith P. F., Langer W. D., 1999, *ApJ*, 517, 209

Gomez H. L., et al., 2012, *ApJ*, 760, 96

Groh J. H., et al., 2019, *A&A*, 627, A24

Gröningsson P., Fransson C., Leibundgut B., Lundqvist P., Challis P., Chevalier R. A., Spyromilio J., 2008, *A&A*, 492, 481

Hammer N. J., Janka H. T., Müller E., 2010, *ApJ*

Henning T., et al., 2024, *PASP*, 136, 054302

Herant M., Benz W., 1992, *ApJ*, 387, 294

Herbst E., Klemperer W., 1973, *AJ*, 185, 505

Hester J. J., et al., 2002, *ApJ*, 577, L49

Hildebrand R. H., 1983, *Quarterly Journal of the Royal Astronomical Society*, 24, 267

Högbom J. A., 1974, A&AS, 15, 417

Hoyle F., Wickramasinghe N. C., 1970, *Nature*, 226, 62

Hunter J. D., 2007, Computing in Science Engineering, 9, 90

James A., Dunne L., Eales S., Edmunds M. G., 2002, *MNRAS*, 335, 753

Janka H.-T., 2012, Annual Review of Nuclear and Particle Science, 62, 407

Jerkstrand A., Fransson C., Kozma C., 2011, *A&A*, 530, A45

Jones O. C., et al., 2023, *ApJ*, 958, 95

Kamenetzky J., et al., 2013, *ApJ*, 773, L34

Kozma C., Fransson C., 1998, *ApJ*, 497, 431

Kunkel W., et al., 1987, IAU Circ., 4316, 1

Larsson J., et al., 2011, *Nature*, 474, 484

Larsson J., et al., 2013, *ApJ*, 768, 89

Larsson J., et al., 2016, *ApJ*, 833, 147

Larsson J., et al., 2019a, *ApJ*, 873, 15

Larsson J., et al., 2019b, *ApJ*, 886, 147

Larsson J., et al., 2023, *ApJ*, 949, L27

Le Teuff Y. H., Millar T. J., Markwick A. J., 2000, A&AS, 146, 157

Leising M. D., Share G. H., 1990, *ApJ*, 357, 638

Lepp S., Dalgarno A., McCray R., 1990, *ApJ*, 358, 262

Liu W., Dalgarno A., 1995, *ApJ*, 454, 472

Liu W., Dalgarno A., Lepp S., 1992, *ApJ*, 396, 679

Matsuura M., et al., 2011, Science, 333, 1258

Matsuura M., et al., 2015, *ApJ*, 800, 50

Matsuura M., et al., 2017, MNRAS, 469, 3347

Matsuura M., et al., 2024, *MNRAS*, 532, 3625

Mazumdar P., Tram L. N., Wyrowski F., Menten K. M., Tang X., 2022, *A&A*, 668, A180

McCray R., 1993, *ARAA*, 31, 175

McCray R., Fransson C., 2016, *ARAA*, 54, 19

McElroy D., Walsh C., Markwick A. J., Cordiner M. A., Smith K., Millar T. J., 2013, *A&A*, 550, A36

Millar T. J., Bennett A., Rawlings J. M. C., Brown P. D., Charnley S. B., 1991, A&AS, 87, 585

Millar T. J., Farquhar P. R. A., Willacy K., 1997, A&AS, 121, 139

Millar T. J., Walsh C., Van de Sande M., Markwick A. J., 2024, *A&A*, 682, A109

Miller S., Tennyson J., Lepp S., Dalgarno A., 1992, *Nature*, 355, 420

Morris T., Podsiadlowski P., 2007, Science, 315, 1103

Nozawa T., Kozasa T., Umeda H., Maeda K., Nomoto K., 2003, *ApJ*, 598, 785

Oka T., 2006, Proceedings of the National Academy of Science, 103, 12235

Ono M., Nozawa T., Nagataki S., Kozyreva A., Orlando S., Miceli M., Chen K.-J., 2024, *ApJS*, 271, 33

Panagia N., 1999, in New Views of the Magellanic Clouds. p. 549

Panagia N., Gilmozzi R., Macchetto F., Adorf H. M., Kirshner R. P., 1991, *ApJ*, 380, L23

Panessa M., Seifried D., Walch S., Gaches B., Barnes A. T., Bigiel F., Neumann L., 2023, *MNRAS*, 523, 6138

Press W. H., Teukolsky S. A., Vetterling W. T., Flannery B. P., 1999, Numerical recipes in C++ : the art of scientific computing, 2nd edn. Cambridge University Press

Prialnik D., 2010, An Introduction to the Theory of Stellar Structure and Evolution, 2nd edn. Cambridge University Press

Price-Whelan A. M., et al., 2018, *AJ*, 156, 123

Priestley F. D., Barlow M. J., Viti S., 2017, *MNRAS*, 472, 4444

Ravi A. P., Park S., Zhekov S. A., Orlando S., Miceli M., Frank K. A., Broos P. S., Burrows D. N., 2024, *ApJ*, 966, 147

Rawlings J., Williams D., 1990, Monthly Notices of the Royal Astronomy Society, 246, 208

Rieke G. H., 2012, Measuring the Universe. Cambridge University Press

Roche P. F., Aitken D. K., Smith C. H., 1991, *MNRAS*, 252, 39P

Rozwadowska K., Vissani F., Cappellaro E., 2021, New Astronomy, 83, 101498

Russell S. C., Dopita M. A., 1992, *ApJ*, 384, 508

Rybicki. G. B., Lightmann A. P., 1979, Radiative Processes in Astrophysics. Wiley-VCH Verlag GmbH & Co. KGaA Weinheim, pp 1–50 (`arXiv:9783527618170`), doi:10.1002/9783527618170

Sarangi A., Cherchneff I., 2013, *ApJ*, 776, 107

Schaefer B. E., 2023, *MNRAS*, 523, 3885

Schöier F. L., van der Tak F. F. S., van Dishoeck E. F., Black J. H., 2005, *A&A*, 432, 369

Shigeyama T., Nomoto K., 1990, *ApJ*, 360, 242

Snell R. L., Hollenbach D., Howe J. E., Neufeld D. A., Kaufman M. J., Melnick G. J., Bergin E. A., Wang Z., 2005, *ApJ*, 620, 758

Sonneborn G., et al., 1998, *ApJ*, 492, L139

Spitzer Jr. A., 1998, Physical Processes in the Interstellar Medium. John Wiley & Sons, Ltd, pp 32–69 (https://onlinelibrary.wiley.com/doi/pdf/10.1002/9783527617722.ch3), doi:https://doi.org/10.1002/9783527617722.ch3, `https://onlinelibrary.wiley.com/doi/abs/10.1002/9783527617722.ch3`

Spyromilio J., Meikle W. P. S., Learner R. C. M., Allen D. A., 1988, Letters to Nature, 334, 327

Tayler R., 1994, The Stars: Their Structure and Evolution, 2nd edn. Cambridge University Press

Taylor J. R., 1996, An Introduction to Error Analysis: The Study of Uncertainties in Physical Measurements, 2 sub edn. University Science Books

Thielemann F.-K., Hashimoto M.-A., Nomoto K., 1990, *ApJ*, 349, 222

Tielens A. G. G. M., 2005, The Physics and Chemistry of the Interstellar Medium. Cambridge University Press, doi:10.1017/CBO9780511819056

Travaglio C., Gallino R., Amari S., Zinner E., Woosley S., Lewis R. S., 1999, *ApJ*, 510, 325

Tu T.-y., Chen Y., Zhou P., Safi-Harb S., Liu Q.-C., 2024, *ApJ*, 966, 178

Utrobin V. P., Wongwathanarat A., Janka H. T., Müller E., 2015, *A&A*, 581, A40

Utrobin V. P., Wongwathanarat A., Janka H. T., Müller E., Ertl T., Woosley S. E., 2019, *A&A*, 624, A116

Utrobin V. P., Wongwathanarat A., Janka H. T., Müller E., Ertl T., Menon A., Heger A., 2021, *ApJ*, 914, 4

Virtanen P., et al., 2020, Nature Methods, 17, 261

Wasserman L., 2003, All of Statistics, 1st edn. Springer New York, NY, doi:https://doi.org/10.1007/978-0-387-21736-9

Whittet D. C. B., 1992, Dust in the galactic environment

Williams D. A., Viti S., 2013, Observational Molecular Astronomy: Exploring the Universe Using Molecular Line Emissions. Cambridge Observing Handbooks for Research Astronomers, Cambridge University Press, doi:10.1017/CBO9781139087445

Wilson T. L., Rohlfs K., Hüttemeister S., 2013, Tools of Radio Astronomy 6th Edition, 6th edn. Astronomy and Astrophysics Library, Springer Berlin, Heidelberg, doi:10.1007/978-3-642-39950-3

Wongwathanarat A., Müller E., Janka H. T., 2015, *ApJ*, 577, 1371–1385

Woodall J., Agúndez M., Markwick-Kemper A. J., Millar T. J., 2007, *A&A*, 466, 1197

Wooden D. H., Rank D. M., Bregman J. D., Witteborn F. C., Tielens A. G. G. M., Cohen M., Pinto P. A., Axelrod T. S., 1993, *ApJS*, 88, 477

Woosley S. E., 1988, *ApJ*, 330, 218

Woosley S. E., Pinto P. A., Weaver T. A., 1988a, PASA, 7, 355

Woosley S. E., Pinto P. A., Ensman L., 1988b, *ApJ*, 324, 466

Wootten A., et al., 2022, *AJ*, 925, 59

Yang Y., Jiang Z., Chen Z., Ao Y., Yu S., 2021, *ApJ*, 922, 144

Young P. A., Meakin C., Arnett D., Fryer C. L., 2005, *ApJ*, 629, L101

Zhou P., et al., 2022, *ApJ*, 931, 144

van der Tak F. F. S., Black J. H., Schöier F. L., Jansen D. J., van Dishoeck E. F., 2007, *A&A*, 468, 627

van der Walt S., Colbert S. C., Varoquaux G., 2011, Computing in Science Engineering, 13, 22